**US Army Corps
of Engineers**®
Engineer Research and
Development Center

BOUSS-2D: A Boussinesq Wave Model for Coastal Regions and Harbors

Report 1
Theoretical Background and User's Manual

Okey George Nwogu and Zeki Demirbilek

September 2001

20020403 092

BOUSS-2D: A Boussinesq Wave Model for Coastal Regions and Harbors

Report 1
Theoretical Background and User's Manual

by   Okey George Nwogu

Davidson Laboratory
Stevens Institute of Technology
Castle Point on the Hudson
Hoboken, NJ 07030

Zeki Demirbilek

Coastal and Hydraulics Laboratory
U.S. Army Engineer Research and Development Center
3909 Halls Ferry Road
Vicksburg, MS 39180-6199

Report 1 of a series

Contents

List of Figures

Preface

The work described herein was conducted by the U.S. Army Engineer Research and Development Center (ERDC), Coastal and Hydraulics Laboratory (CHL), under the Coastal Navigation Hydrodynamics Program work unit Waves in Entrance Channels. Overall program management was directed by the Hydraulic Design Section of Headquarters, U.S. Army Corps of Engineers (HQUSACE). Program Monitors were Messrs. Charles Chesnutt, Barry Holliday, and Mike Klosterman, HQUSACE. The Technical Director was Dr. William McAnally, CHL.

This study was conducted under the general supervision of Mr. Bruce A. Ebersole, Chief, Coastal Processes Branch (CPB), and Mr. Thomas W. Richardson, Acting Director, CHL. The report was prepared by Dr. Okey Nwogu, research scientist, Stevens Institute of Technology, and Dr. Zeki Demirbilek, research hydraulic engineer, Coastal Hydrodynamics Branch, CHL. Dr. Jane M. Smith (CPB) provided technical review of this report.

At the time of publication of this report, Dr. James R. Houston was Director of ERDC, and COL John W. Morris III, EN, was Commander and Executive Director.

1 Introduction

Background

An important component of most coastal and ocean engineering projects is an accurate assessment of the wave climate at the project site. Typical applications include determination of siltation rates inside entrance channels and harbor basins, determination of safe conditions for the loading/offloading of ships, optimization of harbor layouts for both wind-generated and long-period infragravity waves, design of structures such as breakwaters, and the evaluation of the impact of coastal structures on adjacent shorelines. Nearshore wave conditions are normally determined from deepwater conditions because long-term wave data are usually unavailable for most project sites. These offshore wave characteristics have to be transformed to the project site taking into account the effects of wind-wave generation, shoaling/refraction over seabed topography, energy dissipation due to wave breaking and bottom friction, wave reflection/diffraction near structures, nonlinear wave-wave interactions, and wave interaction with current fields.

A number of mathematical models have been developed to simulate the propagation and transformation of waves in coastal regions and harbors. The different models are based on different assumptions, which limit the types of problems to which they can be applied. Examples include spectral wind-wave models for wave propagation in open water where the processes of wind input, shoaling, and refraction are dominant; parabolic mild-slope equation models for wave propagation over large coastal areas when reflection is negligible; Helmholtz equation models for wave agitation and harbor resonance in water of constant depth; elliptic mild-slope models for wave agitation and harbor resonance in water of varying depth; and Boussinesq models for nonlinear wave refraction-diffraction in shallow water.

Numerical models available at the U.S. Army Corps of Engineers for predicting wave conditions in coastal regions and harbors include the spectral wind-wave model STWAVE (Smith, Sherlock, and Resio 2001) and the elliptic mild-slope model CGWAVE (Demirbilek and Panchang 1998). STWAVE is a wind-wave propagation model based on the wave action conservation equation. It is a phase-averaged model, i.e., it assumes that phase-averaged wave properties vary slowly over distances of the order of a wavelength. This allows the efficient computation of wave propagation over large open coastal areas. Due to the phase-averaging procedure, STWAVE cannot accurately resolve rapid variations that occur at subwavelength scales due to wave reflection/diffraction.

Phase resolving models based on either the mild-slope equation or Boussinesq-type equations are better suited for problems involving the reflection/diffraction of waves such as in coastal entrances and harbors. The mild-slope and Boussinesq equations are vertically integrated equations for wave propagation in the two-dimensional horizontal plane with different assumptions made for the variation of fluid motion over the water depth. The mild-slope equation derivation assumes a hyperbolic cosine variation of the velocity potential over depth, consistent with linear monochromatic waves in water of arbitrary depth, while the Boussinesq equation derivation assumes a quadratic profile, valid for shallow-water waves with wavelengths much longer than the water depth.

This report describes BOUSS-2D, a comprehensive numerical model based on a time-domain solution of Boussinesq-type equations. The classical form of the Boussinesq equations for wave propagation over water of variable depth was derived by Peregrine (1967). The equations were restricted to relatively shallow-water depths, i.e., the water depth, h, had to be less than one-fifth of the wavelength, L, in order to keep errors in the phase velocity to less than 5 percent. Nwogu (1993) extended the range of applicability of Boussinesq-type equations to deeper water by recasting the equations in terms of the velocity at an arbitrary distance z_α from the still-water level, instead of the depth-averaged velocity. The elevation of the velocity variable z_α becomes a free parameter, which is chosen to optimize the linear dispersion characteristics of the equations. The optimized form of the equations has errors of less than 2 percent in the phase velocity from shallow-water depths up to the deepwater limit ($h/L = 0.5$).

Despite the improvement in the frequency dispersion characteristics, Nwogu's (1993) equations are based on the assumption that the wave heights were much smaller than the water depth. This limits the ability of the equations to describe highly nonlinear waves in shallow water and led Wei et al. (1995) to derive a fully nonlinear form of the equations. The fully nonlinear equations are particularly useful for simulating highly asymmetric waves in shallow water, wave-induced currents, wave setup close to the shoreline, and wave-current interaction.

As ocean waves approach the shoreline, they steepen and ultimately break. The turbulence and currents generated by breaking waves are important driving mechanisms for the transport of sediments and pollutants. Nwogu (1996) extended the fully nonlinear form of the Boussinesq equations to the surf zone, by coupling the mass and momentum equations with a one-equation model for the temporal and spatial evolution of the turbulent kinetic energy produced by wave breaking. The equations have also been modified to include the effects of bottom friction and flow through porous structures. The modified equations can simulate most of the hydrodynamic phenomena of interest in coastal regions and harbor basins including:

a. Shoaling.

b. Refraction.

c. Diffraction.

d. Full/partial reflection and transmission.

   e. Bottom friction.

   f. Nonlinear wave-wave interactions.

   g. Wave breaking and runup.

   h. Wave-induced currents.

   i. Wave-current interaction.

A time domain, finite-difference method is used to solve the Boussinesq equations. The area of interest is discretized as a rectangular grid with the water-surface elevation and horizontal velocities defined at the grid nodes in a staggered manner. Time-histories of the velocities and fluxes corresponding to incident storm conditions are specified along external or internal wave generation boundaries. The wave conditions may be periodic or nonperiodic, unidirectional or multidirectional. Waves propagating out of the computational domain are absorbed in damping layers placed around the perimeter of the numerical basin. Porosity layers can be placed inside the computational domain to simulate the reflection and transmission characteristics of structures such as breakwaters.

Purpose

This report describes BOUSS-2D, a comprehensive numerical model for simulating the propagation and transformation of waves in coastal regions and harbors based on a time-domain solution of Boussinesq-type equations. An overview of the theoretical background behind the model is described in Chapter 2. The numerical scheme used to solve the equations is described in Chapter 3. The steps involved in setting up and running the model are described in Chapter 4. A number of analytical, laboratory, and field test cases have also been used to validate the model in Chapter 5. The different test cases were selected in Chapter 5 to evaluate the ability of the model to deal with individual wave transformation processes such as refraction, diffraction, wave breaking, etc., as well as the combination of processes that occur in practical engineering problems. Chapter 6 provides a summary and conclusions.

2   Theoretical Background

Governing Equations

BOUSS-2D is based on Boussinesq-type equations derived by Nwogu (1993, 1996). The equations are depth-integrated equations for the conservation of mass and momentum for nonlinear waves propagating in shallow and intermediate water depths. They can be considered to be a perturbation from the shallow-water equations, which are often used to simulate tidal flows in coastal regions. For short-period waves, the horizontal velocities are no longer uniform over depth and the pressure is nonhydrostatic. The vertical profile of the flow field is obtained by expanding the velocity potential, Φ, as a Taylor series about an arbitrary elevation, z_α, in the water column. For waves with length, L, much longer than the water depth, h, the series is truncated at second order resulting in a quadratic variation of the velocity potential over depth:

$$
\begin{aligned}
\Phi(x,z,t) \;=\;& \phi_\alpha + \mu^2 (z_\alpha - z)\left[\nabla\phi_\alpha \cdot \nabla h\right] \\
&+ \frac{\mu^2}{2}\left[(z_\alpha + h)^2 - (z+h)^2\right]\nabla^2\phi_\alpha + O(\mu^4)
\end{aligned}
\tag{1}
$$

where $\phi_\alpha = \Phi(x,z_\alpha,t)$, $\nabla = (\partial/\partial x, \partial/\partial y)$, and $\mu = h/L$ is a measure of frequency dispersion. The horizontal and vertical velocities are obtained from the velocity potential as:

$$
\begin{aligned}
u(x,z,t) \;=\; \nabla\Phi \;=\;& u_\alpha + (z_\alpha - z)\left[\nabla(u_\alpha \cdot \nabla h) + (\nabla \cdot u_\alpha)\nabla h\right] \\
&+ \frac{1}{2}\left[(z_\alpha + h)^2 - (z+h)^2\right]\nabla(\nabla \cdot u_\alpha)
\end{aligned}
\tag{2}
$$

$$
w(x,z,t) \;=\; \frac{\partial\Phi}{\partial z} \;=\; -\left[u_\alpha \cdot \nabla h + (z+h)\nabla \cdot u_\alpha\right]
\tag{3}
$$

where $u_\alpha = \nabla\Phi|_{z_\alpha}$ is the horizontal velocity at $z = z_\alpha$. Given a vertical profile for the flow field, the continuity and Euler (momentum) equations can be integrated over depth, reducing the three-dimensional problem to two dimensions. For weakly nonlinear waves with height, H, much smaller than the water depth, h, the vertically integrated equations are written in terms of the water-surface elevation $\eta(x,t)$ and velocity $u_\alpha(x,t)$ as (Nwogu 1993):

$$\eta_t + \nabla \cdot \boldsymbol{u}_f \;=\; 0 \tag{4}$$

$$\boldsymbol{u}_{\alpha,t} + g\nabla\eta + (\boldsymbol{u}_\alpha \cdot \nabla)\boldsymbol{u}_\alpha + z_\alpha\left[\nabla\left(\boldsymbol{u}_{\alpha,t}\cdot\nabla h\right) + (\nabla\cdot\boldsymbol{u}_{\alpha,t})\nabla h\right]$$
$$+ \frac{1}{2}\left[(z_\alpha+h)^2 - h^2\right]\nabla(\nabla\cdot\boldsymbol{u}_{\alpha,t}) \;=\; 0 \tag{5}$$

where g is the gravitational acceleration and $\boldsymbol{u}_f$ is the volume flux density given by:

$$\boldsymbol{u}_f \;=\; \int_{-h}^{\eta}\boldsymbol{u}\,dz \;=\; (h+\eta)\boldsymbol{u}_\alpha + h\left(z_\alpha + \frac{h}{2}\right)\left[\nabla(\boldsymbol{u}_\alpha\cdot\nabla h) + (\nabla\cdot\boldsymbol{u}_\alpha)\nabla h\right]$$
$$+ \quad h\left[\frac{(z_\alpha+h)^2}{2} - \frac{h^2}{6}\right]\nabla(\nabla\cdot\boldsymbol{u}_\alpha) \tag{6}$$

The depth-integrated equations are able to describe the propagation and transformation of irregular multidirectional waves over water of variable depth. The elevation of the velocity variable z_α is a free parameter and is chosen to minimize the differences between the linear dispersion characteristics of the model and the exact dispersion relation for small amplitude waves. The optimal value, $z_\alpha = -0.535h$, is close to middepth.

For steep near-breaking waves in shallow water, the wave height becomes of the order of the water depth and the weakly nonlinear assumption made in deriving Equations 4 and 5 is no longer valid. Wei et al. (1995) derived a fully nonlinear form of the equations from the dynamic free surface boundary condition by retaining all nonlinear terms, up to the order of truncation of the dispersive terms. Nwogu (1996) derived a more compact form of the equations by expressing some of the nonlinear terms as a function of the velocity at the free surface, $\boldsymbol{u}_\eta$, instead of $\boldsymbol{u}_\alpha$. Additional changes have also been made to the equations to allow for weakly rotational flows in the horizontal plane and ensure that z_α remains in the water column for steep waves near the shoreline and during the wave runup process. The revised form of the fully nonlinear equations can be written as:

$$\eta_t + \nabla \cdot \boldsymbol{u}_f \;=\; 0 \tag{7}$$

$$\boldsymbol{u}_{\alpha,t} + g\nabla\eta + \left(\boldsymbol{u}_\eta\cdot\nabla\right)\boldsymbol{u}_\eta + w_\eta\nabla w_\eta + (z_\alpha-\eta)\left[\nabla\left(\boldsymbol{u}_{\alpha,t}\cdot\nabla h\right) + (\nabla\cdot\boldsymbol{u}_{\alpha,t})\nabla h\right]$$
$$+ \frac{1}{2}\left[(z_\alpha+h)^2 - (h+\eta)^2\right]\nabla\left(\nabla\cdot\boldsymbol{u}_{\alpha,t}\right)$$
$$- \left[\left(\boldsymbol{u}_{\alpha,t}\cdot\nabla h\right) + (h+\eta)\nabla\cdot\boldsymbol{u}_{\alpha,t}\right]\nabla\eta$$
$$+ \left[\nabla\left(\boldsymbol{u}_{\alpha,t}\cdot\nabla h\right) + (\nabla\cdot\boldsymbol{u}_{\alpha,t})\nabla h + (z_\alpha+h)\nabla(\nabla\cdot\boldsymbol{u}_\alpha)\right]z_{\alpha,t} \;=\; 0 \tag{8}$$

where z_α is now a function of time and is given by $z_\alpha + h = 0.465(h+\eta)$. The volume flux density u_f is given by:

$$
\begin{aligned}
\boldsymbol{u}_f \;=\; & (h+\eta)\left\{\boldsymbol{u}_\alpha + \left[(z_\alpha+h) - \frac{(h+\eta)}{2}\right]\left[\nabla(\boldsymbol{u}_\alpha \cdot \nabla h) + (\nabla \cdot \boldsymbol{u}_\alpha)\nabla h\right]\right. \\
& \left. + \left[\frac{(z_\alpha+h)^2}{2} - \frac{(h+\eta)^2}{6}\right]\nabla(\nabla \cdot \boldsymbol{u}_\alpha)\right\}
\end{aligned}
\tag{9}
$$

The fully nonlinear equations are able to implicitly model the effects of wave-current interaction. Currents can either be introduced through the boundaries or by explicitly specifying a current field, U.

Linear Dispersion Properties

The linear dispersion relation of the Boussinesq model that relates the wavelength, L, to the wave period, T, is given by Nwogu (1993) as:

$$
C^2 = \frac{L^2}{T^2} = \left[\frac{1-(\alpha+1/3)(kh)^2}{1-\alpha(kh)^2}\right]
\tag{10}
$$

where C is the phase speed, $k = 2\pi/L$ is the wave number, and $\alpha = [(z_\alpha+h)^2/h^2 - 1]/2$. Depending on the elevation of the velocity variable or the value of α, different dispersion relations are obtained. If the velocity at the seabed ($z_\alpha = -h$) is used, $\alpha = -1/2$. Alternatively, if the velocity at the still-water level ($z_\alpha = 0$) is used, $\alpha = 0$. The dispersion relation of the classical form of the Boussinesq equations which uses the depth-averaged velocity as the velocity variable corresponds to $\alpha = -1/3$. Witting (1984) obtained the value $\alpha = -2/5$ from the Padé (2,2) approximant of tanh kh.

The phase speeds for different values of α, normalized with respect to the linear theory phase speed are plotted as a function of relative depth in Figure 1. The relative depth is defined as the ratio of the water depth, h, to the equivalent deepwater wavelength $L_o = gT^2/2\pi$. The deepwater depth limit corresponds to $h/L = 0.5$. The different dispersion equations are all equivalent in relatively shallow water ($h/L < 0.02$), but gradually diverge from the exact solution with increasing depth. An optimal depth $z_\alpha = -0.535h$ gives errors of less than 2 percent in the phase velocity from shallow-water depths up to the deepwater limit.

Nonlinear Properties

In an irregular sea state, different frequency components interact to generate forced waves at the sum and difference frequencies of the primary waves because of the nonlinear nature of the boundary condition at the free surface. Consider a

(1994) derived similar expressions for the weakly nonlinear form of the Boussinesq equations:

$$G_{\pm}(\omega_1,\omega_2) = \frac{\omega_1\omega_2(k_{\pm}h)^2\cos\Delta\theta[1-(\alpha+1/3)(k_{\pm}h)^2]}{2\lambda k_1'k_2'h^3}$$
$$+\frac{\omega_{\pm}[1-\alpha(k_{\pm}h)^2][\omega_1 k_2'h(k_1 h\pm k_2 h\cos\Delta\theta)+\omega_2 k_1'h(k_1 h\cos\Delta\theta\pm k_2 h)]}{2\lambda k_1'k_2'h^3} \tag{13}$$

where $Dq = q1 \pm q2$, $k_\pm = |k1\pm k2|$, $k' = k[1-(\alpha+1/3)(kh)2]$, and
$$\lambda = \omega_{\pm}^2[1-\alpha(k_{\pm}h)^2]-gk_{\pm}^2 h[1-(\alpha+1/3)(k_{\pm}h)^2] \tag{14}$$

Figure 2 shows a comparison of the quadratic transfer function of the weakly nonlinear Boussinesq model with that of second-order Stokes theory for unidirectional waves where the wave group period is 10 times the average of the individual wave periods, i.e., $\omega_- = (\omega_1 + \omega_2)/20$. The weakly nonlinear Boussinesq model underestimates the magnitude of the setdown wave and second harmonic at the deepwater depth limit by 65 percent and 45 percent respectively. Hence, it cannot accurately simulate nonlinear effects in deep water. To reasonably simulate nonlinear effects, the weakly nonlinear model should be restricted to the range $0 < h/L < 0.3$.

Simulation of Wave Breaking

The turbulent and highly rotational flow field under breaking waves is extremely complex and difficult to model even with the Reynolds-averaged form of the Navier-Stokes equations (e.g., Lin and Liu 1998; Bradford 2000). In BOUSS-2D, we do not attempt to model details of the turbulent motion, but rather, simulate the effect of breaking-induced turbulence on the flow field. We have tried to develop a generic model that can be applied to regular or irregular waves, unidirectional or multidirectional waves, and simple or complex bottom topography without having to recalibrate the model each time. The key assumptions made in developing the model are (see Nwogu 1996):

a. The breaking process is assumed to be "spilling."

b. Turbulence is produced in the near-surface region when the horizontal velocity at the free surface, u_η, exceeds the phase velocity, C.

c. The rate of production of turbulent kinetic energy is proportional to the vertical gradient of the horizontal velocity at the free surface, $\partial u/\partial z|_{z=\eta}$.

d. Breaking-induced turbulence is primarily convected in the near-surface region with the horizontal velocity at the free surface.
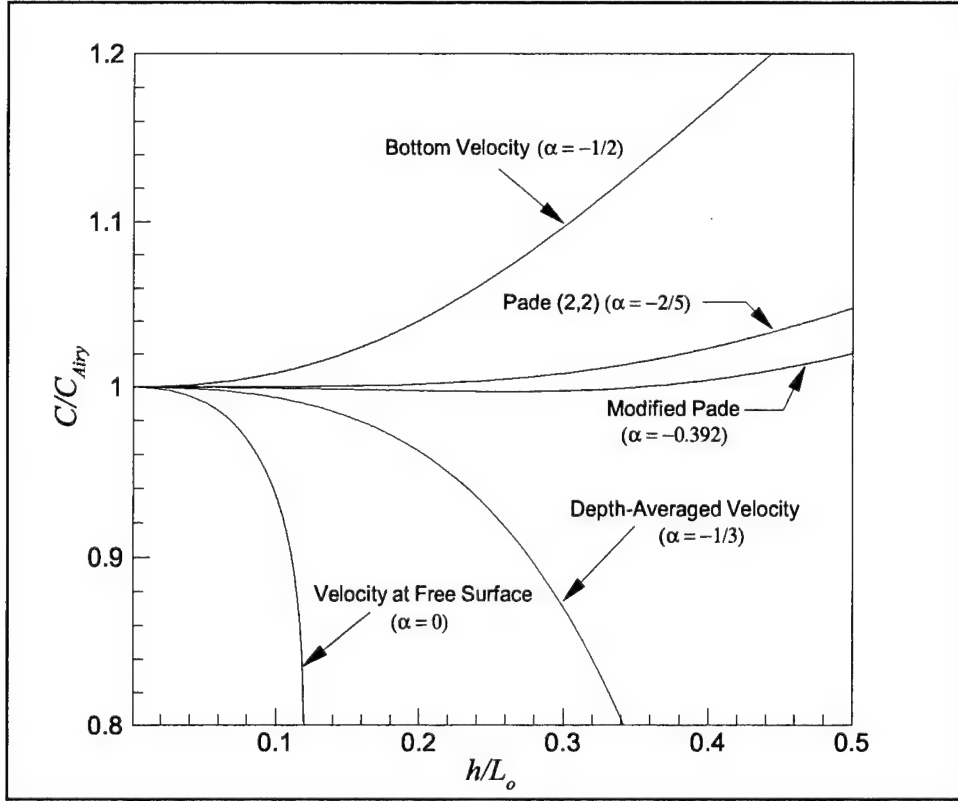
Figure 1   Comparison of normalized phase speeds for different values of α

wave train consisting of two small amplitude periodic waves with amplitudes, a_1 and a_2, frequencies, ω_1 and ω_2, wave numbers, k_1 and k_2, and propagating in directions θ_1 and θ_2 respectively. The water-surface elevation can be written as:

$$\eta^{(1)}(x,t) = a_1 \cos(k_1 \cdot x - \omega_1 t) + a_2 \cos(k_2 \cdot x - \omega_2 t) \tag{11}$$

where $k = (k\cos\theta, k\sin\theta)$. The second-order wave will consist of a subharmonic at the difference frequency, $\omega_- = \omega_1 - \omega_2$, and higher harmonics at the sum frequencies $2\omega_1$, $2\omega_2$ and $\omega_+ = \omega_1 + \omega_2$. This can be written as:

$$\begin{aligned}
\eta^{(2)}(x,t) = & \frac{a_1^2}{2} G_+(\omega_1,\omega_1,\theta_1,\theta_1) \ (\cos(2k_1 \cdot x - 2\omega_1 t) \\
& + \frac{a_2^2}{2} G_+(\omega_2,\omega_2,\theta_2,\theta_2) \ \cos(2k_2 \cdot x - 2\omega_2 t) \\
& + a_1 a_2 G_\pm(\omega_1,\omega_2,\theta_1,\theta_2) \ \cos(2k_\pm \cdot x - 2\omega_\pm t)
\end{aligned} \tag{12}$$

where $k_\pm = k_1 \pm k_2$, and $G_\pm(\omega_1, \omega_2, \theta_1,\theta_2)$ is a bidirectional quadratic transfer function that relates the amplitude of the second-order waves to the amplitude of the first-order waves. Dean and Sharma (1981) derived expressions for the bidirectional quadratic transfer function based on second-order Stokes theory. Nwogu
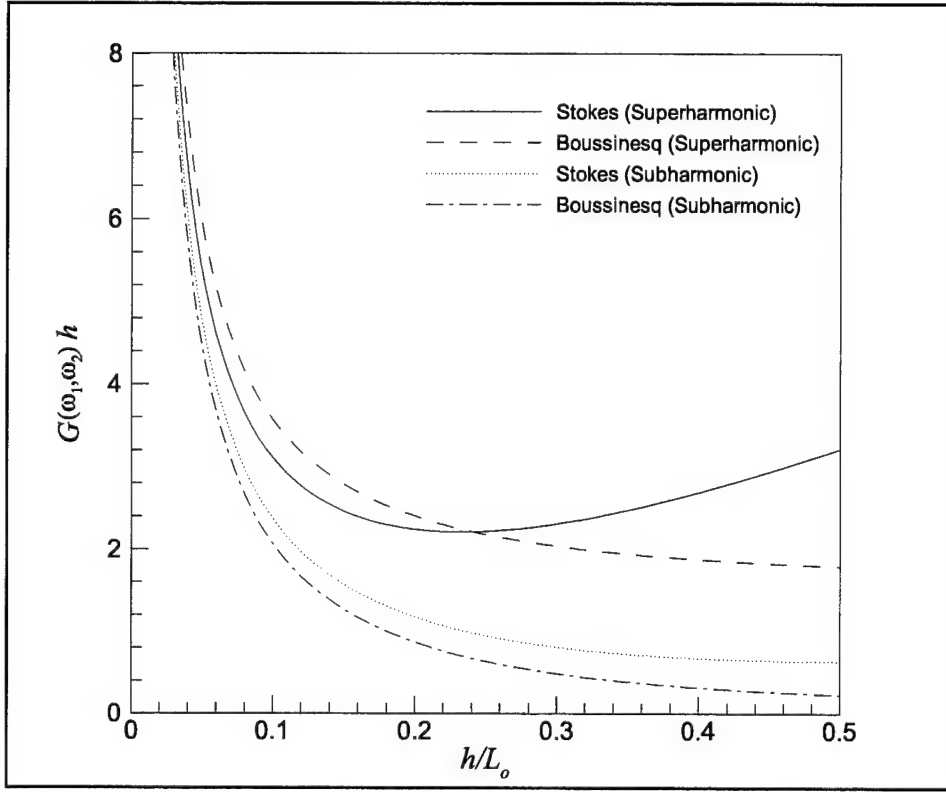
Figure 2. Comparison of quadratic transfer function for Boussinesq and Stokes theories

The effect of wave energy dissipation due to breaking is simulated in the Boussinesq model by introducing an eddy viscosity term to the right-hand side of the momentum equation (Equation 5 or 8). Nwogu (1996) used a dissipative term of the following form:

$$F_{breaking} = -v_t \nabla(\nabla . u_\alpha) \tag{15}$$

where v_t is the turbulent eddy viscosity. As pointed out by Kennedy et al. (2000), it is important for the dissipative term to dissipate energy but conserve momentum to accurately capture details of the mean flow field associated with breaking waves. A modified form of the dissipative term that ensures that momentum is conserved can be written as:

$$F_{breaking} = -\frac{1}{h+\eta} \nabla\{v_t(h+\eta)\nabla \cdot u_\alpha\} \tag{16}$$

The eddy viscosity is determined from the amount of turbulent kinetic energy, k, produced by wave breaking, and a turbulence length scale, l_t, using:

$$v_t = \sqrt{k}l_t \tag{17}$$

A one-equation model is used to describe the production, advection, diffusion, and dissipation of the turbulent kinetic energy produced by wave breaking:

$$k_t = -\mathbf{u}_\eta \cdot \nabla k + \sigma \nabla \cdot \nabla (\nu_t k) + B \frac{l_t^2}{\sqrt{C_D}} \left[\left(\frac{\partial u}{\partial z} \right)^2 + \left(\frac{\partial v}{\partial z} \right)^2 \right]_{z=\eta}^{3/2} - C_D \frac{k^{3/2}}{l_t} \quad (18)$$

The waves are assumed to start breaking when the horizontal component of the orbital velocity at the free surface, $\mathbf{u}_\eta$, exceeds the phase velocity of the waves, C. The parameter B is introduced to ensure that production of turbulence occurs after the waves break, i.e.,

$$B = \begin{cases} 0 & |\mathbf{u}_\eta| < C \\ 1 & |\mathbf{u}_\eta| \geq C \end{cases} \quad (19)$$

The phase velocity is determined from the linear dispersion relation (Equation 10) using the average zero-crossing period of the incident wave train. While this approach leads to some waves in an irregular wave train breaking at slightly different locations in the model than they would in nature, it was found to be more stable than trying to estimate a time-dependent phase velocity using expressions such as $C(t) = -\eta_t / |\nabla \eta|$.

The empirical constants C_D and σ have been chosen as 0.02 and 0.2 respectively. The turbulent length scale, l_t, remains the only free parameter in the turbulence model and is determined from comparisons of numerical model results with experimental data. Recommended values are the significant wave height ($l_t = H_{mo}$) for irregular waves, and the wave height ($l_t = H$) for regular waves.

Bottom Friction

The bottom boundary layer in wave fields is typically confined to a tiny region above the seabed, unlike river and tidal flows where it extends all the way up to the free surface. There is, thus, very little wave energy attenuation due to bottom friction over typical wave propagation distances of O (1km) used in Boussinesq-type models. The bottom friction factor, however, plays a more important role in wave transformation close to the shoreline and nearshore circulation patterns. The effect of energy dissipation due to a turbulent boundary layer at the seabed has been modeled by adding a bottom shear stress term to the right-hand side of the momentum equation (Equation 5 or 8):

$$F_{bfriction} = -\frac{1}{h+\eta} f_w \mathbf{u}_\alpha |\mathbf{u}_\alpha| \quad (20)$$

where f_w is the wave friction factor. The bottom friction term can also be written in terms of the Chezy coefficient, C_f, used in tidal flows by replacing f_w with g/C_f^2.

Equation 20 has been expressed in terms of u_α instead of the velocity at the seabed, u_b, to minimize the additional computational expense of evaluating u_b. The values of the friction factors specified in the model would thus be slightly different than those based on the bottom velocity.

3   Numerical Solution

Finite Difference Scheme

The weakly and fully nonlinear Boussinesq equations (Equations 4-9) are solved in the time-domain using a finite-difference method. The computational domain is discretized as a rectangular grid with grid sizes Δx and Δy, in the x and y directions, respectively. The equation variables η, u_α, and v_α are defined at the grid points in a staggered manner as shown in Figure 3. The water depth and surface elevation are defined at grid points (i,j), while the velocities are defined half a grid point on either side of the elevation grid points. The external boundaries of the computational domain correspond to velocity grid points.
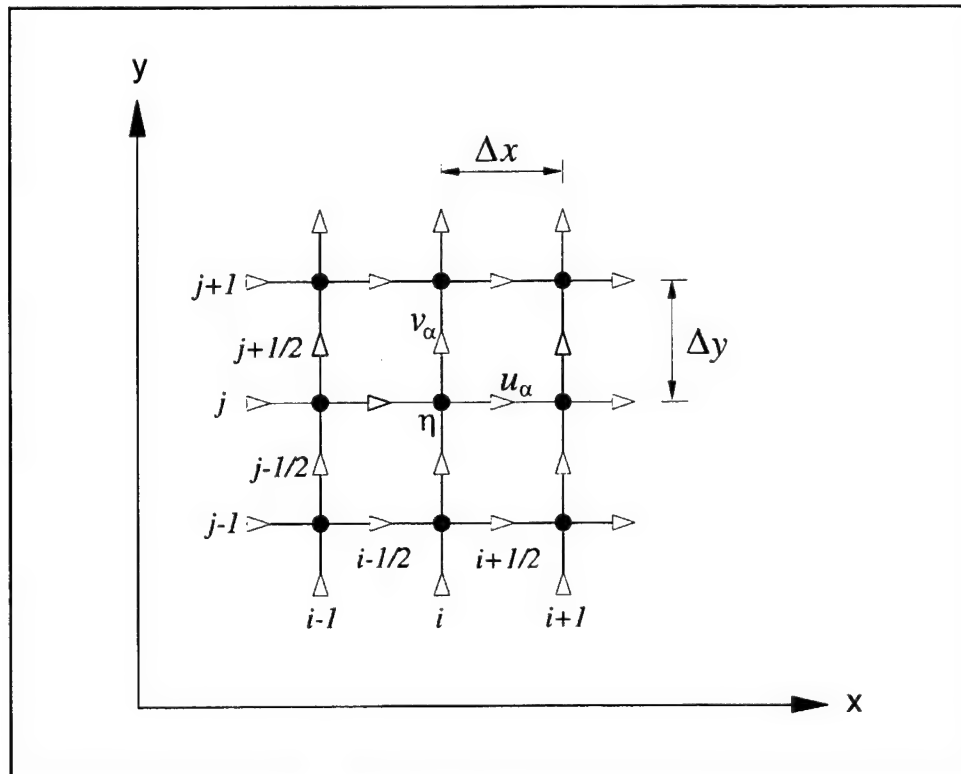
Figure 3.   Computational grid for finite difference scheme

The numerical solution scheme is an implicit Crank-Nicolson scheme with a predictor-corrector method used to provide the initial estimate. The first step in the solution scheme is the predictor step in which values of the variables at an intermediate time-step $t = (n + \frac{1}{2})\Delta t$ are determined using known values at $t = n\Delta t$ (Δt is the time-step size). The second step is the corrector step in which predicted values at $t = (n + \frac{1}{2})\Delta t$ are used to provide an initial estimate of the values at $t = (n+1)\Delta t$. The last step is an iterative Crank-Nicolson scheme, which is repeated until convergence.

The partial derivatives are approximated using a forward difference scheme for time and central difference schemes for the spatial variables. The resulting Crank-Nicolson formulation for the weakly nonlinear form of the mass and momentum equations (Equations 4-6) can be written as:

$$\delta_t \eta = - \; \delta_x^{(1)} u_f^{n+1/2} \; - \delta_y^{(1)} v_f^{n+1/2} \tag{21}$$

$$\delta_t \left(u_\alpha + f_4 \delta_x^{(2)} u_\alpha + f_2 \delta_{xx} u_\alpha \right) = - \; g\delta_x^{(1)} \eta^{n+1/2} - \frac{1}{2}\delta_x^{(1)} \left[\left(\overline{u_\alpha^{n+1/2}}^x \right)^2 \right] - \delta_y^{(1)} \left(\overline{v_\alpha^{n+1/2}}^x \; \overline{u_\alpha^{n+1/2}}^y \right)$$
$$- \; f_4 \left[\delta_y^{(1)}(h) \; \delta_t \delta_x^{(1)} \left(\overline{v_\alpha^{n+1/2}}^y \right) + \delta_x^{(1)}(h) \; \delta_t \delta_y^{(1)} \left(\overline{v_\alpha^{n+1/2}}^x \right) \right] \tag{22}$$
$$- \; f_2 \delta_t \delta_{xy} v_\alpha^{n+1/2}$$

$$\delta_t \left(v_\alpha + f_4 \delta_y^{(2)} v_\alpha + f_2 \delta_{yy} v_\alpha \right) = -g\delta_y^{(1)} \eta^{n+1/2} - \frac{1}{2}\delta_y^{(1)} \left[\left(\overline{v_\alpha^{n+1/2}}^y \right)^2 \right] - \delta_x^{(1)} \left(\overline{v_\alpha^{n+1/2}}^x \; \overline{u_\alpha^{n+1/2}}^y \right)$$
$$- \; f_4 \left[\delta_y^{(1)}(h) \; \delta_t \delta_x^{(1)} \left(\overline{u_\alpha^{n+1/2}}^y \right) + \delta_x^{(1)}(h) \; \delta_t \delta_y^{(1)} \left(\overline{u_\alpha^{n+1/2}}^x \right) \right] \tag{23}$$
$$- \; f_2 \delta_t \delta_{xy} u_\alpha^{n+1/2}$$

where the volume flux densities u_f and v_f are given by:

$$u_{f\,i+1/2,j} = \overline{h+\eta}^x u_{\alpha\,i+1/2,j} + \overline{h}^x f_1 \left(\delta_{xx} u_\alpha + \delta_{xy} v_\alpha \right)$$
$$+ \; \overline{h}^x f_3 \left[2\delta_x^{(1)}(h)\delta_x^{(2)} u_\alpha + \delta_x^{(1)}(h)\delta_y^{(1)} \left(\overline{v_\alpha}^x \right) + \delta_y^{(1)}(h) \; \delta_x^{(1)} \left(\overline{v_\alpha}^y \right) \right] \tag{24}$$

$$v_{f\,i,j+1/2} = \overline{h+\eta}^y v_{\alpha\,i,j+1/2} + \overline{h}^y f_1 \left(\delta_{xy} u_\alpha + \delta_{yy} v_\alpha \right)$$
$$+ \; \overline{h}^y f_3 \left[2\delta_y^{(1)}(h)\delta_y^{(2)} v_\alpha + \delta_x^{(1)}(h)\delta_y^{(1)} \left(\overline{u_\alpha}^x \right) + \delta_y^{(1)}(h) \; \delta_x^{(1)} \left(\overline{u_\alpha}^y \right) \right] \tag{25}$$

The parameters f_1 to f_4 are given by:

$$f_1 = \left[\frac{(z_\alpha + h)^2}{2} - \frac{h^2}{6} \right] \tag{26a}$$

$$f_2 = \left[\frac{(z_\alpha + h)^2}{2} - \frac{h^2}{2} \right] \tag{26b}$$

$$f_3 = \left[(z_\alpha + h) - \frac{h}{2} \right] \tag{26c}$$

$$f_4 = \left[(z_\alpha + h) - h \right] \tag{26d}$$

The average and difference operators in Equations 21 to 25 are given by:

$$\delta_t \phi = \frac{1}{\Delta t} \left(\phi^{n+1} - \phi^n \right) \tag{27a}$$

$$\phi^{n+1/2} = \frac{1}{2} \left(\phi^n + \phi^{n+1} \right) \tag{27b}$$

$$\bar{\phi}^x = \frac{1}{2} \left(\phi_{i+1,j} + \phi_{i,j} \right) \ or \ \frac{1}{2} \left(\phi_{i+1/2,j} + \phi_{i-1/2,j} \right) \tag{27c}$$

$$\bar{\phi}^y = \frac{1}{2} \left(\phi_{i,j+1} + \phi_{i,j} \right) \ or \ \frac{1}{2} \left(\phi_{i,j+1/2} + \phi_{i,j-1/2} \right) \tag{27d}$$

$$\delta_x^{(1)} \phi = \frac{1}{\Delta x} \left(\phi_{i+1,j} - \phi_{i,j} \right) \ or \ \frac{1}{\Delta x} \left(\phi_{i+1/2,j} - \phi_{i-1/2,j} \right) \tag{27e}$$

$$\delta_y^{(1)} \phi = \frac{1}{\Delta y} \left(\phi_{i,j+1} - \phi_{i,j} \right) \ or \ \frac{1}{\Delta y} \left(\phi_{i,j+1/2} - \phi_{i,j-1/2,j} \right) \tag{27f}$$

$$\delta_x^{(2)} \phi = \frac{1}{2\Delta x} \left(\phi_{i+3/2,j} - \phi_{i-1/2,j} \right) \tag{27g}$$

$$\delta_y^{(2)} \phi = \frac{1}{2\Delta y} \left(\phi_{i,j+3/2} - \phi_{i,j-1/2} \right) \tag{27h}$$

$$\delta_{xx} \phi = \frac{1}{\Delta x^2} \left(\phi_{i+3/2,j} - 2\phi_{i+1/2,j} + \phi_{i-1/2,j} \right) \tag{27i}$$

$$\delta_{yy} \phi = \frac{1}{\Delta y^2} \left(\phi_{i,j+3/2} - 2\phi_{i,j+1/2} + \phi_{i,j-1/2} \right) \tag{27j}$$

$$\delta_{xy} \phi = \frac{1}{\Delta x \Delta y} \left(\phi_{i,j+1} - 2\phi_{i,j} + \phi_{i,j-1} \right) \tag{27k}$$

and ϕ represents the variables (η, u_α, v_α). The finite-difference operator definitions in Equation 27 corresponding to the x and y components of the momentum equation are centered at ($i+1/2,j$) and ($i,j+1/2$), respectively.

The finite difference formulation of the continuity equation (Equation 21) yields an algebraic equation that is explicitly solved for η at all grid points. The formulation for the x and y momentum equations (Equations 22 and 23) have been decoupled by placing the v_{xt}, v_{yt}, and v_{xyt} terms on the right-hand side of the x equation and the u_{xt}, u_{yt}, and u_{xyt} terms on the right-hand side of the y equation. This reduces the momentum equations to tridiagonal equations for u_α and v_α along lines in the x and y direction, respectively. Tridiagonal matrices are much easier to store and solve than the large sparse matrix equation that would be obtained if the equations were not decoupled. The major disadvantage of this approach, however, is that the iterative step takes longer to converge for shorter-period waves propagating at large angles to the grid where the higher-order cross-derivative terms (u_{xyt}, v_{xyt}) become comparable in magnitude to the inline derivative terms (u_{xxt}, v_{yyt}).

The numerical scheme is stable provided that the Courant number, C_R, is less than 1, i.e.,

$$C_R = \sqrt{\left[C^2 \Delta t^2 \left(\frac{1}{\Delta x^2} + \frac{1}{\Delta y^2}\right)\right]} < 1 \tag{28}$$

where C is the phase speed based on the average zero-crossing period of the incident waves. It is, however, recommended that the Courant number be kept within the range 0.5 to 0.7 since nonlinear wave-wave interactions, wave breaking, and the presence of reflected waves can affect the stability criterion of the numerical model.

Boundary Conditions

To solve the governing equations, appropriate boundary conditions have to be imposed at the boundaries of the computational domain. This requires specification of waves propagating into the domain and the absorption of waves propagating out of the domain. The equations have also been modified to simulate wave interaction with fully/partially reflecting structures within the computational domain. The types of boundaries considered in BOUSS-2D include:

   a. Fully reflecting or solid wall boundaries.

   b. External wave generation boundaries.

   c. Internal wave generation boundaries.

   d. Wave absorption or damping regions.

   e. Porous structures.

Solid wall boundaries

Along solid wall or fully reflecting boundaries, the horizontal velocity normal to the boundary must be zero over the entire water depth, i.e.,

$$\boldsymbol{u} \cdot \boldsymbol{n} \quad = \quad 0 \qquad -h < z < \eta \tag{29}$$

where n is the normal vector to the boundary. This condition is satisfied in the depth-integrated equations by specifying that both the volume flux density and velocity normal to the boundary are zero, i.e.,

$$\boldsymbol{u}_\alpha \cdot \boldsymbol{n} \quad = \quad 0 \tag{30}$$

$$\boldsymbol{u}_f \cdot \boldsymbol{n} \quad = \quad 0 \tag{31}$$

Since the equations are solved on a staggered grid, the boundary conditions are specified as either $u_\alpha = u_f = 0$ along wall boundaries perpendicular to the x-axis, or $v_\alpha = v_f = 0$ along wall boundaries perpendicular to the y-axis.

External wave generation boundaries

Along external wave generation boundaries, time-histories of velocities u_α or v_α, and flux densities u_f or v_f corresponding to an incident storm condition are specified. The time-histories may correspond to regular or irregular, unidirectional or multidirectional waves.

Regular Waves. Regular, long-crested wave conditions are specified in terms of a wave height, H, wave period, T, and direction of propagation, θ. The water-surface elevation for small-amplitude waves ($H \ll h$) may be written as:

$$\eta(x,y,t) \quad = \quad \frac{H}{2} \cos\left(kx\cos\theta + ky\sin\theta - \omega t\right) \tag{32}$$

where $\omega = 2\pi/T$ is the angular frequency, k is the wave number, and θ is the direction of wave propagation relative to the positive x-axis. The boundary conditions along a wave generation line perpendicular to the x-axis may be obtained from the linearized form of the continuity equation (Equation 5) for water of constant depth as:

$$u_\alpha(x_g, y_g, t) \quad = \quad T_u(\omega)\cos\theta \ \ \eta(x_g, y_g, t) \tag{33}$$

$$u_f(x_g, y_g, t) \quad = \quad \left[(h+\eta) \ - \ h\left(\frac{\alpha_2^2}{2} - \frac{1}{6}\right)(kh)^2\right]u_\alpha(x_g, y_g, t) \tag{34}$$

where (x_g, y_g) are the x-y coordinates of the wave generation line and $T_u(\omega)$ is a linear transfer function given by:

$$T_u(\omega) \quad = \quad \frac{\omega}{kh\left[1 - \left(\frac{\alpha_2^2}{2} - \frac{1}{6}\right)(kh)^2\right]} \tag{35}$$

and $\alpha_2 = (z_\alpha + h)/h$. Similar expressions apply to v_α and v_f for wave generation lines perpendicular to the y-axis with $\cos\theta$ replaced by $\sin\theta$ in Equation 33.

For large amplitude waves $[H = O(h)]$, higher harmonic components (2ω, 3ω, etc.) are generated due to the nonlinear terms in the governing equations. These waves are often called bound waves since they are attached to the primary wave and travel at its phase speed, $C = \omega/k$, instead of the phase speed of a free wave at the corresponding frequency. The wave shape also changes from the sinusoidal shape assumed in Equation 32 to an asymmetric one with peaked crests and broad shallow troughs. If linear wave conditions are imposed at the boundaries, the numerical model will generate free higher harmonic components with the same magnitude but 180 deg out of phase with the bound waves at the wavemaker to satisfy the linear boundary condition. The presence of bound and free higher frequency waves that travel at different speeds will lead to a spatially nonhomogenous wave field with the wave height and shape changing continuously over the computational domain.

The Fourier approximation method of Rienecker and Fenton (1981) has been used to solve the weakly nonlinear form of the Boussinesq equations and develop nonlinear boundary conditions for the generation of large-amplitude regular waves in shallow water. The partial differential Equations 4 to 6 are initially transformed into a set of coupled nonlinear ordinary differential equations in terms of a moving coordinate system, $\xi = x - Ct$. The velocity variable u_α is expanded as a Fourier series and substituted into the governing equations, which are evaluated at a finite number of collocation points over half a wavelength to yield a system of nonlinear algebraic equations. A Newton-Raphson iterative procedure is used to solve the nonlinear equations for the unknown values of the free surface displacement at the collocation points, the Fourier coefficients, the wave number, and the phase speed. Details of the technique are provided in Appendix A.

Irregular Unidirectional Waves. For nonperiodic waves, the incident wave conditions are typically expressed in the form of a wave spectrum, which describes the frequency distribution of wave energy. Different parametric shapes have been proposed for wave spectra including:

a. The Pierson-Moskowitz (PM) spectrum for fully developed sea states in deep water, which is defined in terms of the wind speed.

b. The Bretschneider (1959) spectrum, which has the same shape as the PM spectrum but is defined in terms of the significant wave height and peak period.

    c. The JONSWAP spectrum for fetch-limited conditions in deep water.

    d. The TMA spectrum for fetch-limited conditions in shallow water.

    e. The Ochi-Hubble spectrum for bimodal sea states with double-peaked spectra.

Expressions for the different wave spectra are provided in Appendix B.

The Fourier series technique is used to generate time-histories of the velocity boundary conditions from the wave spectrum. The water-surface elevation, $\eta(t)$, is assumed to be a zero-mean, stationary, random Gaussian process. The surface-elevation time series at a reference point $x_r = (x_r, y_r)$ in the computational domain can be represented as a linear superposition of N regular wave components, i.e.,

$$\eta(x_r,t) = \sum_{j=1}^{N} a_j \cos\left[k_j \cdot x_r - \omega_j t + \varepsilon_j \right] \tag{36}$$

where a_j, ω_j, ε_j, and $k_j = (k_j\cos\theta, k_j\sin\theta)$ are the amplitude, angular frequency, phase angle, and wave number vector of the jth frequency component, respectively. The angle, θ, is the direction of wave propagation relative to the positive x-axis.

The wave spectrum is divided into N frequency bands with uniform spacing, $\Delta\omega$, so that the frequency of the jth wave component is given by $\omega_j = j\Delta\omega$. The amplitudes of the individual wave components are obtained deterministically from the wave spectrum, $S_\eta(\omega)$, as:

$$a_j = \sqrt{2S_\eta(\omega_j)\Delta\omega} \tag{37}$$

while the phase angles, ε_j, are randomly selected from a uniform distribution between 0 and 2π. Incident wave conditions are more typically specified in terms of the repeat period or duration of the record, T_D, and time-step, Δt. The values of N and $\Delta\omega$ can be obtained from these as:

$$\Delta\omega = \frac{1}{T_D} \tag{38}$$

$$N = \frac{T_D}{2\Delta t} \tag{39}$$

The velocity and flux boundary conditions along a wave generation line perpendicular to the x-axis may be obtained from the surface elevation using the linear transfer function approach:

$$u_\alpha(x_g,t) = \sum_{j=1}^{N} T_u(\omega_j) a_j \cos\theta \cos\left[k_j \cdot (x_g - x_r) - \omega_j t + \varepsilon_j \right] \tag{40}$$

$$u_f(\boldsymbol{x_g}, t) = [h + \eta(\boldsymbol{x_g}, t)]u_\alpha(\boldsymbol{x_g}, t) + h^3\left[\frac{\alpha_2^2}{2} - \frac{1}{6}\right]\left(u_{\alpha xx}(\boldsymbol{x_g}, t) + v_{\alpha xy}(\boldsymbol{x_g}, t)\right) \qquad (41)$$

where

$$\eta(\boldsymbol{x_g}, t) = \sum_{j=1}^{N} a_j \cos\left[\boldsymbol{k_j} \cdot (\boldsymbol{x_g} - \boldsymbol{x_r}) - \omega_j t + \varepsilon_j\right] \qquad (42)$$

$$u_{\alpha xx}(\boldsymbol{x_g}, t) = -\sum_{j=1}^{N} a_j k_j^2 \cos^3\theta \cos\left[\boldsymbol{k_j} \cdot (\boldsymbol{x_g} - \boldsymbol{x_r}) - \omega_j t + \varepsilon_j\right] \qquad (43)$$

$$v_{\alpha xy}(\boldsymbol{x_g}, t) = -\sum_{j=1}^{N} a_j k_j^2 \sin^2\theta \cos\theta \cos\left[\boldsymbol{k_j} \cdot (\boldsymbol{x_g} - \boldsymbol{x_r}) - \omega_j t + \varepsilon_j\right] \qquad (44)$$

For highly nonlinear irregular waves in shallow water[1], the velocity boundary conditions would have to be modified to take into account the presence of lower and higher frequency wave components induced by nonlinear interactions between the primary wave components. Second-order Boussinesq theory can be used to generate the velocities and flux densities associated with the bound second-order waves along the wave generation boundary. However, this theory is valid over a limited range of wave steepnesses (H/L) and relative depths (h/L) because it only includes second-harmonic terms. Second-order Stokes theory, for example, cannot accurately describe the shape of cnoidal-type waves in shallow water when the Ursell parameter (HL^2/h^3) is large.

A different approach to generating steep irregular waves in shallow water is the nonlinear Fourier method of Osborne (1997), in which an irregular wave train is represented as a superposition of nonlinear cnoidal or solitary type waves. This approach, however, has not yet been implemented in BOUSS-2D.

Irregular Multidirectional Waves. Naturally occurring ocean waves exhibit a pattern that varies randomly not only in time but also in space. The wave energy is distributed over both frequency and direction and can be described in terms of a directional wave spectrum, $S_\eta(\omega, \theta)$, which is the product of the frequency spectrum, $S_\eta(\omega)$, and a directional spreading function $D(\omega, \theta)$:

$$S_\eta(\omega, \theta) = S_\eta(\omega)D(\omega, \theta) \qquad (45)$$

The directional spreading function is non-negative and should satisfy the following relation:

$$\int_{-\pi}^{\pi} D(\omega, \theta) = 1 \qquad (46)$$

---

[1] A useful guideline is $H_{mo}/L_p > 0.025 \tanh k_p h$, where H_{mo} is the significant wave height, and L_p and k_p are respectively the wavelength and wave number based on the peak frequency of the spectrum.

One of the most commonly used models for the directional spreading function is the cosine-power function defined as:

$$D(\theta) \quad = \quad \frac{\Gamma(s+1)}{\sqrt{\pi}\,\Gamma(s+1/2)}\cos^{2s}(\theta - \theta_p) \qquad \text{for } |\theta - \theta_p| < \pi/2 \qquad (47)$$

where θ_p is the principal direction of wave propagation and Γ is the gamma function. The parameter s is an index describing the degree of directional spreading with $s \to \infty$ representing a unidirectional wave field. Figure 4 shows a plot of the of the cosine power spreading function for different values of the spreading index, s.
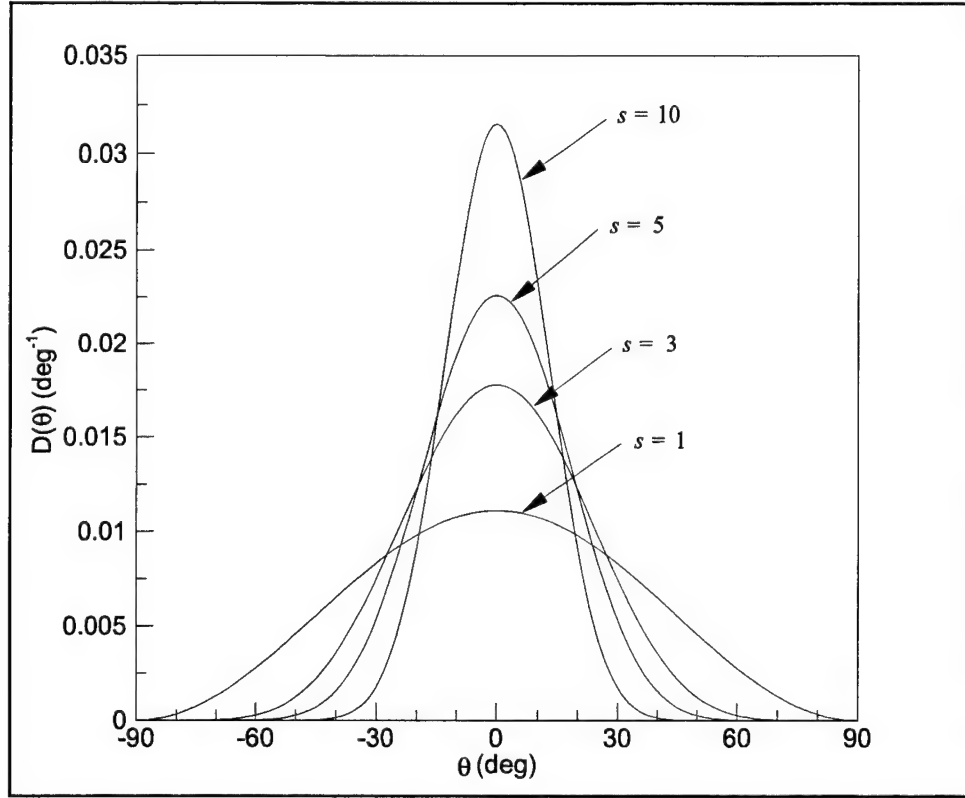
Figure 4.   Cosine-power spreading function for different values of the spreading index s

A number of other models have been proposed for the directional spreading function including the normal, circular normal, and wrapped-normal distribution (Borgman 1969). A more intuitive and universal parameter to describe the degree of directional spreading in a multidirectional sea state is the standard deviation of the directional spreading function, σ_θ, which is defined as:

$$\sigma_\theta^2 \quad = \quad \int_{\theta_p - \pi/2}^{\theta_p + \pi/2} D(\theta)\,(\theta - \theta_p)^2\,d\theta \tag{48}$$

Given the same standard deviation, there is very little difference between the shapes of different proposed forms of the directional spreading functions as shown in Appendix C.

Time-histories of the velocity boundary conditions can be synthesized from the directional wave spectrum using an extension of the linear superposition technique used for irregular, unidirectional waves. The directional wave spectrum is initially divided into N frequency bands with uniform spacing, $\Delta\omega$, and M direction bands with uniform spacing $\Delta\theta$. The water-surface elevation $\eta(x,t)$ can be represented as a linear superposition of periodic wave components with different amplitudes and frequencies, propagating in different directions, i.e.,

$$\eta(x,t) = \sum_{i=1}^{N} \sum_{j=1}^{M} a_{ij} \cos\left[k_{ij} \cdot x - \omega_i t + \varepsilon_{ij} \right] \tag{49}$$

where $k_{ij} = (k_i \cos\theta_j, k_i \sin\theta_j)$. The wave amplitudes, a_{ij}, are obtained deterministically from the directional wave spectrum as:

$$a_{ij} = \sqrt{2 S_\eta(\omega_i, \theta_j) \Delta\omega \Delta\theta} \tag{50}$$

while the phase angles, ε_{ij}, are randomly selected from a uniform distribution between 0 and 2π. For a given time series duration, T_D, and time-step, Δt, the values of N and $\Delta\omega$ can be obtained in the same manner as for unidirectional waves using Equations 38 and 39 respectively.

For finite duration time records, the double summation model (Equation 49) produces a wave field that is spatially nonhomogenous. As pointed out by Jeffreys (1987), this is because the phase difference between wave components with identical frequencies but propagating in different directions is no longer random but locked. An extreme example of this phenomenon is the standing wave pattern that is produced when incident waves are fully reflected by a vertical wall. The wave field consists of two waves with the same amplitude and frequency propagating in opposite directions with a constant phase difference between them. The wave heights vary from zero at the nodes to twice the incident wave height at the antinodes. This variability is obviously reduced by including more frequency and direction components. However, as pointed by Stansberg (1987) and others, the number of wave components required to reduce the spatial variability in wave energy to within acceptable levels is quite large [O(10,000)].

A different approach to producing a spatially homogenous multidirectional wave field is to assume that each wave component has a unique direction of propagation. Similar to an irregular unidirectional wave train, the water-surface elevation is given by Equation 36 with $k_j = (k_j \cos\theta_j, k_j \sin\theta_j)$. Miles (1989) discusses four different methods of assigning directions to each frequency component. In BOUSS-2D, the random direction method was adapted in which wave directions are selected at random from the cumulative distribution of the directional spreading function. With this technique, the frequency spectrum is matched exactly. However, the directional spreading function is matched only in

a global sense over the entire record. The method also does not guarantee a symmetric directional distribution even when the target distribution is symmetric.

The velocity and flux boundary conditions along the wave generation lines are obtained from the surface elevation time-histories using the linear transfer function approach described previously in Equations 40 to 44.

Internal wave generation boundaries

In applications where there is significant wave reflection from bathymetric features or structures within the computational domain, it is desirable to absorb the waves that propagate back to the wave generation boundary to prevent a buildup of wave energy inside the domain. This can be achieved by modifying the boundary conditions along the wave generation boundary to simultaneously generate and absorb reflected waves (e.g., Van Dongeren and Svendsen 1997). A different approach proposed by Larsen and Dancy (1983) is to generate the waves inside the computational domain and absorb reflected waves in a damping layer placed behind the generation boundary. This approach has been adopted in BOUSS-2D with the governing equations modified to allow for the generation of waves inside the computational domain.

Consider the generation of waves along a horizontal line by a distribution of sources that extend from the seabed ($z = -h$) to the free surface ($z = \eta$). The velocity potential associated with the fluid motion satisfies the Laplace equation everywhere in the fluid except for generation line ($x = x_g$) where there is a point source of fluid mass. The governing equation for the fluid motion can thus be written as:

$$\nabla^2\phi = q(y,z,t)\delta(x - x_g) \tag{51}$$

where $q(y,z,t)$ is the volume flux density. Assuming that the water depth is constant along the generation line, a modified form of the second-order Taylor series expansion of the velocity potential about an arbitrary elevation $z = z_\alpha$ in the water column (Equation 1) can be written as:

$$\phi = \phi_\alpha + \frac{1}{2}\left[(z_\alpha + h)^2 - (z + h)^2\right]\left[\nabla^2\phi_\alpha - q\delta(x - x_g)\right] \tag{52}$$

The horizontal fluid velocities are obtained from the velocity potential as:

$$\boldsymbol{u} = \nabla\phi_\alpha + \frac{1}{2}\left[(z_\alpha + h)^2 - (z + h)^2\right]\nabla\left[\nabla^2\phi_\alpha - q\delta(x - x_g)\right] \tag{53}$$

On a rectangular grid with a finite grid spacing Δx, the delta function can be replaced with $2/\Delta x$. To generate waves with a given velocity profile $u_o(y,z,t)$, the mass and momentum equations along the grid generation line and adjacent velocity points can be written as:

$$\eta_t + \nabla \cdot \int_{-h}^{\eta} \boldsymbol{u} \; dz = \frac{2}{\Delta x} \int_{-h}^{\eta} u_o \; dz \tag{54}$$

$$\boldsymbol{u}_{\alpha t} + g\nabla\eta + (\boldsymbol{u}_\alpha \cdot \nabla) \, \boldsymbol{u}_\alpha + \frac{1}{2}\left[(z_\alpha + h)^2 - h^2\right] \left[\nabla(\nabla \cdot \boldsymbol{u}_{\alpha t} - 2u_{o\alpha,\,t}/\Delta x)\right] = 0 \tag{55}$$

Some previous investigators (e.g., Larsen and Dancy 1983) introduced a point source for fluid flow into the continuity equation. It is, however, important to apply a correction to the momentum equations to account for higher-order spatial derivatives across the generation line.

Damping regions

Waves propagating out of the computational domain are absorbed in damping regions placed around the perimeter of the computational domain. Damping layers can also be used to model the partial reflection from harbor structures inside the computational area. Artificial dissipation of wave energy in damping layers is achieved through the introduction of a term proportional to the surface elevation into the right-hand side of the mass equation:

$$F_{damping\_\eta} = -\mu(\boldsymbol{x})\,\eta \tag{56}$$

and a term proportional horizontal velocity into the right-hand side of the momentum equation:

$$F_{damping\_u} = -\mu(\boldsymbol{x})\,\boldsymbol{u}_\alpha \tag{57}$$

where $\mu(\mathbf{x})$ is the damping strength with units of s^{-1}. Introduction of the damping terms lead to the nonconservation of mass and momentum in the damping regions. However, extensive tests with different combinations of the damping terms showed that the inclusion of damping terms in both the mass and momentum equation was more effective than just a damping term in the momentum equation.

Numerical simulations to evaluate the performance of the damping layer showed that waves could be effectively damped out in a layer half a wavelength wide by employing a quadratic variation of $\mu(x)$ with a peak value of $30/T$, where T is the wave period. The damping strength has thus been nondimensionalized by $30/T$, i.e.,

$$\mu_{nd}(\boldsymbol{x}) = \frac{T}{30}\mu(\boldsymbol{x}) \tag{58}$$

where $\mu_{nd}(x)$ is a nondimensional damping coefficient that is allowed to vary from 0 to 1. Figure 5 shows the variation of the reflection coefficient with damping coefficient for different relative widths (w/L) of the damping layer, where w is the width of the damping layer and L is the wavelength. It should be pointed
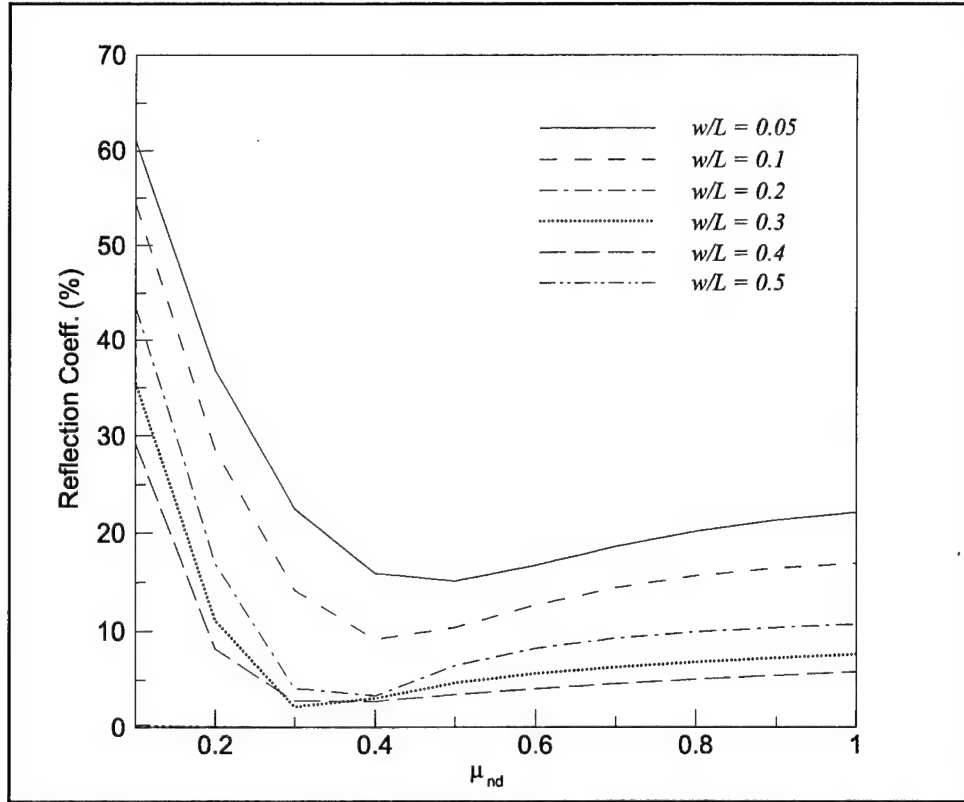
Figure 5.   Variation of reflection coefficient with damping coefficient

out that the results presented in Figure 5 are for normally incident waves. Different reflection coefficients would be obtained for obliquely incident waves.

Flow through porous structures

The Boussinesq equations have also been modified to simulate partial wave reflection and transmission through surface-piercing porous structures such as breakwaters. The modified equations for the porous region can be written in terms of either the velocity in the pores or the volume-averaged (discharge) velocity. In order to easily match velocities and fluxes across the water/porous structure interface, the equations for the porous region are written in terms of the discharge velocity. Ignoring inertial effects, the modified form of the equations for the porous region are obtained by replacing u with u/n, where n is the porosity, and including a term to account for energy dissipation inside the structure:

$$\eta_t + \nabla \cdot \left(\frac{u_f}{n} \right) = 0 \tag{59}$$

$$u_{\alpha,t} + ng\nabla\eta + u_\alpha \cdot \nabla\left(\frac{u_\alpha}{n}\right) + z_\alpha\left[\nabla\left(u_{\alpha,t} \cdot \nabla h\right) + (\nabla \cdot u_{\alpha,t})\nabla h\right]$$
$$+ \frac{1}{2}\left[(z_\alpha + h)^2 - h^2\right]\nabla\left(\nabla \cdot u_{\alpha,t}\right) + nf_l u_\alpha + nf_t u_\alpha |u_\alpha| = 0 \tag{60}$$

where f_l and f_t are laminar and turbulent friction factors respectively. Engelund (1953) recommended the following empirical relationships for the laminar and turbulent friction factors:

$$f_l = \alpha_o \frac{(1-n)^3}{n^2} \frac{\nu}{d^2} \tag{61}$$

$$f_t = \beta_o \frac{(1-n)}{n^3} \frac{1}{d} \tag{62}$$

where ν is the kinematic viscosity of water, d is the characteristic stone size, and α_o and β_o are empirical constants that range from 780 to 1,500, and 1.8 to 3.6 respectively.

Simulation of Wave Runup

The runup of waves on shorelines provides an important boundary condition for predicting wave-induced currents and sediment transport in the surf zone. The runup limit is also important for determining the minimum crest elevation of coastal structures to prevent overtopping and/or flooding. A simple runup scheme has been implemented in BOUSS-2D. Dry computational cells (land points) are assumed to be porous regions where the phreatic surface elevation and volume-averaged velocities are calculated simultaneously with the fluid motion in the wet cells. When the phreatic surface elevation exceeds the elevation of the land point by a specified threshold, the porous cell is considered flooded and treated as a wet cell during the next time-step. Alternatively, when the free surface elevation drops below a specified threshold above the bottom elevation of a wet cell, the wet cell is assumed to be dry and treated as a porous cell during the next time-step.

Subgrid Turbulence

BOUSS-2D optionally provides a mechanism to simulate the turbulence and mixing that occurs in regions with large gradients in the horizontal velocities such as around the tips of breakwaters. The dissipation term is identical to that used for wave breaking, i.e., Equation 16. The eddy viscosity is given by Smagorinsky's (1963) formulation with the turbulent length scale proportional to the grid size. It can be written as:

$$\nu_t = C_s^2 \Delta x \Delta y \left[\left(u_{\alpha,x}\right)^2 + \left(v_{\alpha,y}\right)^2 + \frac{1}{2}\left(u_{\alpha,y} + v_{\alpha,x}\right)^2 \right] \qquad (63)$$

where C_s is an empirical constant.

4 Setting Up and Running BOUSS-2D

BOUSS-2D is a high-resolution wave model designed for investigating complex wave transformation problems over small regions (1-5 km). It is ideally suited for applications where reflection, diffraction, and/or nonlinear interactions are significant such as near coastal inlets and harbors. For wave propagation over large open areas where the processes of wind-wave generation, shoaling and refraction are dominant, phase-averaged models such as STWAVE (Smith, Sherlock, and Resio 2001) should be used. For periodic harbor oscillations, frequency-domain models such as the elliptic mild-slope model CGWAVE (Demirbilek and Panchang 1998) should be used since time-domain models take longer than frequency-domain models to attain steady-state conditions.

Overview of Model Setup

The basic steps involved in setting up and running BOUSS-2D are:

a. Collect ancillary data such as bathymetric data and wave climate information.

b. Select portion of the ocean to be covered by the numerical model and prepare 2-D rectangular grids containing information on the:

    (1) Seabed elevations over the computational area.

    (2) Damping values for the absorption of outgoing waves at model boundaries (optional).

    (3) Porosity values if porous structures such as breakwaters are inside the computational domain (optional).

    (4) Tidal current distribution over the computational area (optional).

c. Create a simulation parameter file that contains all the information required to run the model. This can be done using the DOS-based interactive program Pre-BOUSS2D or other Windows-based programs.

d. Run the BOUSS-2D model.

e. Analyze the model output and plot the results.

Collection of Bathymetric and Wave Climate Data

The first step in the modeling process is the collection of information on the seabed elevations over the computational area. This can be obtained from hydrographic surveys of the area, digitizing nautical charts, or from digital topographic databases such as those maintained by the National Oceanic and Atmospheric Administration (NOAA).

Wave climate information close to the project site can be obtained from:

a. Long-term wave measurements at the project location.

b. Long-term wave measurements in deeper water with buoys such as those operated by NOAA.

c. Hindcast from long-term wind observations using models such as Wave Model (WAM), Wave Information Steady Wave Model (WISWAVE), or Steady-State Wave Model (STWAVE).

Depending on the source of the wave climate data, simpler wave propagation models such as STWAVE (Smith, Sherlock, and Resio 2001) or Refraction/ Diffraction Model for Spectral Wave Conditioning (REFDIF-S) (Kirby and Ozkan 1994) might have to be run to transfer the wave climate data to the boundary of the computational grid. Statistical techniques (e.g., Borgman 1972) can then be used to reduce the wave climate data to design wave conditions with associated return periods.

Information on tidal water levels and currents near the project site can be obtained using prediction techniques based on long-term tidal observations (e.g., NOAA) or by running more sophisticated circulation models such as Advanced Circulation (ADCIRC) Model for Oceanic, Coastal and Estuarine Waters. If the current speeds exceed 10 percent of the phase velocity of the waves, the currents could significantly modify the wave field and a 2-D circulation model would have to be run to provide the spatial distribution of current speeds over the computational area.

Preparation of Bathymetric Grid File

BOUSS-2D simulates wave propagation over a 2-D Cartesian grid as shown in Figure 6. The computational domain is defined as a rectangular region from (x_{origin}, y_{origin}) to (x_{max}, y_{max}) with uniform grid spacings Δx and Δy in the x and y directions, respectively. The bathymetric grid represents the seabed elevation at each node of the grid with land points defined as positive while water points are defined as negative. To prepare the grid, the spatial extent and spacing of the computational grid have to be selected. Factors to consider in the selection of the grid boundaries and spacing include:
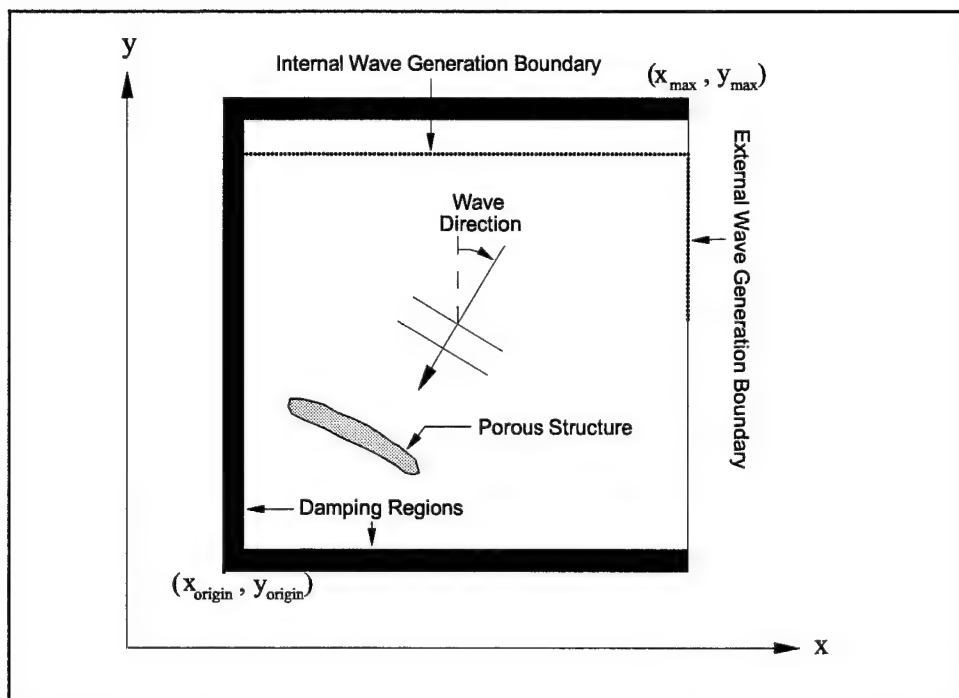
Figure 6. Definition sketch for computational grid

  a. The grid axes should be aligned as much as possible with the
       predominant wave direction.

  b. Points of interest in the computational domain should be kept at least one
       wavelength away from the boundaries to minimize the effect of
       diffraction into the damping layers.

  c. The water depth should be uniform along the wave generation boundary.

  d. The grid spacing should be chosen to resolve the shortest wave period of
       interest (T_{min}) in the shallowest part of the domain (h_{min}). This typically
       corresponds to having at least eight grid points per wavelength in the
       shallow regions and 20 to 30 points per wavelength at the peak wave
       period (T_p) in the deep regions (h_{max}).

  e. The maximum water depth has to be less than half the shortest wave-
       length of interest ($h_{max} \leq L(T_{min})/2$). In regions with relatively deep water
       along the offshore boundary, an artificial maximum depth can be
       imposed in the numerical model to ensure that the shortest waves of
       interest are resolved. For example, if we are interested in modeling a sea
       state with $T_p = 10\ s$ and $T_{min} = 6\ s$ over an area where the water depth
       ranges from 5 m to 100 m, a maximum depth of 28 m can be imposed
       corresponding to $L(T_{min})/2$.

  f. The maximum size of the computational area should be based on the
       amount of available computational resources. For typical PC's or work-
       stations with 100 to 200 MB of virtual memory, the grid size should not
       exceed 500 x 500 grid points. Larger grids can be used at the cost of
       much longer computational times.

Once the grid spacing and extent have been chosen, different algorithms (linear, inverse distance, kriging, etc.) can be used to interpolate the seabed elevation data (x,y,z) onto a uniform rectangular grid. Land regions and impermeable harbor structures are then mapped onto the grid as positive elevations. The grid data should then be saved as an ASCII file in the grid file format described in Appendix D.

Preparation of Damping Grid File

The external boundaries of the computational grid are considered to be fully reflecting wall boundaries unless it is specified as a wave generation boundary. Damping regions have to be placed inside the domain to absorb outgoing waves. The damping regions should be of the order of half a wavelength wide with a quadratic variation of the nondimensional damping coefficient, $\mu_{nd}(x,y)$, from 0 to 1 at the wall boundary.

A utility program GEN_DAMP (Appendix E) has been provided to generate the damping file given the location of the damping layers (North, South, East, or West grid boundaries), the width of the damping layer, and the nondimensional damping strength at the end wall. The damping file is stored as an ASCII file in the grid file format described in Appendix D.

Preparation of Porosity Grid File

Porosity layers are used to simulate partial reflection and transmission through porous structures such as breakwaters. The porosity grid file contains information on the porosity distribution $n(x,y)$ over the computational grid with a value of 1.0 for water points. A porosity value of 0.4 is typically used for breakwaters. Regions with small porosity values ($n < 0.1$) such as breakwater core layers should be treated as impermeable regions and mapped as land points in the bathymetry file.

A utility program MAP_POROSITY (Appendix E) has been provided to create a porosity file given the breakwater boundaries as a set of discrete (x,y) points. The porosity file should be saved as an ASCII file in the grid file format described in Appendix D.

Creation of Simulation Parameter File

All the input parameters required to run BOUSS-2D is stored in an ASCII text file, referred to as a simulation parameter file (.par). The file is a free format file with names of the simulation parameters and associated values not constrained to any particular rows or columns. The full colon (:) character is used at the beginning of lines containing parameter names and values, and the pound (#) character is used to delineate sections of a line with comments. Due to the multitude of options available for the input file, it is recommended that the interactive program Pre_BOUSS2D be used to create it. Pre_BOUSS2D can be run

from an MS-DOS prompt window by typing the program name including the filepath, e.g.,

```
C:\BOUSS2D\BIN\pre_bouss2d
```

The user then interactively types in answers on the keyboard in response to questions posed by the program. Default answers shown in square brackets [...] can be selected by hitting the enter key.

Step 1. Simulation Parameter File
- Enter the name of the output simulation parameter file (.par)

Step 2. Bathymetric Information
- Enter the name of the bathymetry file (.grd)
- Enter storm surge/tidal water level offset in meters

Step 3. Damping Information
- Enter name of damping file (.grd) if there are damping regions in the computational domain

Step 4. Porous Structure Information
Enter the following information if there is a porous structure in the computational domain
- Name of porosity file (.grd)
- Characteristic stone size in porous layer (m)

Step 5. Wave Generation Boundaries
Waves may be generated along one or two boundaries. The boundaries may be external (along boundary of computational grid) or internal (within the computational grid). Internal wave generation boundaries have to be parallel to one of the grid boundaries.

For each wave generation boundary, enter the following information:
- Type of Wave Generation Boundary (External/Internal)

 For External Wave Generation Boundary
- Select grid boundary (North, East, South, or West)
- If generation line exists over part of the boundary, enter the coordinates of the start and end points.

 For Internal Wave Generation Boundary
- Enter orientation of wave generation line (East-West or North-South)
- Enter the x or y coordinate of wave generation line
- If generation line exists over part of boundary, enter the coordinates of the start and end points.

Step 6. Incident Wave Information
Along wave generation boundaries, BOUSS-2D requires the horizontal velocities $u_\alpha(t)$ and flux densities $u_f(t)$ normal to the boundary at each time-step. The time-histories may correspond to regular or irregular, unidirectional or multidirectional waves. The velocity and flux time series can either be synthesized from parametric information (wave height, period, etc.) or derived from an input

surface-elevation time series. The information required to generate the incident wave boundary conditions is described as follows:

- Wave Synthesis Options
  - Synthesize velocity and flux time-histories from parametric information
  - Read in measured surface-elevation time series. The input file has to be in the time series file format described in Appendix D.

- Incident Wave Type
  - Regular Waves
  - Irregular Unidirectional Waves
  - Irregular Multidirectional Waves

Regular Waves
- Wave Height (m) – vertical distance between the wave crest and trough. The incident wave height should not exceed 75 percent of the breaking limit given by the Miche criterion as $H_{break}/L = 0.14 \tanh kh$. When the wave height exceeds 25 percent of the breaking limit, nonlinear effects become important and the time-histories are synthesized using the Boussinesq-Fourier theory discussed in Appendix A.

- Wave Period (s) – time interval between successive wave crests. The incident wave period has to be greater than the limit imposed by the dispersive properties of the Boussinesq equations, i.e., the wavelength calculated from the linear dispersion relation (Equation 10) using the wave period and maximum water depth has to be greater than twice the water depth ($L > 2h_{max}$).

- Wave Direction (deg) – This is the direction the waves propagate into the computational domain from, and is defined in a clockwise manner from the northern boundary of the grid as shown in Figure 6. For example, waves propagating into the domain normal to the western boundary would have a direction of 270 deg. The incident wave direction also has to be within ± 85 deg of the normal to the wave generation boundary.

- Number of Wave Cycles – This determines the time period over which output parameters such as the significant wave height and mean velocities are calculated after steady-state conditions have been established in the computational domain. The recommended range is from 10 to 50.

Irregular Waves
- Type of Wave Spectrum
  - JONSWAP
  - Bretschneider
  - Pierson-Moskowitz
  - TMA
  - Ochi-Hubble

Different spectral parameters will be input depending on the selected wave spectrum. The most commonly used parameters are described in the following paragraphs. Detailed information on the different wave spectra and their associated parameters are provided in Appendix B.

- Significant Wave Height, H_{mo} (m) – Defined as four times the square root of the zeroth moment of the spectrum, i.e., $H_{mo} = 4\sqrt{m_0}$, where $m_0 = \int_0^\infty S_\eta(f)df$. H_{mo} is equivalent to the average height of the highest one-third of the waves ($H_{1/3}$) for moderate sea states in deep water with a Rayleigh wave height distribution. The input significant wave height should not exceed 50 percent of the breaking limit given by the Miche criterion based on the peak frequency of the spectrum, i.e., $H_{mo,max}/L_p = 0.07 \tanh k_p h$.

- Peak Wave Period, T_p (s) – Inverse of the cyclic frequency at which the wave spectrum is a maximum ($T_p = 1/f_p$)

- Minimum Wave Period, T_{min} (s) – The incident wave spectrum is set to zero at all frequencies greater than $1/T_{min}$ with the truncated wave spectrum optionally rescaled to match the target significant wave height. The minimum wave period has to be greater than the limit imposed by the dispersive properties of the Boussinesq equations, i.e., the wavelength based on T_{min} and h_{max} has to be greater than twice the maximum water depth [$L(T_{min}) > 2h_{max}$].

- Maximum Wave Period, T_{max} (s) – The incident wave spectrum is set to zero at all frequencies less than $1/T_{max}$. The maximum wave period is used to separate infragravity waves from wind-generated waves and has a default value of 25 s (prototype).

- Wave Direction (deg) – This is the direction the waves propagate into the computational domain from, and is defined in a clockwise manner from the northern boundary of the grid as shown in Figure 6. For example, waves propagating into the domain normal to the western boundary would have a direction of 270 deg. The incident wave direction also has to be within ± 85 deg of the normal to the wave generation boundary.

- Synthesized Time Series Duration – This is the recycling period of the Fourier series used to synthesize the time-histories and corresponds to the time period over which output parameters such as the significant wave height and mean velocities are calculated after steady-state conditions have been established in the computational domain. The recommended range is from 50 to 100 wave periods.

- Random Number Seed – The seed of the random number generator used to select phase angles for the different Fourier components. Different seeds can be used to obtain different time records from the same wave spectrum.

Multidirectional Waves

In addition to specifying spectral parameters, the user has to select additional parameters to describe the directional distribution of wave energy. The different directional distributions are discussed in Appendix C.

- Type of Directional Spreading Function
  - Wrapped-Normal
  - Cosine-Power

- Standard Deviation, σ_θ (deg) – The standard deviation of the Wrapped-Normal directional spreading function. The allowable range is from 5 deg to 50 deg with 10 deg representing narrow-band swell-type conditions and 30 deg representing broader, local wind-generated seas.

- Spreading Index, s – Describes the degree of directional spreading for the Cosine-power directional distribution. The allowable range of the spreading index is from 0 to 65 with $s = 2$ representing broad, local wind-generated seas and $s = 15$ representing narrow-band swell-type conditions.

- Principal Wave Direction, θ_p (deg) – This is the direction corresponding to peak of the directional spreading function. The wave direction is defined in a clockwise manner from the northern boundary of the grid as shown in Figure 6. The principal direction has to be within ± 30 deg of the normal to the wave generation boundary.

- Maximum Propagation Direction, θ_{max} (deg) – This is the maximum wave propagation direction relative to the normal to the wave generation boundary as shown in Figure 7. The directional distribution is truncated at $\pm\theta_{max}$ and renormalized. As pointed out by Sand and Mynett (1987), θ_{max} also defines the limited area in the computational domain over which homogenous conditions exist, i.e., all wave directions are included. Diffraction effects will further reduce the size of the spatially homogenous region. The recommended value is two to three times the standard deviation of the directional distribution.

It should also be noted that when using more than one wave generation boundary, different spectral/directional parameters might be specified for the individual boundaries. However, the duration of the synthesized or input time record must be the same for both boundaries.

Step 7. Current Field
If tidal currents are significant over the computational area, the spatial distribution of the currents $U(x,y)$ should be stored as an ASCII file in the grid file format (.grd) described in Appendix D. The user should then enter the name of the file containing the velocity data.
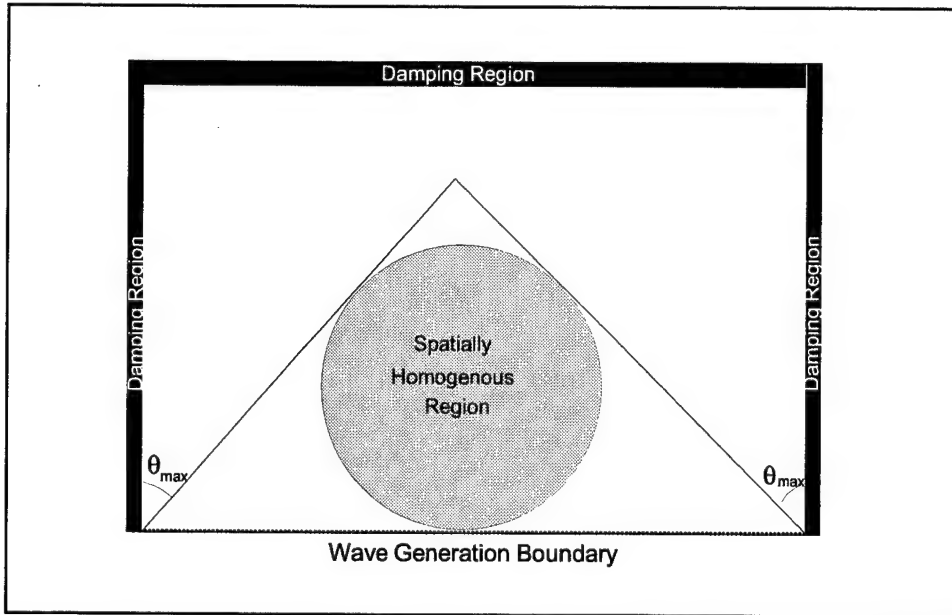
Figure 7. Sketch showing spatially homogenous region for multidirectional waves

Step 8. Simulation Parameters

- Duration of Numerical Simulation (s) – This is equal to time required for the storm waves to propagate from the wave generation boundary to the farthest points of interest in the model area and establish steady-state conditions, i.e., warm-up period plus the duration of the synthesized or input time record specified in Step 6.

- Simulation Time-Step (s) – The time-step should be selected based on the stability considerations, i.e., the Courant number C_r has to be less than 1.0:

$$C_r = \sqrt{\left[C^2 \Delta t^2 \left(\frac{1}{\Delta x^2} + \frac{1}{\Delta y^2} \right) \right]} < 1.0$$

where C is the phase velocity calculated using the maximum water depth (h_{max}) and the average zero-crossing period of the incident waves. It is recommended that the Courant number be kept within the range 0.5 to 0.7, which typically corresponds to 30 to 50 points per wave period. For plunging waves on steep slopes, it may be necessary to use up to 100 points per wave period to simulate the rapid changes in wave shape irrespective of the Courant number.

- Chezy Coefficient – Bottom friction factor with a default value of 30. Should be kept between 20 and 1,000.

- Model Equations Option (Weakly Nonlinear/Fully Nonlinear) – Select either weakly nonlinear model of Nwogu (1993) or the fully nonlinear model of Nwogu (1996). The fully nonlinear model is computationally more intensive

than the weakly nonlinear model and should only be used to investigate highly asymmetric waves in shallow water, wave-induced currents, and wave-current interaction.

- Wave Breaking Option (Y/N) – Wave breaking should be enabled if the significant wave height is going to be greater than half the water depth in the shallowest regions of the computational area ($H_{mo} > h_{min}/2$).

- Turbulent Length Scale, l_t (m) – Controls the rate of wave energy dissipation for breaking waves. Should be set equal to the significant wave height ($l_t = H_{mo}$) for irregular waves or the wave height ($l_t = H$) for regular waves.

- Smagorinsky Constant C_s – Eddy viscosity coefficient for subgrid turbulence. To avoid excessive dissipation of the waves, C_s should be kept between 0 and 0.5. The default value is 0.0.

- Wave Runup Option (Y/N) – The runup scheme used in the numerical model is designed to simulate subcritical flow conditions on mild slopes. It cannot resolve details of supercritical flow on steep slopes. The runup option should only be used with the fully nonlinear model equation option.

- Minimum Flooding Depth – Parameter used control the stability of runup computations. Its value should be of the order of one-hundredth of the incident wave height ($H/100$).

Step 9. Output Data

BOUSS-2D calculates the time-dependent evolution of the water-surface elevation and horizontal velocities over a rectangular grid. For most simulations, it would require an excessive amount of disk space to store the surface elevation and velocity data at every grid point for all the simulation time-steps. To minimize disk storage requirements, the program outputs the time-averaged values of the variables over the entire grid or time-histories of the variables at specified grid points in the computational domain. All output files start with a prefix (xxx) specified by the user. The different output file options are given in the following paragraphs:

2-D Spatial Output

- Mean water level $\bar{\eta}(x, y)$ distribution over the computational grid (xxx_mwl.grd) – The free surface fluctuations are averaged over the duration of the synthesized or input time record, t_w, specified in Step 6, i.e.,

$$\bar{\eta}(x, y) = \frac{1}{N} \sum_{t_s - t_w}^{t_s} \eta(x, y, t)$$

where $N = t_w/\Delta t$ and t_s is the duration of the numerical simulation specified in Step 8. The user should make sure that the duration of the numerical simulation is long enough to establish steady-state conditions in the numerical wave basin.

- Significant wave height distribution $H_{mo}(x,y)$ over the entire computational grid (xxx_Hs.grd) – The significant wave height is calculated as four times standard deviation of the water-surface elevation over the duration of the synthesized or input time record, i.e.,

$$H_{mo}(x,y) = 4\sqrt{\left[\frac{1}{N-1}\sum_{t_s-t_w}^{t_s}\eta^2(x,y,t) \; - \; \bar{\eta}^2(x,y)\right]}$$

For regular waves, the wave height can be obtained from the significant wave height as $H_{mo}/\sqrt{2}$. It should noted that there could be differences between the significant wave height estimated from the standard deviation of the time record and those obtained using zero-crossing analysis especially for highly asymmetric waves in shallow water.

- The time-averaged or mean current $\bar{u}_\alpha(x,y)$ over the entire computational domain (xxx_uv.grd).

$$\bar{u}_\alpha(x,y) = \frac{1}{N}\sum_{t_s-t_w}^{t_s} u_\alpha(x,y,t)$$

The time-averaging procedure is also carried out over the duration of the synthesized or input time record.

Time Series Output

- Time series of the water-surface elevation $\eta(t)$ and two components of the horizontal velocity $u_\alpha(t)$, $v_\alpha(t)$ at specified (x,y) locations in the grid. The time series files are named xxx_eta.ts1, xxx_u.ts1, and xxx_v.ts1.

Animation Output

- Time-dependent output of the water surface elevation $\eta(x,y,t)$ and horizontal velocities $u_\alpha(x,y,t)$ over a specified area and time period. The user specifies the coordinates of the lower left-hand corner (x_1,y_1), upper right-hand corner (x_2,y_2), and grid skip interval for the output grid area, and the start time, end time, and time-step for the output time period. The files are named xxx.eta and xxx.uv for the surface elevation and velocities, respectively. The animation files could be large and should be used judiciously. The size of the surface elevation output file in bytes can be calculated as 4 x (number of grid points) x (number of time-steps). The velocity file is twice the size of the surface elevation file.

Step 10.

After entering all the information, Pre-BOUSS2D creates a simulation parameter file. The simulation parameter file is an ASCII file that can be edited using

standard text editors (WordPad, etc.). Changes can be made to the wave simulation parameters (e.g., wave height, period, direction, time-step, etc.) and the file saved under a new name. A sample output of the simulation parameter file is shown as follows:

```
###############################################################
# BOUSS2D Simulation Parameter File:   barbers_irr_t12.wsp
# Written By:              John. E. Hacker
# Creation Date:           Fri, Sep 15, 2000
# Creation Time:                      04:16 PM
###############################################################
#
# Bathymetric Grid Parameters
:BATHY_FILE                bathy_barbers.grd
:TIDAL_OFFSET              0               # metres
#
# Damping Parameters
:DAMPING_FILE              damp_barbers.grd
#
# WaveMaker #1 Parameters
:START_WAVEMAKER
:     WM_POS_X1            600             # metres
:     WM_POS_Y1            0               # metres
:     WM_POS_X2            600             # metres
:     WM_POS_Y2            2500            # metres
:     WAVE_TYPE       Irreg_uni    # Regular, Irreg_uni, or Irreg_multi
:     TIME_SERIES_OPTION   synthesize      # file or synthesize
:     WAVE_DIRECTION       270             # degrees
:     TIME_SERIES_DURATION 1800            # seconds
:     RANDOM_NUMBER_SEED   25136827
:     SPECTRAL_TYPE        JONSWAP    # JONSWAP, BRET, PM, TMA or OCHI
:     JONSWAP_OPTION       Hs              # Hs, Sigma, or Gamma
:     WAVE_HEIGHT_SIG      3               # metres
:     WAVE_PERIOD_PEAK     12              # seconds
:     WAVE_PERIOD_MIN      8               # seconds
:     WAVE_PERIOD_MAX      24              # seconds
:     GAMMA                3.3
:     PHILLIPS             0.0081
:     RESCALE_SPECTRUM     NO              # YES or NO
:END_WAVEMAKER
```

```
#
# Simulation Parameters
#
:DURATION                2800          # seconds
:TIME_STEP               0.2           # seconds
:RAMP_DURATION           12            # seconds
:CHEZY_COEFF             30
:NONLINEAR_OPTION        STRONG        # WEAK or STRONG
:WAVE_RUNUP_OPTION       NO            # YES or NO
:WAVE_BREAKING_OPTION    YES           # YES or NO
:TURB_LENGTH_SCALE       3             # metres
#
# Output Parameters
:FILE_NAME_PREFIX        irr_h3t12
:HS_FILE                 irr_h3t12_Hs.r2s  # Hs output file
:MEAN_UV_FILE            irr_h3t12_mean_UV.r2v # Mean UV output file
#
# Surface Elevation (ETA) File Parameters
:SAVE_ETA
:    ETA_FILE            irr_h3t12.wse
:    START_TIME          0             # seconds
:    END_TIME            1800          # seconds
:    SAVE_TIME_STEP      1             # seconds
:    SAVE_FULL_GRID      YES           # YES or NO
:    GRID_STEP           1
:END_SAVE_ETA
#
:SAVE_TIMESERIES
:    TS_X                1220          # metres
:    TS_Y                890           # metres
:END_TIMESERIES
#
```

Running BOUSS-2D

After creation of the simulation input file, BOUSS-2D can be run from an MS-DOS command prompt window by typing:

```
C:\BOUSS2D\BIN\bouss2d input_file_name
```

After carrying out computations for 10 time-steps, the program displays an estimate of the run time. The run time could vary, however, depending on other processes running on the computer at the same time.

Time Series Data Analysis

BOUSS-2D outputs the significant wave height and mean current distribution over the entire computational grid. For some applications, it might be necessary to analyze the time series data at specific grid points to obtain frequency or directional wave spectra, wave height statistics, reflection coefficients, etc. Hughes (1993) extensively discusses time and frequency domain analysis techniques for time series data in a laboratory setting. Similar techniques can be applied to time series output from the numerical model.

Standard statistical analysis techniques can be applied to the surface elevation or velocity time records to obtain the mean, standard deviation, skewness, and kurtosis of the time records. The skewness of the surface elevation, η, and its time derivative, η_t, can be used to quantify the degree of wave asymmetry or nonlinearity in shallow water. Zero-crossing analysis techniques can be used to define the heights and periods of individual wave cycles within an irregular wave record. These can be analyzed to obtain parameters such as the root-mean-square wave height, H_{rms}, average height of the highest one-third of the waves, $H_{1/3}$, or the average wave period, T_{av}.

Standard spectral analysis techniques can be used to obtain the surface elevation or velocity spectra. These can be analyzed to obtain parameters such as the significant wave height, H_{mo}, and spectral peak period, T_p. Different techniques have been proposed for the estimation of directional wave spectra using either an array of wave gauges (e.g., Nwogu 1989) or collocated measurements of the surface elevation and horizontal velocities (e.g., Nwogu et al. 1987). Collocated time series of the surface elevation and horizontal velocities can also be used to estimate the reflection coefficients using the technique described in Hughes (1993).

5   Model Validation

Wave Propagation through a Breakwater Gap

We initially evaluated the ability of BOUSS-2D to simulate the propagation of waves through a gap into a rectangular harbor basin. The basin is 1,200 m wide, 600 m long, and 10 m deep. The width of the opening at the harbor entrance is 120 m.

The first case considered is a regular wave with period $T = 7$ s propagating in a direction normal to the breakwaters. The corresponding ratio of the gap width, B, to wavelength, L, is 2. Boussinesq model simulations were carried out using grid spacings $\Delta x = \Delta y = 3$ m and time-step size $\Delta t = 0.15$ s. A 60-m-wide damping layer was placed around the perimeter of the basin to absorb outgoing waves. Figure 8 shows a snapshot of the instantaneous water-surface elevation produced by the BOUSS-2D model.

The normalized wave height distribution predicted by BOUSS-2D is compared with the numerical solution of Isaacson and Qu (1990) in Figure 9. Isaacson and Qu (1990) used a boundary integral technique to solve the 2-D Helmholtz equation, which is a reduced form of the mild-slope equation for water of constant depth. Good agreement is generally observed between the wave height predictions from the numerical models. Small oscillations can be seen in the Boussinesq model predictions, especially for the smaller wave height contours. This is due to partial wave reflection from the radiation boundaries. Reflection coefficients of the order of 5 to 10 percent at the boundaries have been observed to cause such oscillations in wave height contour lines (Isaacson and Qu 1990)

We next investigated the propagation of irregular multidirectional waves through the gap. The sea state is characterized by a JONSWAP wave spectrum with peak period $T_p = 7$ s and peak enhancement factor $\gamma = 3.3$. A wrapped-normal distribution with a standard deviation of 20 deg was used for the directional distribution of wave energy. The double-summation method was used to synthesize time-histories of velocity fluxes along the incident wave boundary for the BOUSS-2D simulations.

Figure 10 shows a snapshot of the instantaneous water-surface elevation produced by the BOUSS-2D model. The normalized wave height distribution predicted by BOUSS-2D is compared with the numerical solution of Isaacson and Qu (1990) in Figure 11. Good agreement is observed. As expected, the
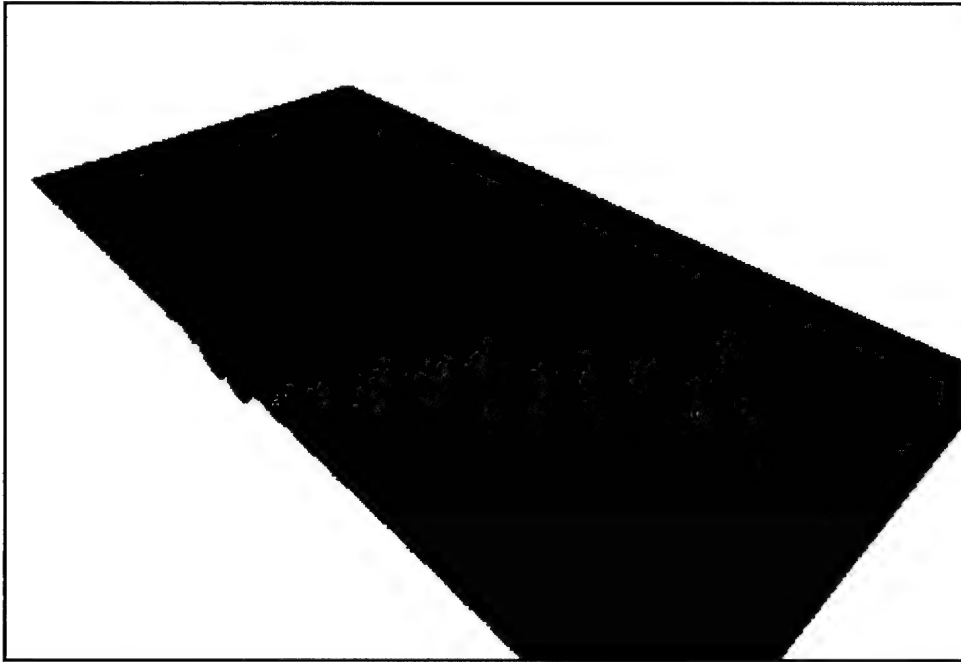
Figure 8.   3-D view of instantaneous water-surface elevation for regular waves
             propagating through a breakwater gap (T = 7 s, h = 10 m, B/L = 2)
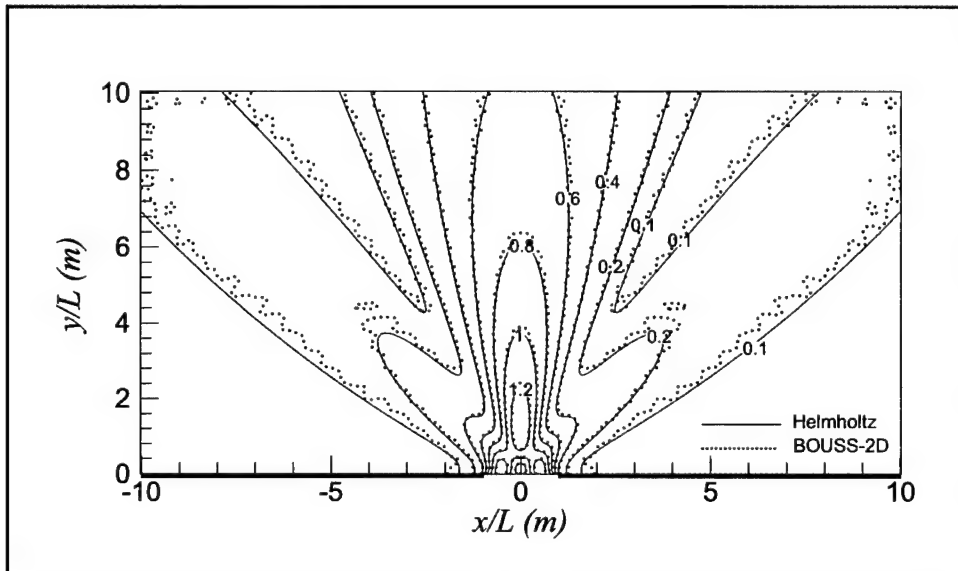

Figure 9.   Relative wave height contours for regular waves propagating through
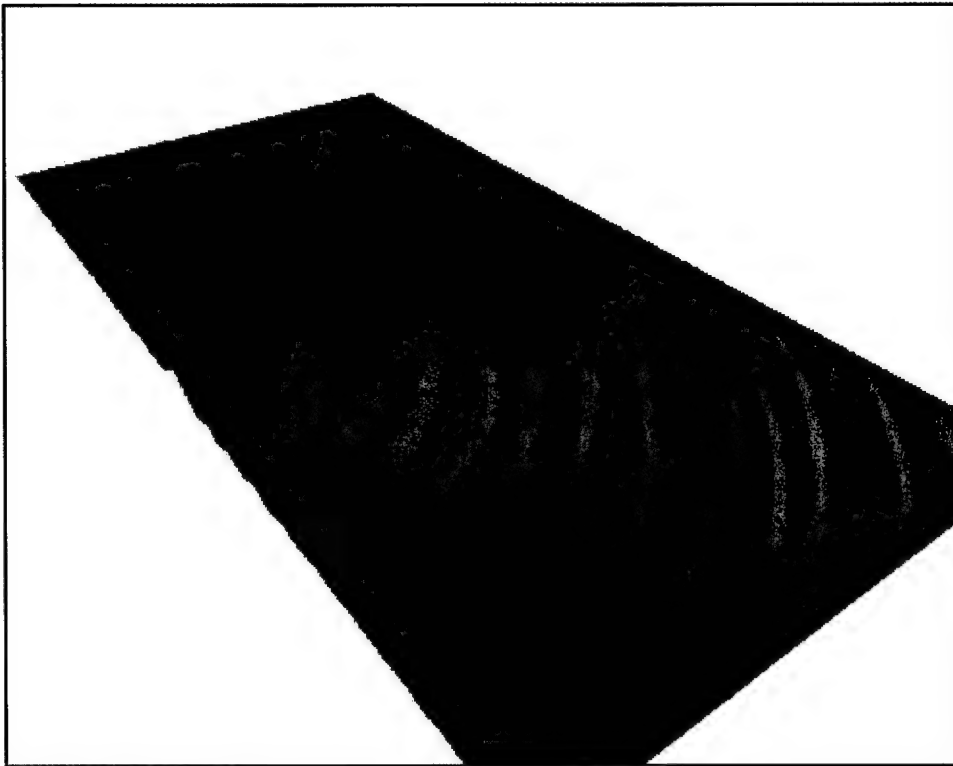   a breakwater gap (T = 7 s, h = 10 m, B/L = 2)

Figure 10. 3-D view of instantaneous water-surface elevation for multidirectional waves propagating through a breakwater gap (T_p = 7 s, σ_θ = 20°, h = 10 m, B/L_p = 2)
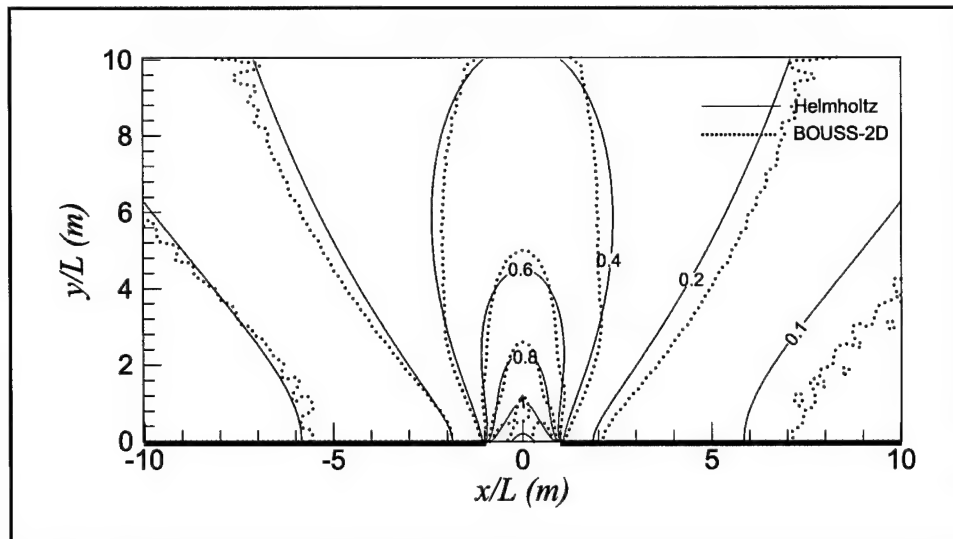
Figure 11. Relative wave height contours for multidirectional waves propagating through a breakwater gap (T_p = 7 s, σ_θ = 20°, h = 10 m, B/L_p = 2)

directional spreading of wave energy leads to larger wave heights in the sheltered area behind the breakwaters and smaller wave heights along the principal direction of the waves.

Multidirectional Wave Propagation over a Shoal

Laboratory experiments on the transformation of irregular multidirectional waves over an elliptical shoal were carried out by Vincent and Briggs (1989). The experimental layout is shown in Figure 12, and consists of an elliptical shoal placed in a 0.4572-m-deep basin. The boundary of the shoal is an ellipse defined by:

$$\left(\frac{x - x_c}{3.96}\right)^2 + \left(\frac{y - y_c}{3.05}\right)^2 = 1 \tag{64}$$

where (x_c, y_c) are the coordinates of the center of the shoal and are given by $x_c = 13.72$ m and $y_c = 6.10$ m. The water depth over the shoal is given by:

$$h(x,y) = 0.9144 - 0.7620 \left\{1 - \left(\frac{x - x_c}{4.95}\right)^2 - \left(\frac{y - y_c}{3.81}\right)^2\right\}^{0.5} \tag{65}$$

The minimum water depth over the shoal is 0.1524 m. Tests were carried out for various regular and irregular, unidirectional and multidirectional waves. For irregular waves, the TMA spectrum was used to describe the frequency distribution of wave energy, while the wrapped-normal distribution was used for the directional spreading function. Water-surface elevation data were collected at five transects located at distances of 3.05 m, 6.10 m, 9.14 m, 12.19 m, and 15.24 m from the wavemaker as shown in Figure 12.

The numerical basin for the BOUSS-2D model simulations is 31.5 m wide, 27 m long, with a uniform grid spacing of 0.1 m. Two-meter-wide damping layers were placed around the perimeter of the basin to absorb outgoing waves. Two representative test cases were selected for the model-data comparisons. Test case N1 is characterized by a TMA spectrum with significant wave height $H_{mo} = 0.0775$ m, peak period $T_p = 1.3$ s, peak enhancement factor $\gamma = 2$, and a narrow directional distribution with standard deviation $\sigma_\theta = 10$ deg. Test case B1 is characterized by a TMA spectrum with significant wave height $H_{mo} = 0.0775$ m, peak period $T_p = 1.3$ s, peak enhancement factor $\gamma = 2$, and a broad directional distribution with standard deviation $\sigma_\theta = 30$ deg. Time-histories of the velocity boundary conditions along the wavemaker were synthesized for a duration of 130 s, corresponding to 100 wave periods. Simulations were carried out using a time-step size $\Delta t = 0.025$ s.
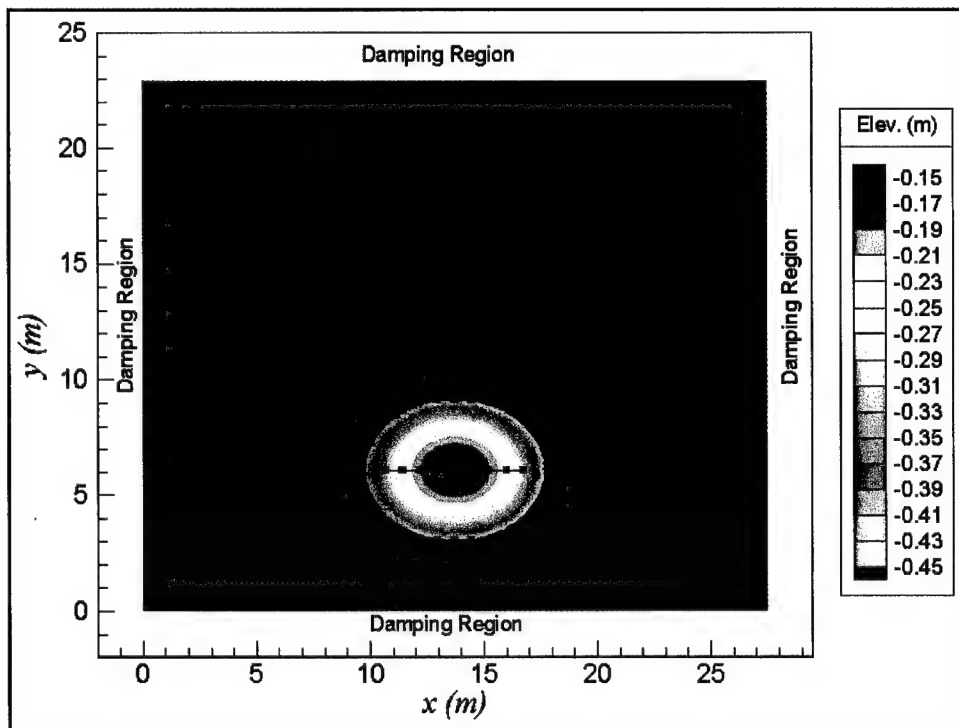
Figure 12. Plan view of bathymetry and layout for Vincent-Briggs shoal experiments

Figure 13 shows a snapshot of the instantaneous water-surface elevation over the shoal predicted by the BOUSS-2D model for test case N1. The focusing of wave energy behind the shoal can clearly be seen. The corresponding 2-D map of the normalized wave height distribution over the computational grid is shown in Figure 14. The predicted wave height variation along transects 3 and 4 are compared to the experimental results in Figures 15 and 16, respectively. BOUSS-2D significantly overpredicted the wave height amplification along transect 3 with differences of the order of 20 to 30 percent. A better match was obtained along transect 4 where the wave height amplification was lower. The reason for such large discrepancies along transect 3 is still unclear. Similar discrepancies were obtained with the CGWAVE model (Demirbilek and Panchang 1998) as shown in Figures 15 and 16. For the broader directional distribution test case B1, reasonable agreement was obtained between the model and the lab data as shown in Figures 17 and 18 with differences of the order of 10 percent.

Wave Breaking in Bimodal Sea States

Bimodal sea states consisting of swell and local wind-generated components occur frequently along most U.S. coastlines (Thompson 1980). Smith and Vincent (1992) investigated the shoaling and breaking of dual-wave systems on a constant slope beach. They found that the higher frequency component decayed much faster in the presence of the low-frequency waves, while the lower frequency component appeared to be unaffected by the presence of high-frequency waves. Smith and Vincent (1992) investigated the applicability of spectral energy
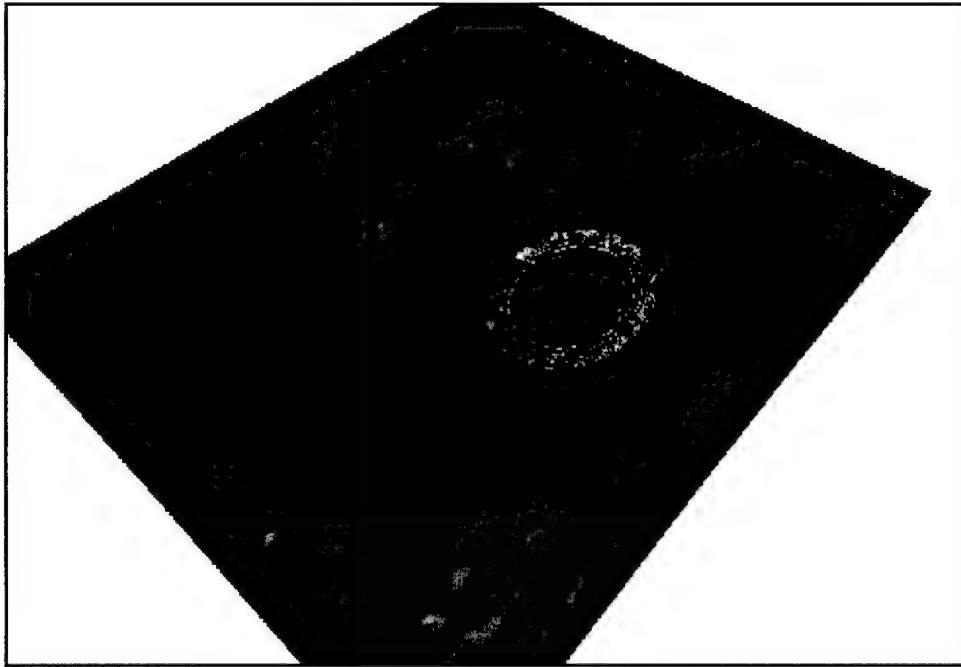
Figure 13. 3-D view of multidirectional wave propagation over a shoal for test
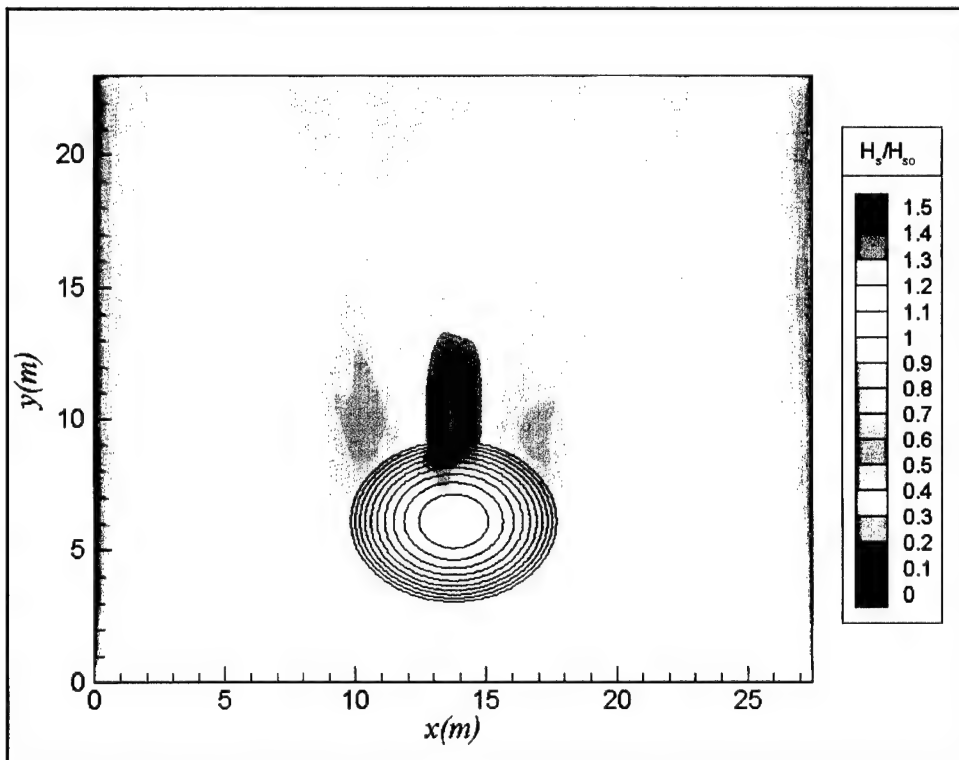case N1 (H_{mo} = 0.0775 m, T_p= 1.3 s, σ_θ = 10 deg)

Figure 14. Normalized wave height distribution for multidirectional wave
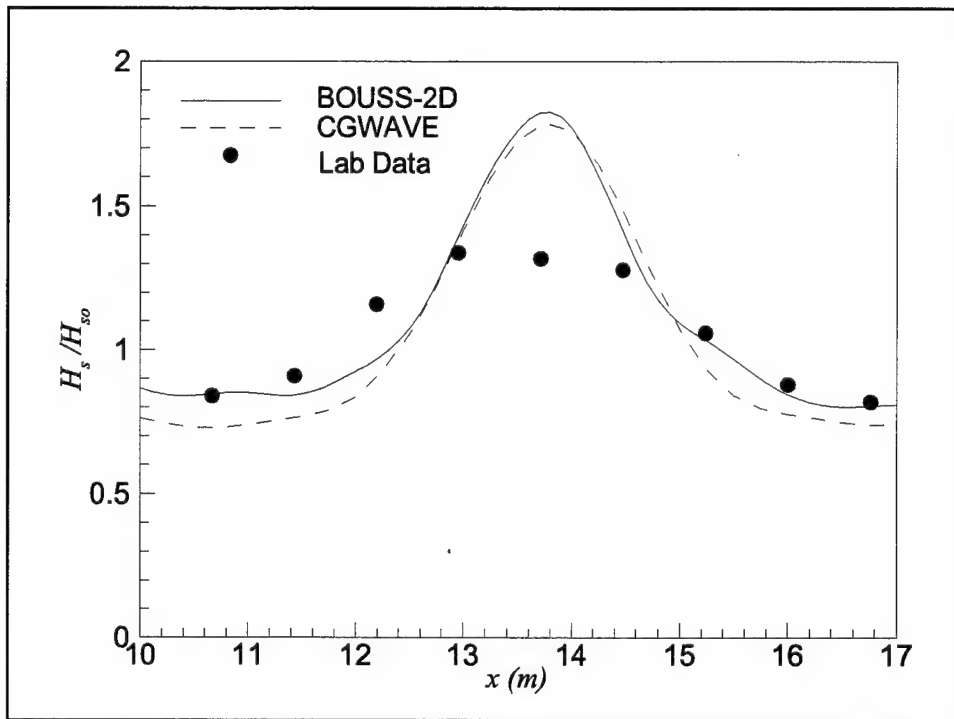propagation over a shoal for test case N1

Figure 15. Normalized wave height distribution along transect 3 for test case N1
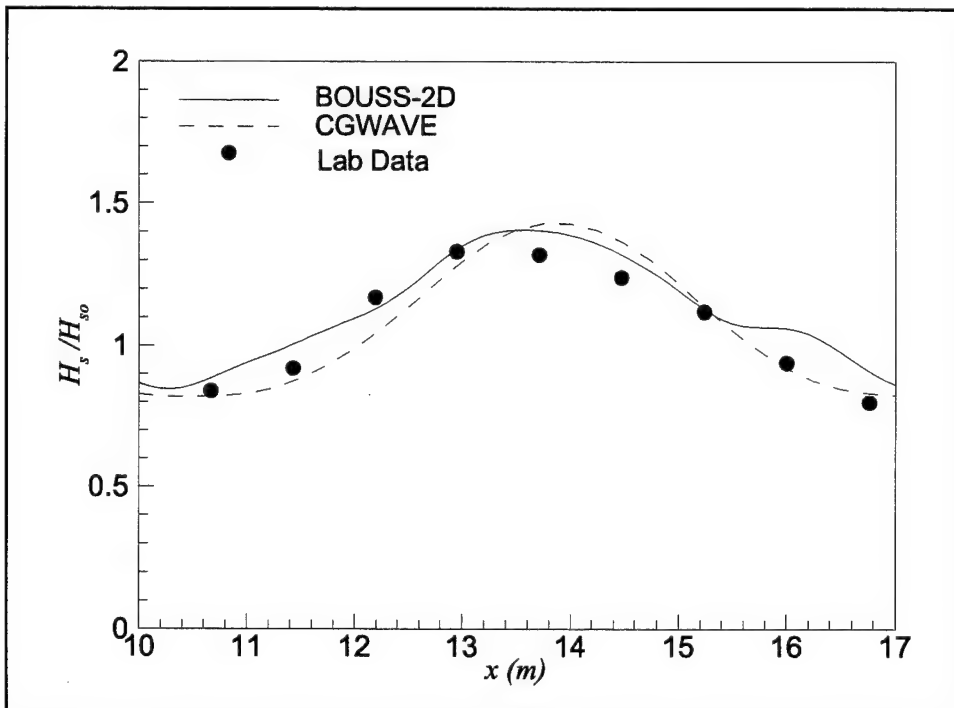

Figure 16. Normalized wave height distribution along transect 4 for test case N1
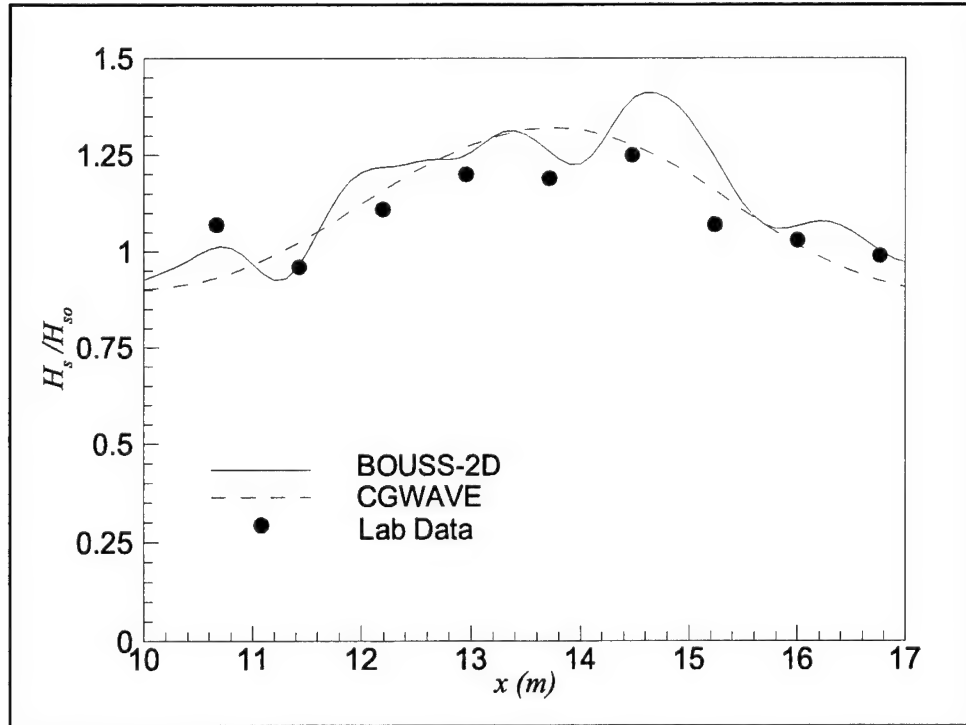
Figure 17. Normalized wave height distribution along transect 3 for test case B1
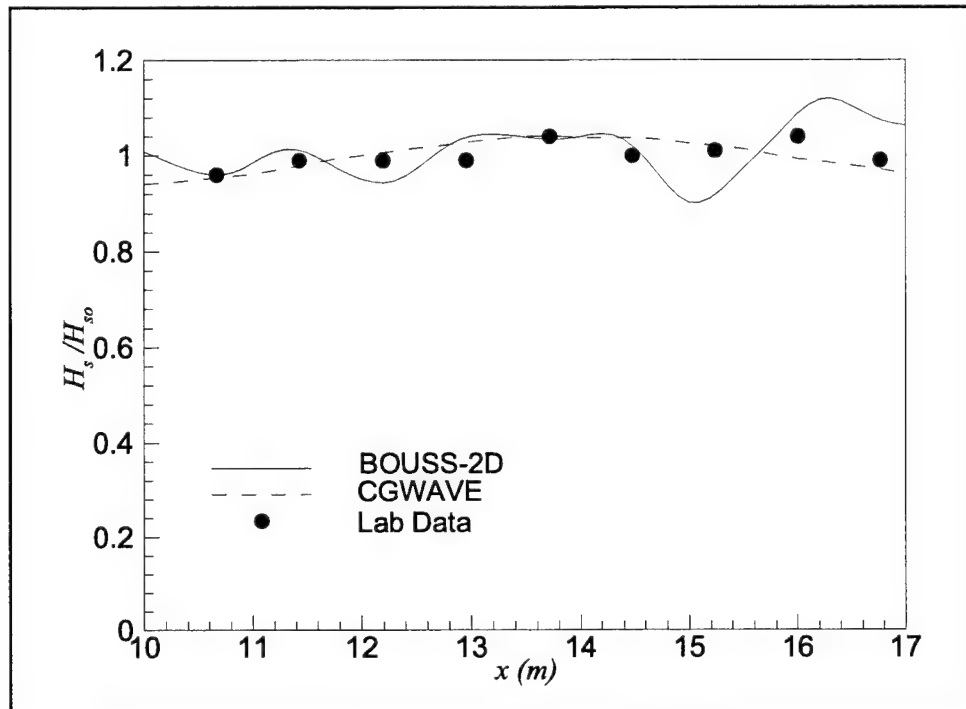

Figure 18. Normalized wave height distribution along transect 4 for test case B1

conservation models with a depth-limited breaking criterion and simpler tech-
niques such as shoaling the component wave systems independently of each
other and superimposing the results. None of these techniques could reproduce
the observed changes to the wave spectrum.

Boussinesq model simulations were carried out for test case 7 in the Smith
and Vincent experiments. The sea state is composed of two irregular wave
components described by TMA spectra with $H_{mo,1}$ = 7.6 cm, $T_{p,1}$ = 2.5 s, $H_{mo,2}$ =
13.2 cm, $T_{p,1}$ = 1.75 s, and γ = 20. The numerical wave flume is 41 m long and
consists of a 20-m-long constant-depth region and a 1:30 planar beach. The water
depth in the constant depth section of the flume was 0.61 m. The measured time
series at the offshore gauge was used to generate velocity boundary conditions
for the numerical model. A grid spacing of 0.125 m and time-step size of 0.04 s
was used for the numerical simulations.

Figures 19 to 22 show comparisons of the measured and predicted wave
spectra at gauges located in water depths of 61 cm, 18.3 cm, 9.1 cm, and 6.1 cm.
Although the higher frequency component dominates the incident wave spectrum
with 67 percent of the wave energy at h = 61 cm, its energy is preferentially dis-
sipated with the lower frequency component becoming dominant at the shallow
depth of 6.1 cm. The Boussinesq model is able to reproduce the observed trends
in the experimental data. The primary reason for the preferential reduction in
energy of the high-frequency component is due to the nonlinear cross-spectral
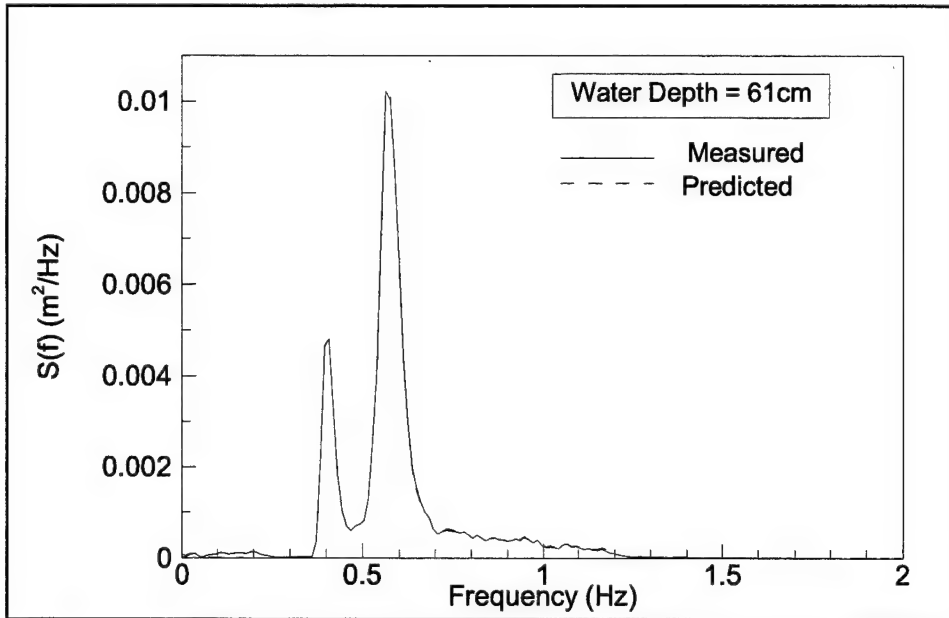transfer of energy during the shoaling process.

Figure 19. Measured and predicted wave spectra at Gauge 1 for bimodal sea
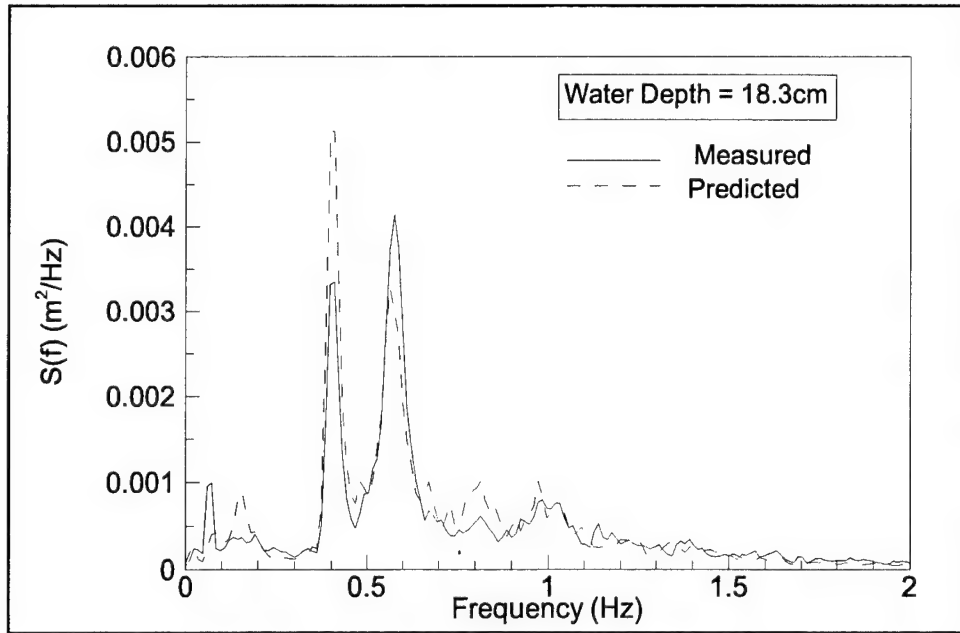state shoaling on a constant slope beach

Figure 20. Measured and predicted wave spectra at Gauge 4 for bimodal sea state shoaling on a constant slope beach
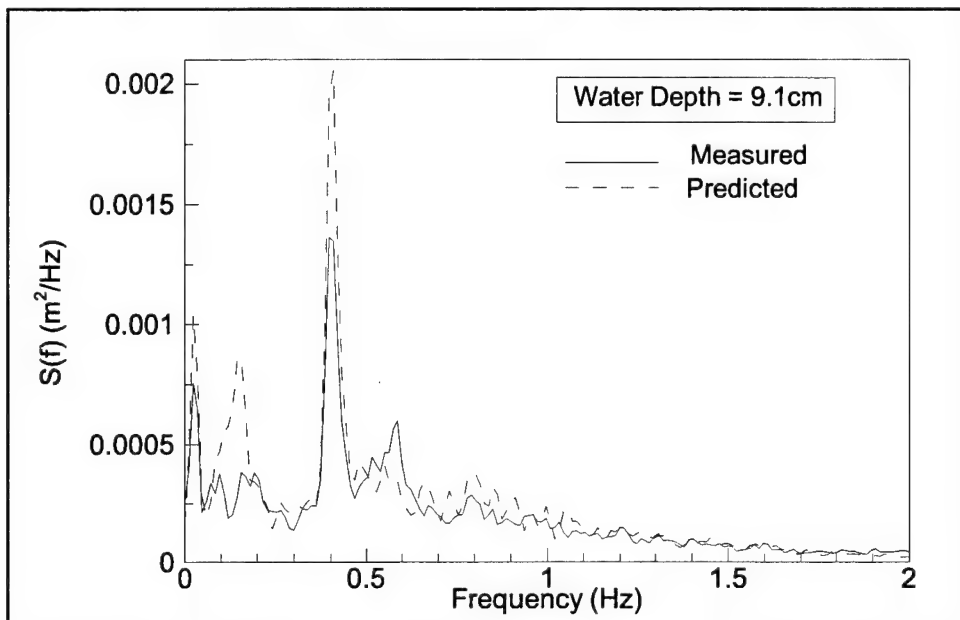

Figure 21. Measured and predicted wave spectra at Gauge 7 for bimodal sea state shoaling on a constant slope beach
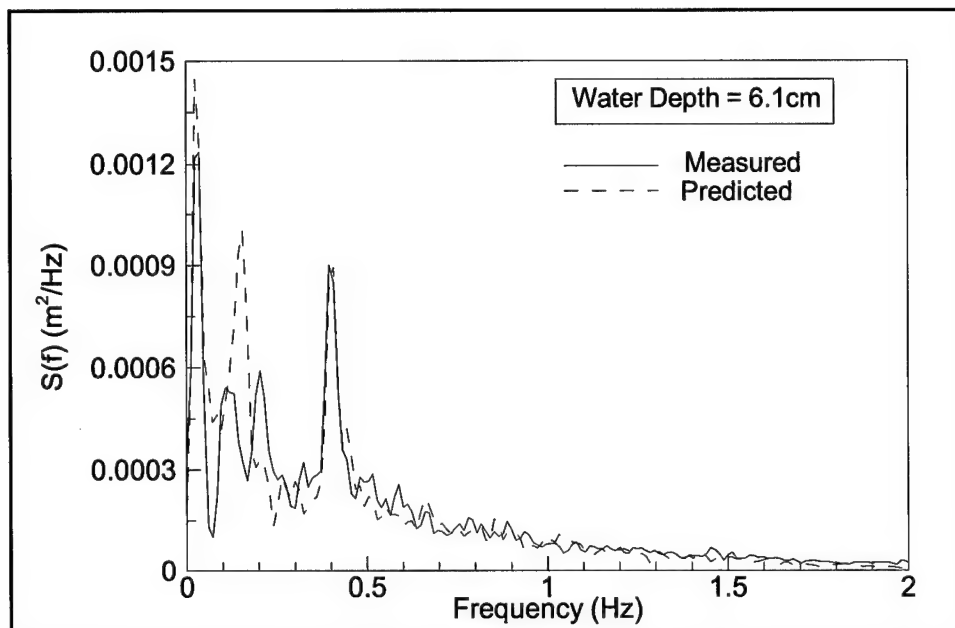
Figure 22. Measured and predicted wave spectra at Gauge 9 for bimodal sea state shoaling on a constant slope beach

Rip Currents on Barred Beaches

Rip currents are narrow, jet-like currents that flow out from the surf zone towards the open ocean. Rip currents are typically generated when there are alongshore variations in the wave breaking location. Alongshore variations could be associated with bathymetric effects (e.g., gaps in sandbars), the presence of structures (piers, jetties, etc.) or edge waves, generated by the trapping of reflected waves near the shoreline. One characteristic feature of rip currents is their unsteady nature. The currents tend to occur episodically as well as oscillate in the horizontal plane (Smith and Largier 1995).

Haller, Dalrymple, and Svendsen (1997) carried out laboratory experiments to investigate the generation of rip currents on a barred beach with rip channels. The bathymetry consists of a 1:30 constant slope beach with a superimposed longshore bar. The bar has two 1.8-m-wide gaps as shown in Figure 23. The water depth is 40 cm at the seaward boundary and 5 cm at the top of the bar. The Boussinesq model was applied to a regular wave test case with height $H = 4.5$ cm, and period $T = 1$ s. Numerical simulations were carried out using grid spacings $\Delta x = \Delta y = 0.06$ m and time-step size $\Delta t = 0.015$ s.

Figure 24 shows a snapshot of the instantaneous water-surface elevation 70 s into the simulation. Waves propagating over the bar break on the bar while those propagating through the gap break closer to the shoreline. This sets up a spatial variation of the mean water level and drives a time-varying circulation pattern. Figure 25 shows a 2-D map of the mean currents averaged over 50 wave cycles (from $t = 150$ s to $t = 200$ s). As observed in the laboratory experiments, there are two pairs of counterrotating circulation cells. The primary circulation consists of
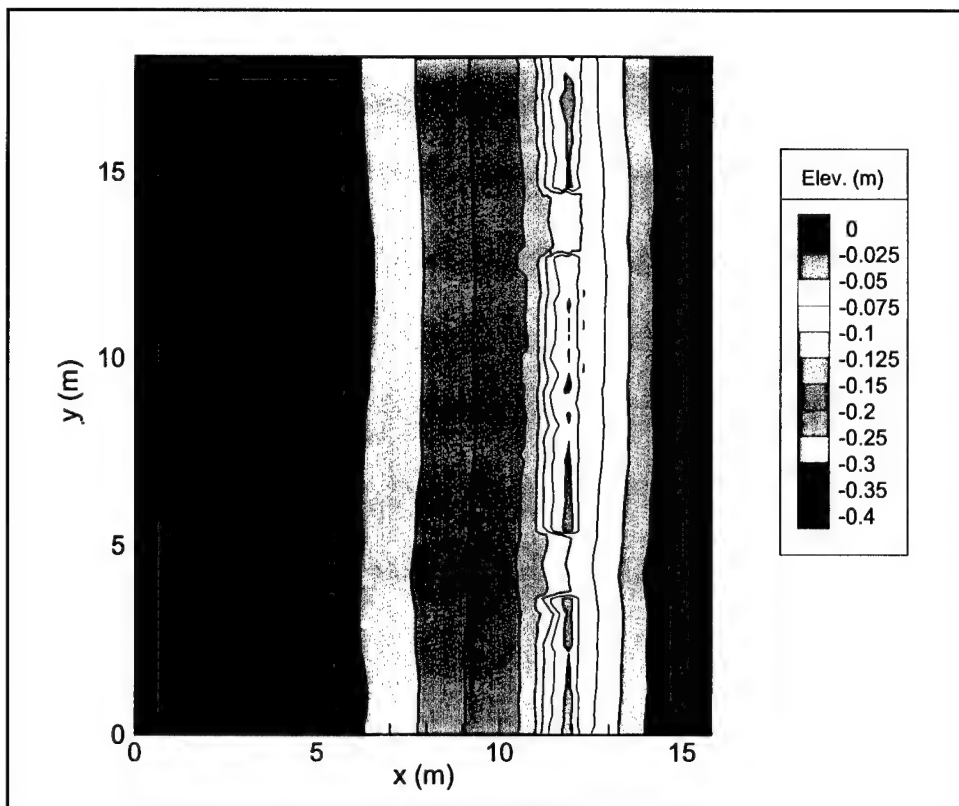
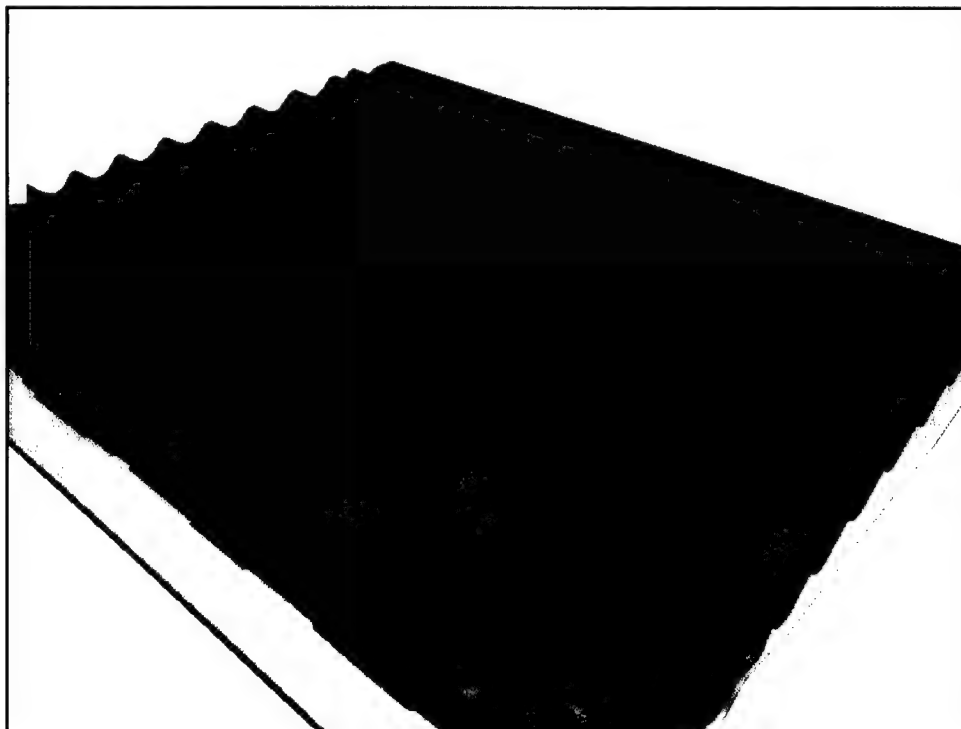Figure 23. Plan view of bathymetry for rip current experiments

Figure 24. 3-D view of wave propagation over a barred beach with a rip channel
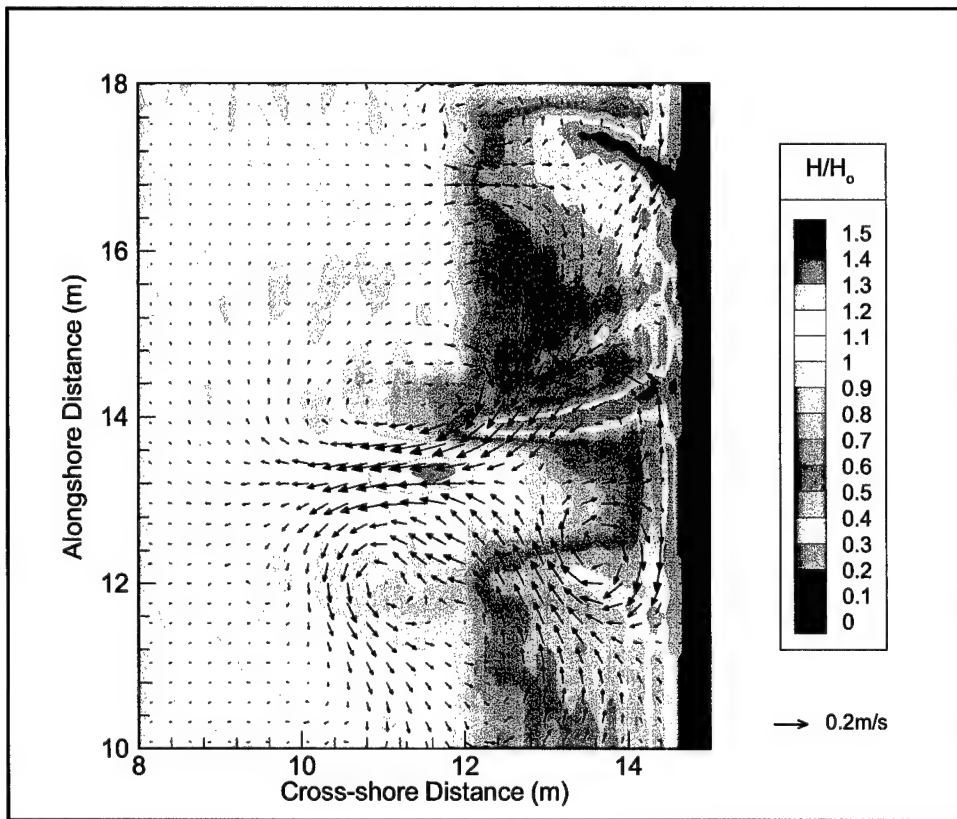(H = 5 cm, T = 1 s)

Figure 25. Time-averaged rip current pattern at t = 200 s

opposing longshore currents that converge and flow seawards through the gap in the sandbar. The secondary circulation cell occurs closer to the shoreline.

Wave-Current Interaction

The presence of currents can significantly modify the wave field inside entrance channels and harbors. This is particularly true for adverse currents where the interaction shortens and steepens the waves, leading to potentially hazardous navigation conditions. Smith et al. (1998) carried out laboratory experiments to investigate wave-current interaction in an idealized inlet. The bathymetry and layout used for the numerical simulations is shown in Figure 26. The wave basin is 24 m wide and 18.25 m long. The water depth variation adjacent to the inlet is given by the equilibrium beach profile:

$$h = 0.036y^{0.67} + 0.022 \qquad (66)$$

The equilibrium profile extends to a water depth of 0.205 m beyond which it is linearly transitioned at a slope of 1:7 to the constant depth region of 0.325 m. The entrance channel is lined by two parallel jetties that extend a distance of 3.8 m from the shoreline ($y = 0$) with an entrance width of 4 m.
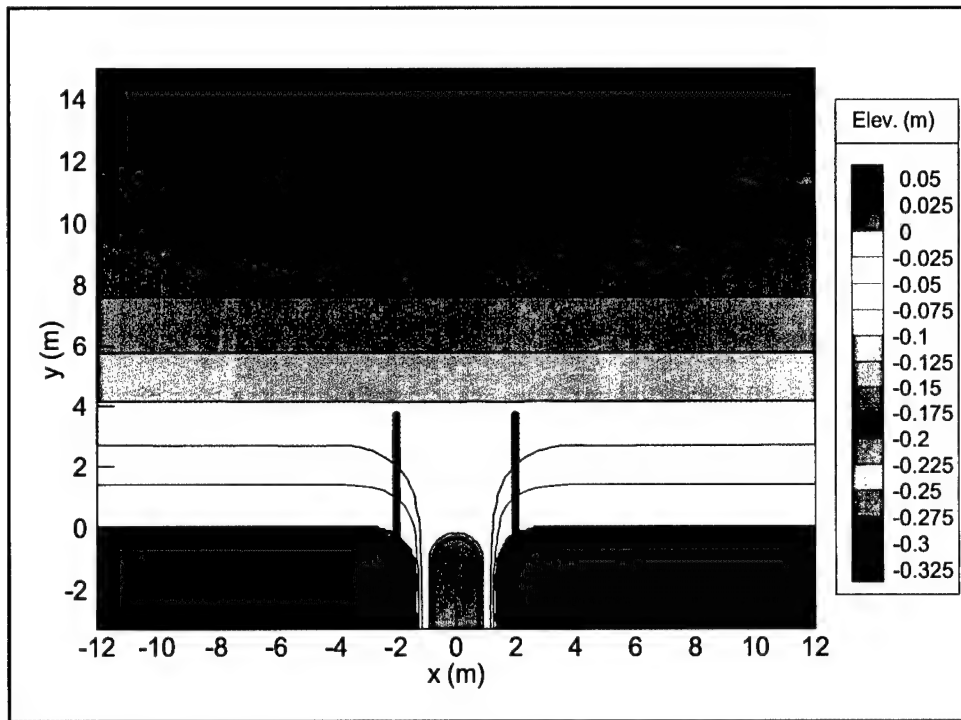
Figure 26. Bathymetry of idealized inlet for wave-current interaction study

A 2-D hydrodynamic model was run to provide the current field for use in the wave model simulations. Figure 27 shows a map of the current field generated by the model. Boussinesq model simulations were carried out using grid spacings $\Delta x = \Delta y = 0.075$ m and time-step size $\Delta t = 0.015$ s. The incident wave conditions were characterized by a TMA spectrum with $H_{mo} = 0.055$ m, $T_p = 1.4$ s, and $\gamma = 3.3$. The predicted wave height distributions for current speeds $U = 0$ m/s and $U = 0.24$ m/s are shown in Figures 28 and 29, respectively. The Boussinesq model predicted an increase of 15 to 20 percent in the significant wave height near the entrance channel. The laboratory measurements, however, showed a slight decrease in wave height through the channel due to the effect of wave breaking. A more detailed investigation of the wave-breaking criterion and energy dissipation rates in the presence of currents will be carried out to improve simulations of wave-current interaction in the Boussinesq model.

Wave Transformation Near Ponce de Leon Inlet, Florida

Ponce de Leon Inlet, an inlet leading into the Halifax and Indian Rivers in Florida has a complex bathymetry featuring a large ebb shoal, a navigation channel, and a jetty. A 1:100 laboratory model study of a 4.2-km by 1.4-km region near the inlet was carried out at the U.S. Army Engineer Research and Development Center (ERDC) Coastal and Hydraulics Laboratory (CHL). Tests were conducted for sea states with different wave heights, peak periods, spectral widths, and directional spread. The TMA spectrum was used to describe the frequency distribution of wave energy, while the wrapped-normal distribution
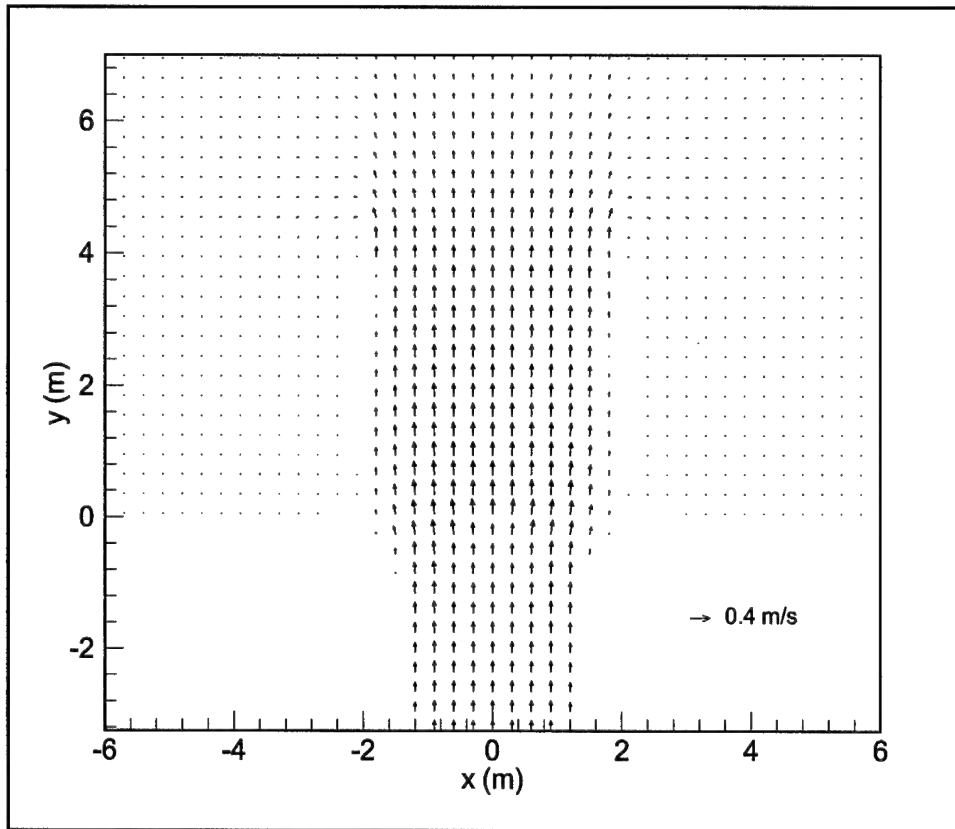
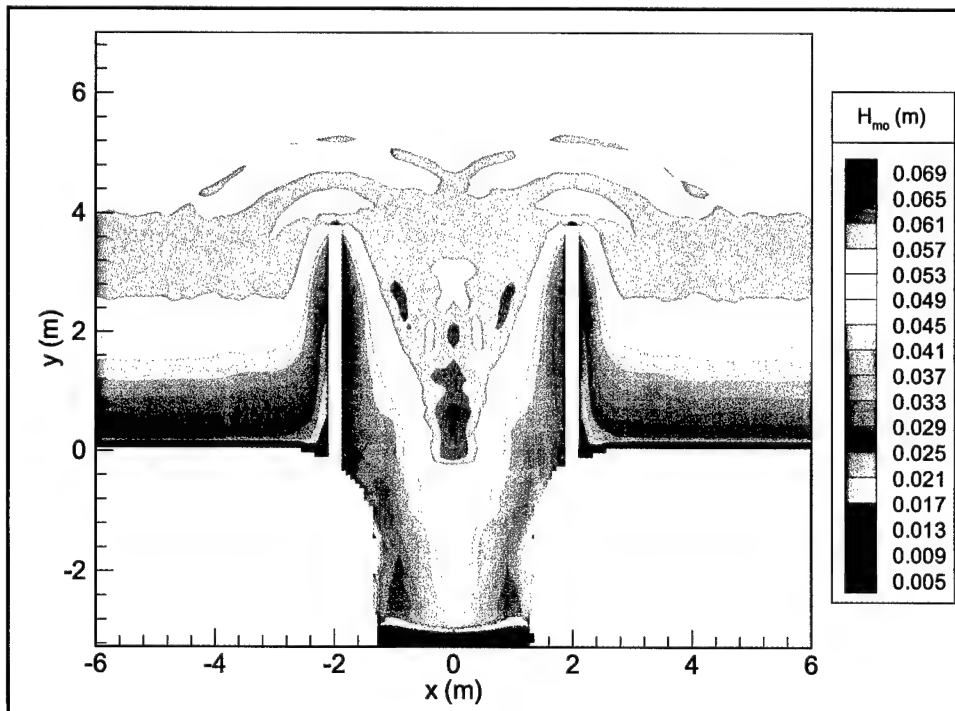Figure 27. Predicted current field for $U = 0.24$ m/s

Figure 28. Predicted wave height distribution near inlet for test case without
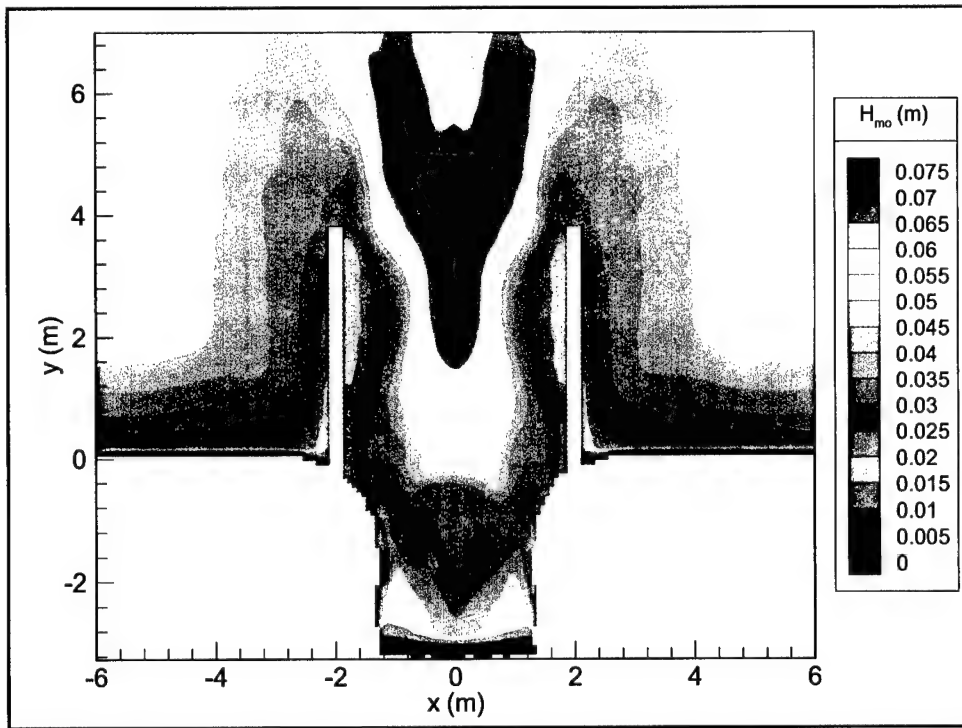currents ($H_{mo} = 0.055$ m, $T_p = 1.4$ s, $U = 0$ m/s)

Figure 29. Predicted wave height distribution near inlet for test case with currents (H_{mo} = 0.055m, T_p = 1.4 s, U = 0.24 m/s)

was used for the directional spreading function. Water-surface elevation data were recorded at 30 locations.

BOUSS-2D was run for one of the multidirectional test cases characterized by H_{mo} = 0.95 m, T_p = 10 s, γ = 5, and directional spread σ_θ = 20 deg (Test No. 11). The bathymetry used for the numerical simulations is shown in Figure 30. Boussinesq model simulations were carried out using $\Delta x = \Delta y = 5$ m and $\Delta t = 0.15$ s. Time-histories of the velocity boundary conditions along the wavemaker were synthesized using the double-summation method for a duration of 500 s, corresponding to 50 wave periods.

A snapshot of the instantaneous water-surface elevation produced by the BOUSS-2D model is shown in Figure 31. The corresponding significant wave height distribution is shown in Figure 32. Two distinct wave-focusing regions can be observed on the shoal. The predicted wave height variations along the offshore and nearshore gauge arrays are compared to the experimental results in Figures 33 and 34, respectively. BOUSS-2D reasonably reproduced the wave height variation along the offshore array, although differences of the order of 20 percent exist at a couple of gauge locations. For the nearshore array, excellent agreement is obtained between BOUSS-2D model predictions and the experimental data.
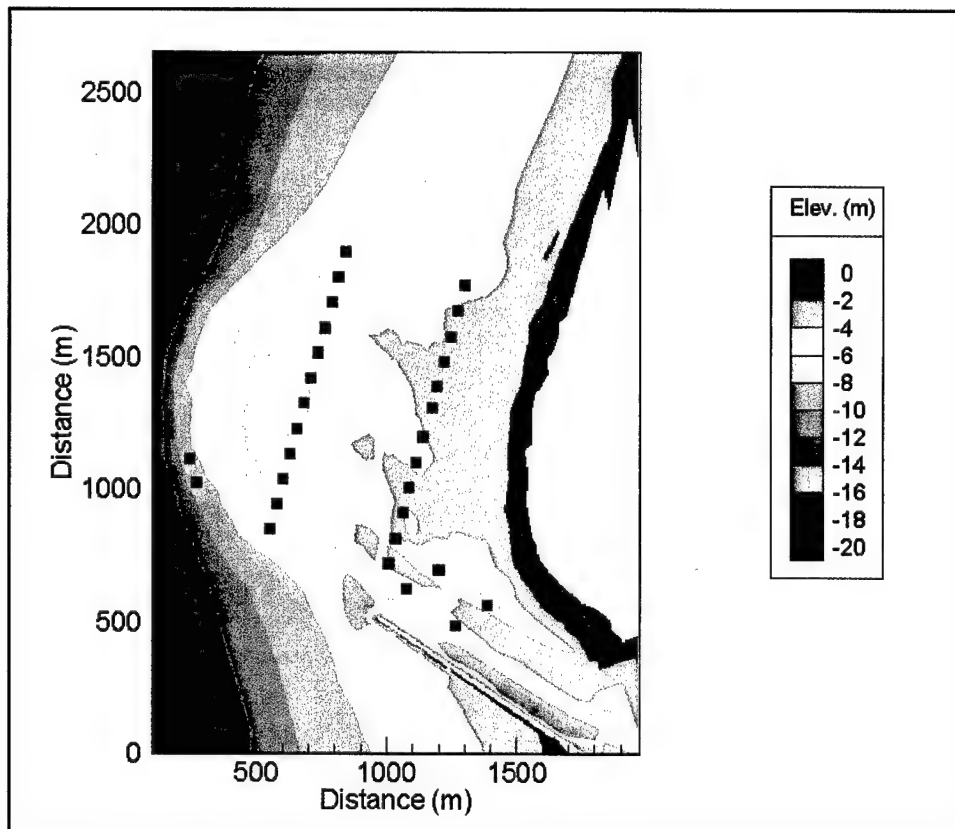
Figure 30. Ponce de Leon Inlet model bathymetry
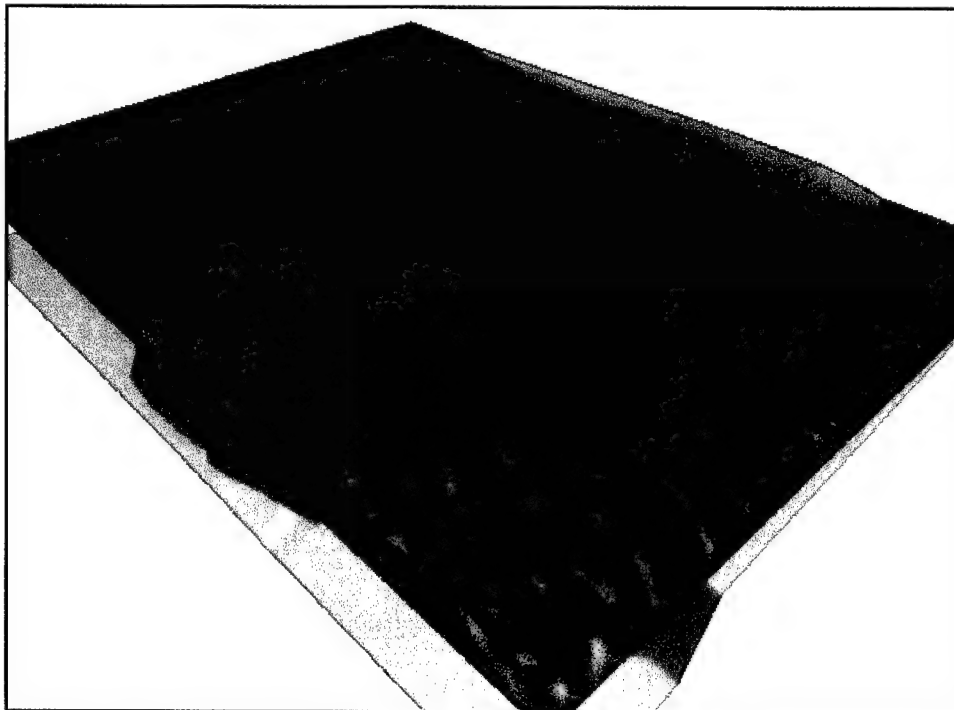
Figure 31. 3-D view of multidirectional wave propagation near Ponce de Leon Inlet (H_{mo} = 0.95 m, T_p = 10 s, σ_θ = 20 deg)
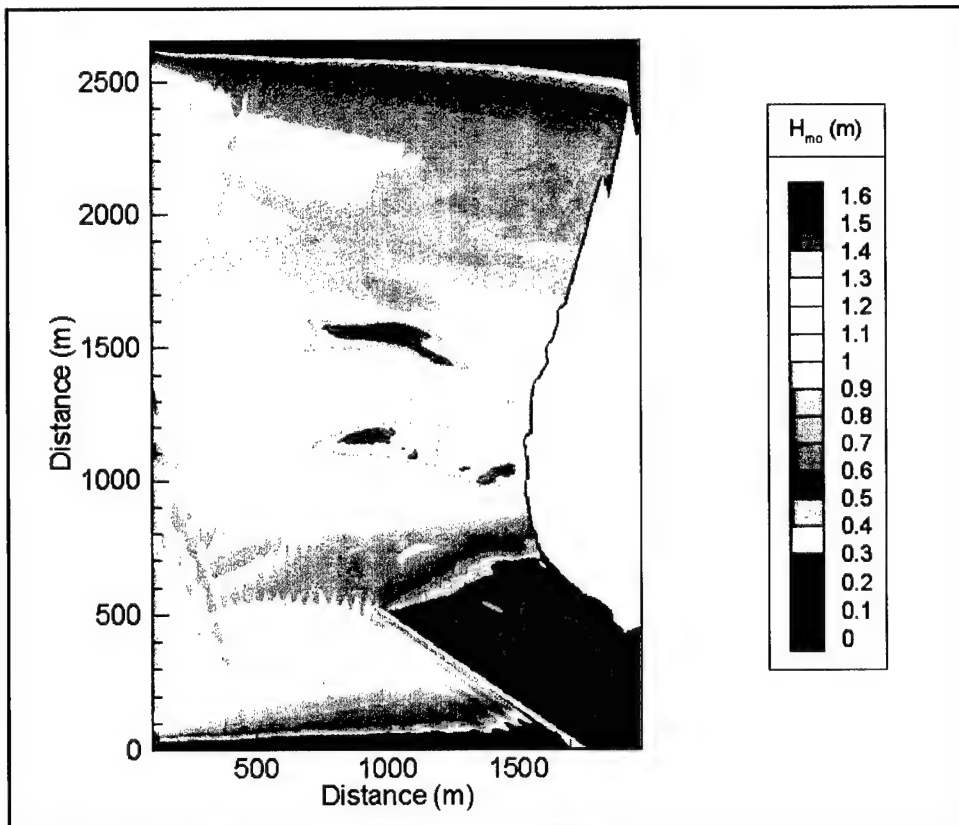
Figure 32. 2-D map of wave height distribution predicted by Boussinesq model (H_{mo} = 0.95 m, T_p = 10 s, σ_θ = 20 deg)
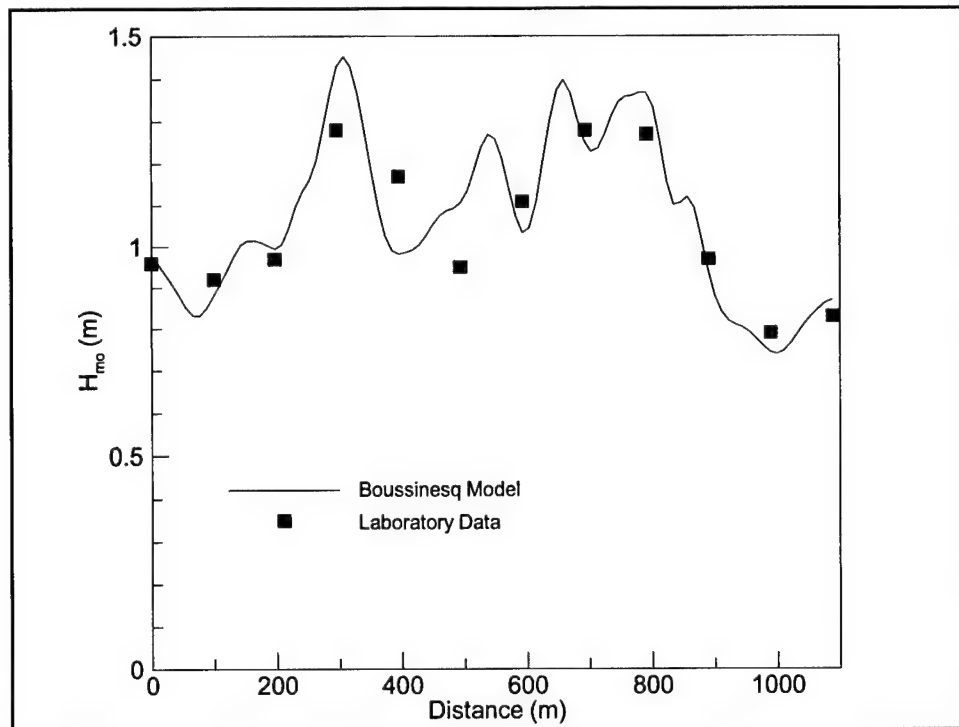
Figure 33. Measured and predicted wave height distribution along the offshore gauge array (H_{mo} = 0.95 m, T_p = 10 s, σ_θ = 20 deg)
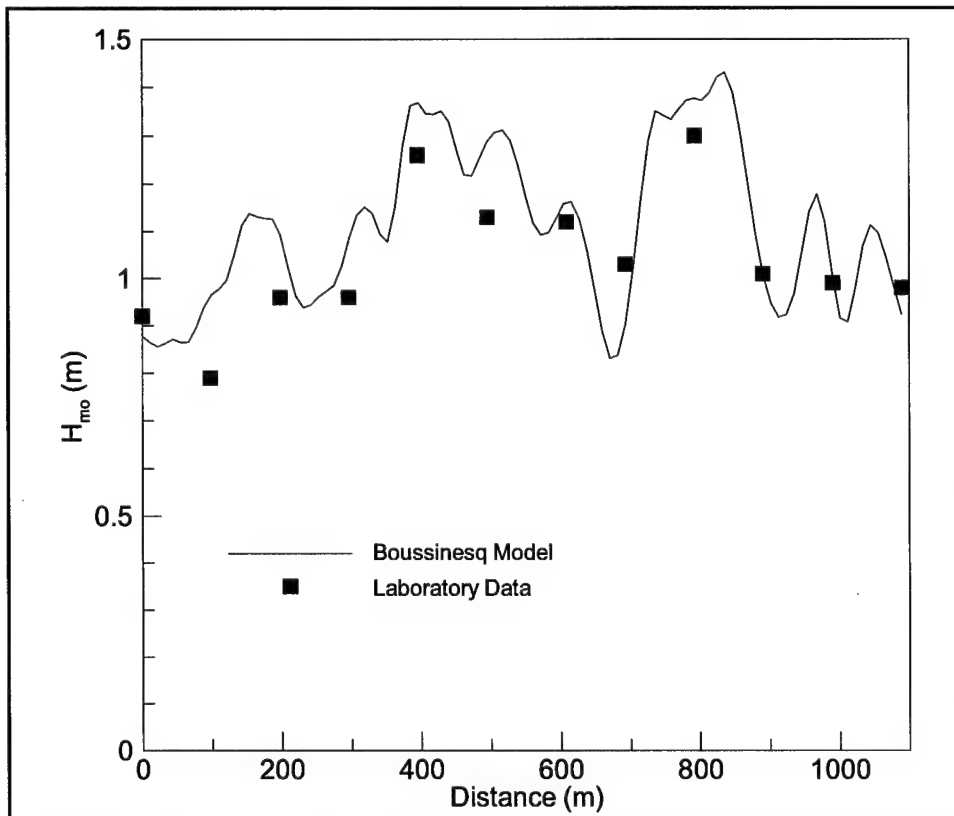
Figure 34. Measured and predicted wave height distribution along the nearshore
gauge array (H_{mo} = 0.95 m, T_p = 10 s, σ_θ = 20 deg)

Wave Disturbance in Barbers Point Harbor, Hawaii

Barbers Point Harbor is a small harbor in Hawaii that has experienced occasional long-period harbor oscillation problems. The main harbor basin is 11.6 m deep, and is connected to the Pacific Ocean through a 12.8-m-deep, 1.3-km-long entrance channel. The water depths are shallow (2 to 10 m) in the vicinity of the entrance channel, leading to the nonlinear generation of free and forced long-period waves near the harbor entrance. Free long waves could be resonantly amplified inside the harbor basin if the long-wave periods are close to any of the natural modes of oscillation of the basin.

BOUSS-2D was used to investigate to the resonant harbor oscillation periods and the wave height amplification factors. A three-dimensional view of the bathymetry and harbor layout used for the simulations is shown in Figure 35. The offshore boundary was truncated at a water depth of 50 m. Numerical simulations were carried for regular waves with periods ranging from 50 s to 200 s. Wave height information was output at two gauges outside the harbor and four gauges inside the harbor as shown in Figure 36.

Figure 35. 3-D view of Barbers Point Harbor model bathymetry

Figure 36. 2-D map of Barbers Point Harbor bathymetry showing wave gauge
locations

The predicted wave heights at two gauge locations inside the basin, normalized by the incident wave height, are compared with predictions from the elliptic mild-slope model CGWAVE (Demirbilek and Panchang 1998) in Figures 37 and 38. The harbor exhibits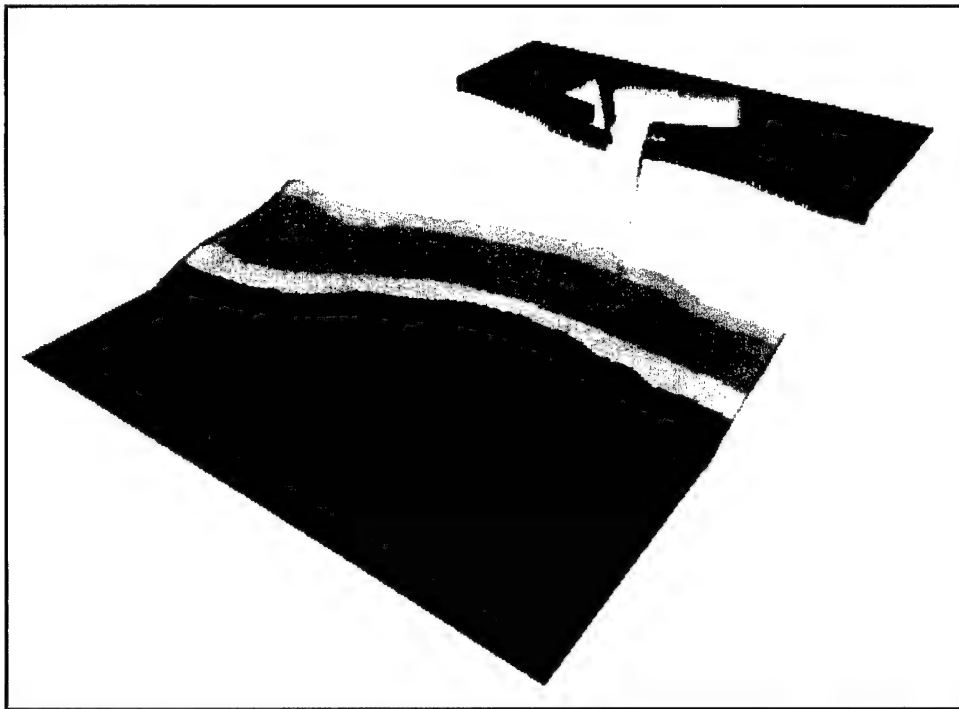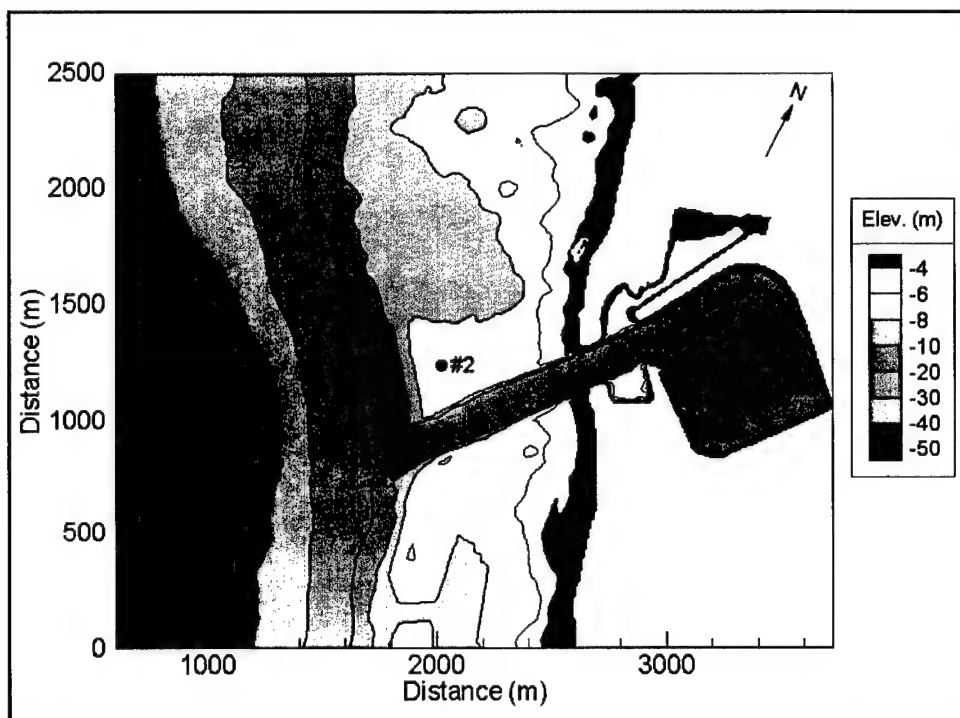 a number of distinct periods of oscillation (60 s, 83 s, 110 s, 130 s, 143 s, and 190 s). The Helmholtz or pumping mode of the basin occurs at a period of around 900 s. Good agreement is generally observed between wave height amplification factors predicted by both models. It should be pointed out that it takes longer to attain steady-state conditions in time-domain models, especially for resonant oscillations. Figure 39 shows a plot of the time history at Gauge 5 for one of the resonance periods ($T = 60$ s). Steady-state conditions are attained approximately 30 wave periods after the waves initially arrived at the gauge location.

Although linear, frequency-domain models are computationally more efficient at predicting harbor resonance periods and amplification factors, they cannot predict the magnitude of the long-period wave energy inside a harbor from a given offshore wind-wave spectrum. To overcome this deficiency, Okihiro, Guza, and Seymour (1993) used an ad-hoc coupling of a nonlinear model for the generation of bound long waves outside a harbor with a linear model for the amplification of long waves inside the harbor. The complex nature of bathymetry outside Barbers Point Harbor makes it difficult to quantify the relative amount of long-wave energy outside the harbor that is freely propagating into the harbor. The entrance channel is much deeper than the surrounding areas. Free long waves would be generated along the steep side slopes of the entrance channel as well as reflected from shoreline. The long waves would thus be propagating over a wide range of directions.

We investigated the ability of the Boussinesq model to simultaneously model the nonlinear generation of long waves by storm waves propagating from deep to shallow water, the diffraction of both short and long period waves into the harbor basin, and the resonant amplification of long waves inside a harbor. We initially considered a bichromatic wave train with component periods $T_1 = 12$ s, $T_2 = 13.46$ s, and heights $H_1 = H_2 = 1.5$ m. The group period of 110 s corresponds to one of the natural periods of oscillation of the basin. Numerical simulations were carried out with $\Delta x = \Delta y = 10$ m and $\Delta t = 0.2$ s. The simulated surface elevation time-histories at the offshore Gauge 1, harbor entrance Gauge 2, and harbor basin Gauges 3 and 5 are shown in Figure 40. The long-period component, obtained by applying a low-pass filter ($T > 25$ s), is also shown in the figures. It can be seen that nonlinear interactions during the shoaling process lead to an amplification of the long-period wave component between the offshore Gauge 1 which is in 50 m of water, and the harbor entrance Gauge 2 which is 7 m of water. Inside the harbor basin, the long waves are further amplified and dominate the harbor response at Gauge 5.

Although bichromatic waves are useful for demonstrating the importance of nonlinear wave-wave interactions in harbor response, natural sea states are irregular with wave energy distributed over a large number of frequency components. We simulated the response of the harbor to an irregular wave train. Numerical simulations were carried out for an incident sea state characterized by a JONSWAP spectrum with $H_{mo} = 3$ m, $T_p = 12$ s and $\gamma = 3.3$. Figure 41 shows a
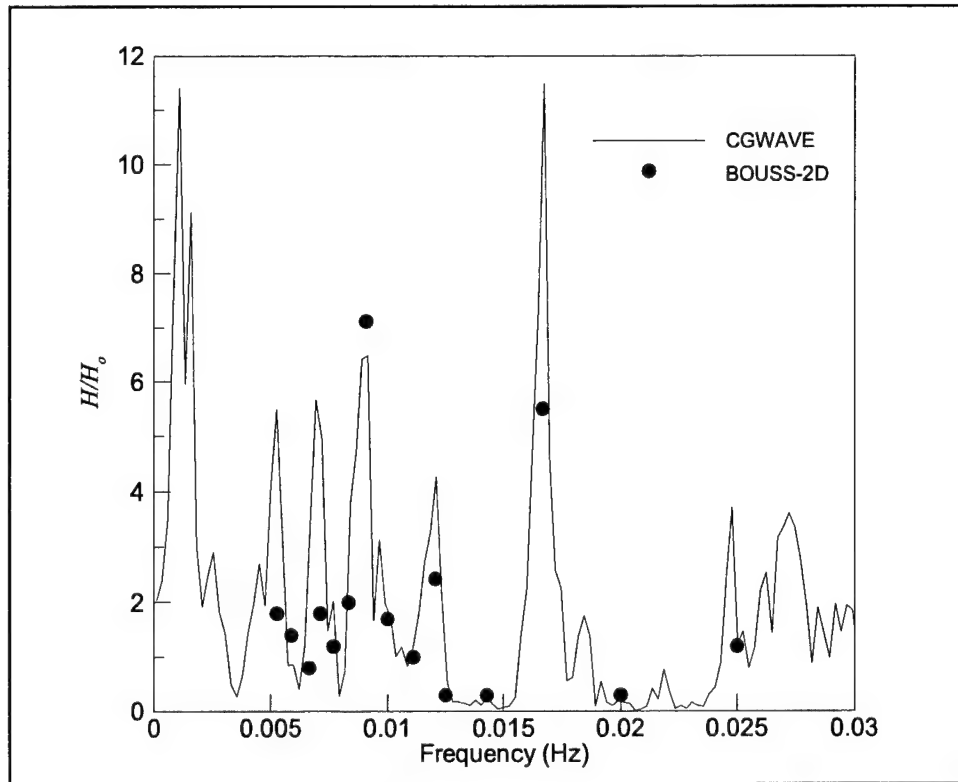
Figure 37. CGWAVE and BOUSS-2D model predictions of the wave height amplification factor at Gauge 5
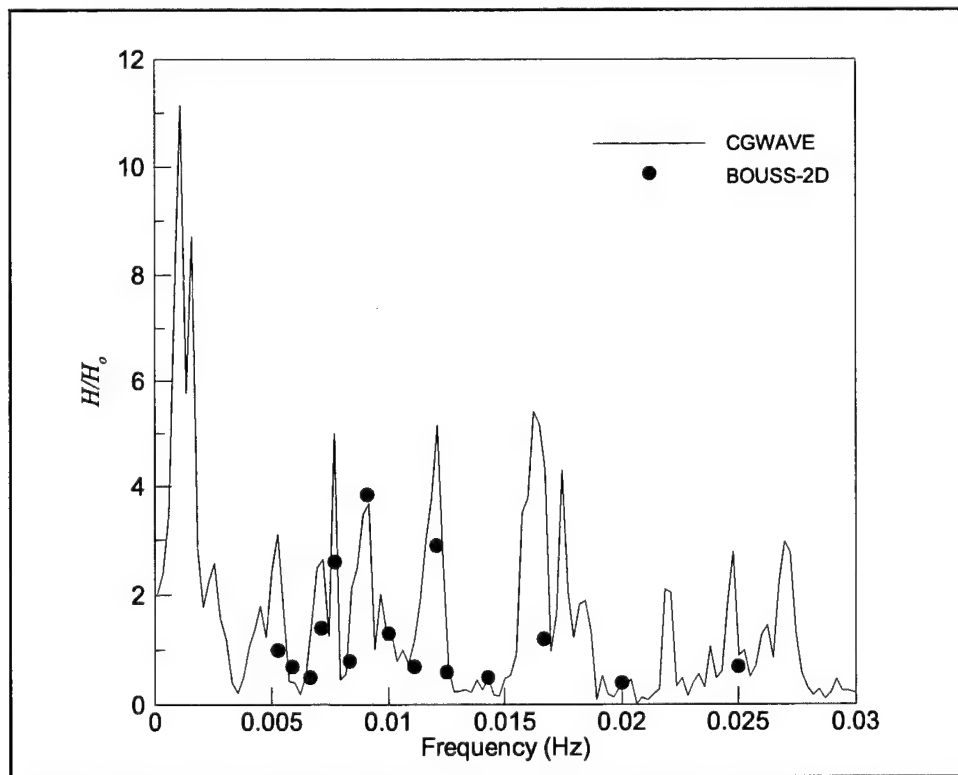
Figure 38. CGWAVE and BOUSS-2D model predictions of the wave height amplification factor at Gauge 6
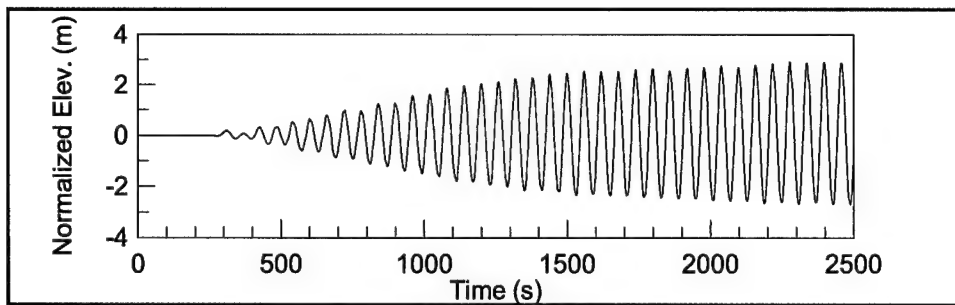
Figure 39. Boussinesq model prediction of the time-history of the water-surface elevation at Gauge 5 for a natural harbor period (T = 60 s)
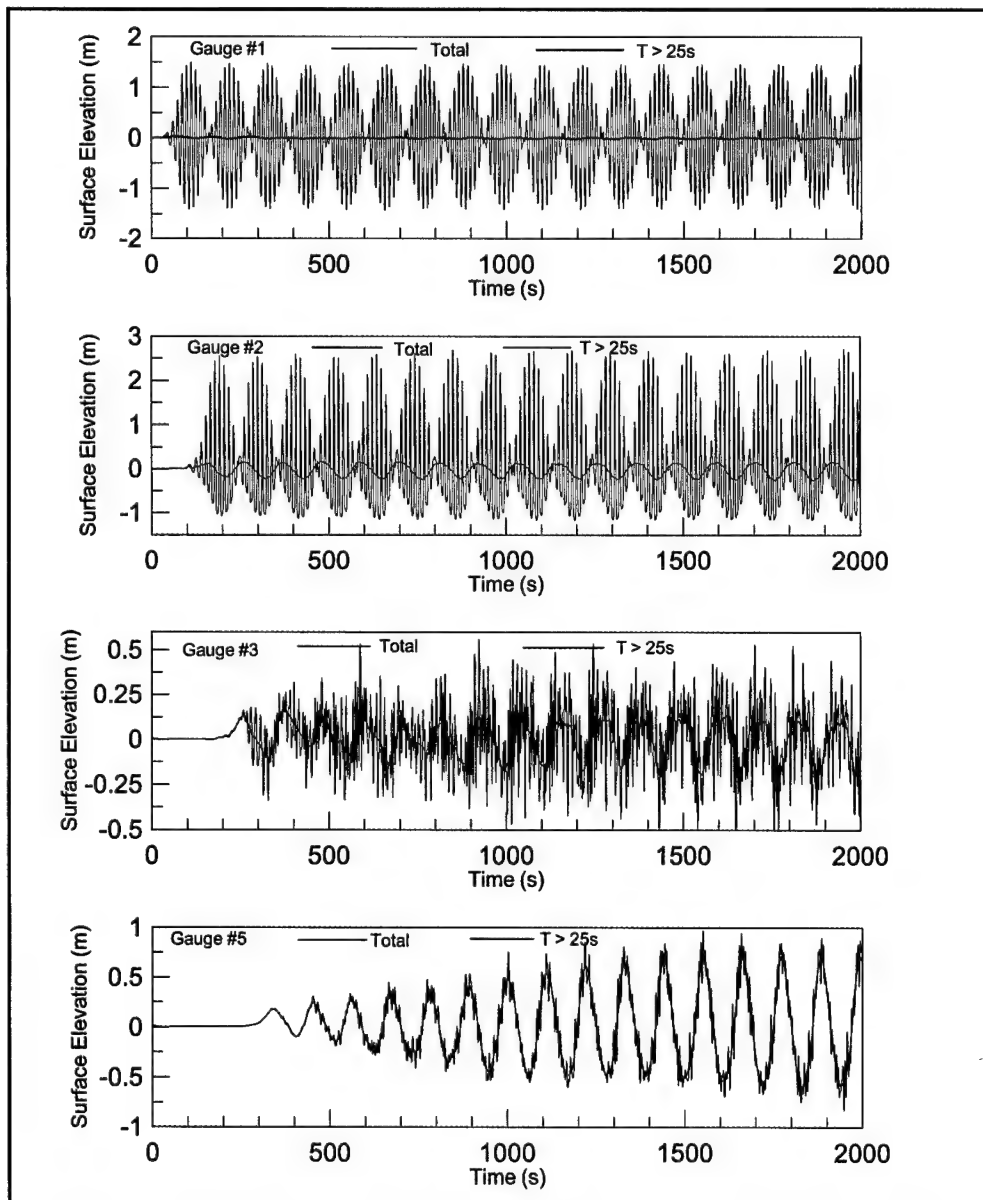
Figure 40. Time-histories of total and long-period (T > 25 s) component of water-surface elevation at Gauges 1, 2, 3, and 5 for bichromatic wave train
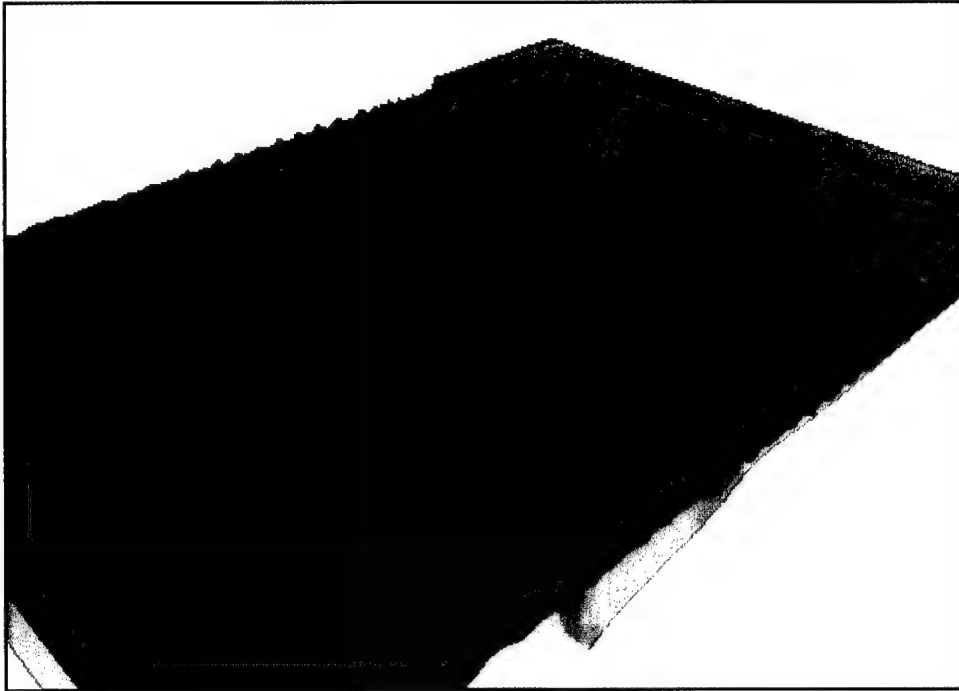
Figure 41. 3-D view of irregular wave propagation into Barbers Point Harbor

snapshot of waves propagating into the harbor. The predicted wave spectra at Gauges 1 and 2 are shown in Figure 42. It can be seen that nonlinear interactions significantly modified the wave spectrum at Gauge 2 ($h = 7$ m), with the cross-spectral transfer of energy to both lower and higher harmonics. The wave spectra for the four gauges located inside the harbor basin are plotted in Figure 43. The short-period wave energy is much smaller inside the harbor basin because the bathymetry acts to refract waves away from the harbor entrance.

The wave spectra were divided into short-period ($T < 25$ s) and long-period components ($T > 25$ s) and wave heights were calculated for each component. The short-period wave heights at the inside gauges varied from 0.42 to 0.57 m, compared to 3.1 m at outside Gauge 2. The long-wave energy inside the harbor is, however, comparable to that at the outside gauge with heights ranging from 0.38 to 0.46 m for the inside gauges, compared to 0.49 m at an outside Gauge 2.
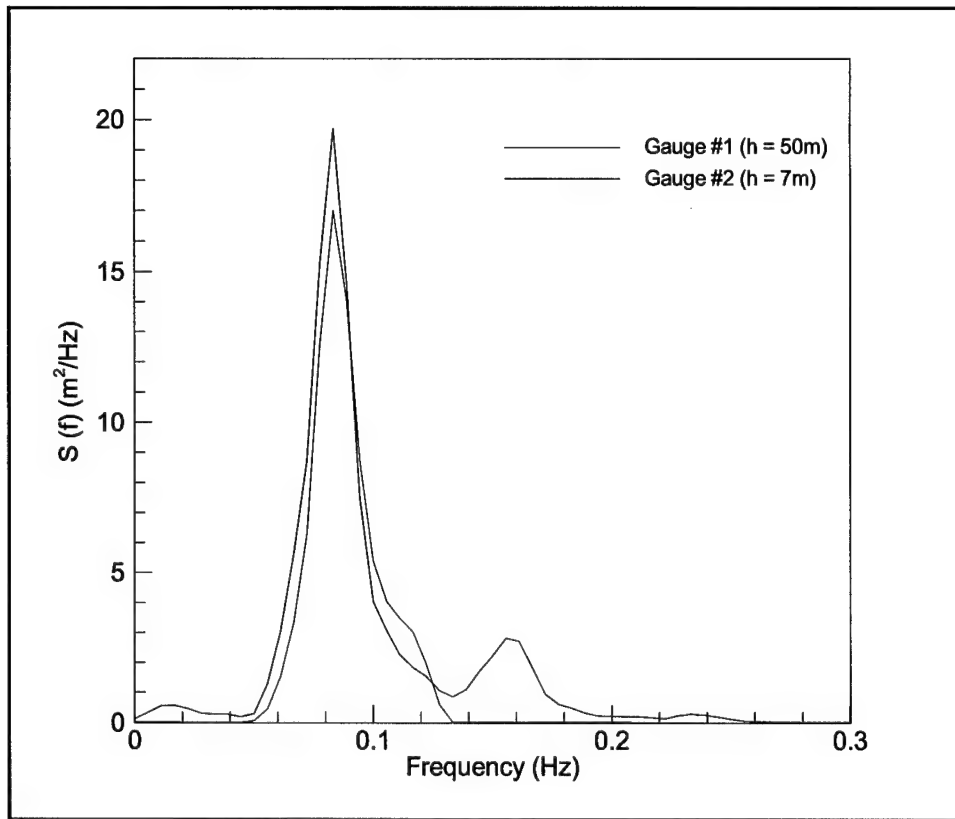
Figure 42. Predicted wave spectra at the outside Gauges 1 and 2 for an irregular sea state (H_{mo} = 3 m, T_p = 12 s)
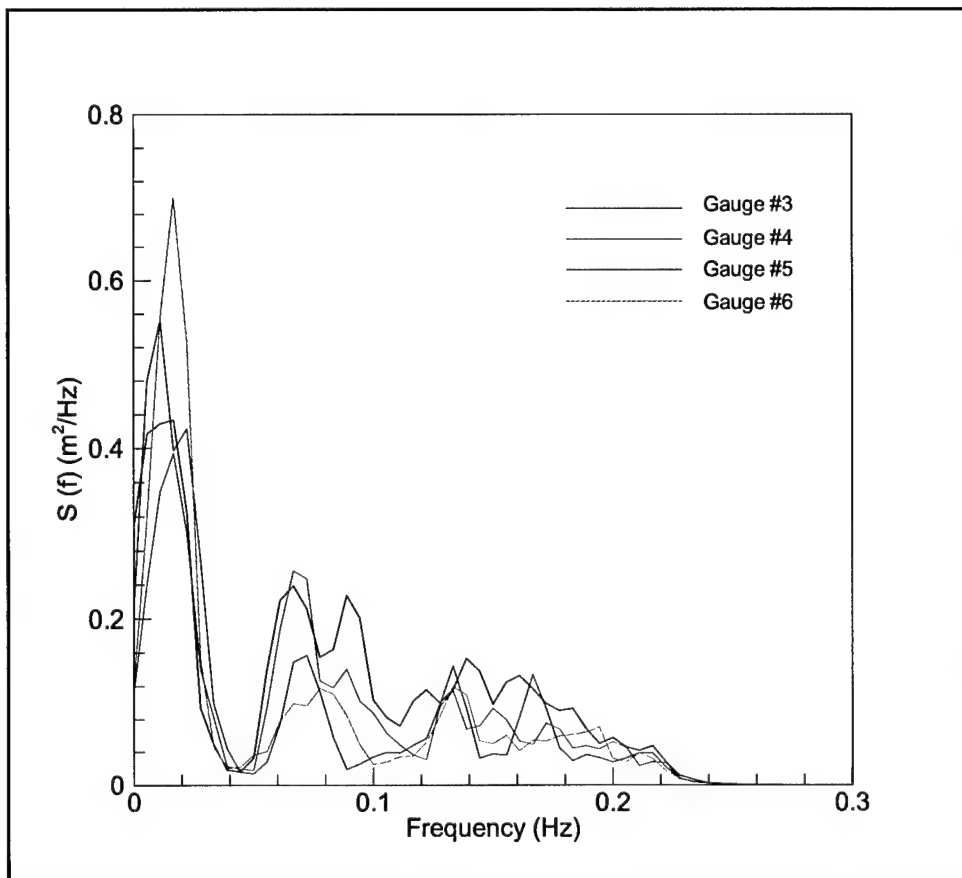
Figure 43. Predicted wave spectra at gauges inside harbor basin (Gauges 3-6)
for an irregular sea state (H_{mo} = 3 m, T_p = 12 s)

References

Borgman, L. E. (1969). "Directional spectra models for design use," *Proceedings*, 1st Annual Offshore Technology Conference, Houston, Paper No. OTC 1069, 721-746.

Borgman, L. E. (1972). "Statistical models for ocean waves and wave forces," *Advances in Hydroscience* 8, 139-181.

Bradford, S. F. (2000). "Numerical simulation of surf zone dynamics," *Journal of Waterway, Port, Coastal and Ocean Engineering*, ASCE, 126(1), 1-13.

Bouws, E., Gunther, H., and Vincent, C. L. (1985). "Similarity of the wind wave spectrum in finite depth water, Part I, Spectral form," *Journal of Geophysical Research* 90, 975-986.

Bretschneider, C. L. (1959). "Wave variability and wave spectra for wind-generated gravity waves," Technical Memo No. 118, Beach Erosion Board, U.S. Army Corps of Engineers.

Dean, R. G., and Sharma, J. N. (1981). "Simulation of wave systems due to nonlinear directional spectra," *Proceedings*, International Symposium on Hydrodynamics in Ocean Engineering, Trondheim, Norway, 1211-1222.

Demirbilek, Z., and Panchang, V. (1998). "CGWAVE: A coastal surface water wave model of the mild slope equation," Technical Report CHL-98-26, U.S. Army Engineer Waterways Experiment Station, Vicksburg, MS.

Engelund, F. (1953). "On the laminar and turbulent flow of ground water through homogeneous sand," *Trans. Danish Academy of Technical Sciences* 3(4).

Gordkin, C. B., and Pulli, J. J. (1984). "Application of the winding-number algorithm to the spatial sorting of catalogued earthquake data," *Bulletin of the Seismological Society of America* 74(5), 1845-1848.

Haller, M. C., Dalrymple, R. A., and Svendsen, I. A. (1997). "Rip channels and nearshore circulation," *Proceedings*, Coastal Dynamics '97, Plymouth, U.K., 594-603.

Hasselmann, K., Barnett, T. P., Bouws, E., Carlson, H., Cartwright, D. E., Enke, K., Ewing, J. A., Gienapp, H., Hasselmann, D. E., Kruseman, P., Meerburg, A., Muller, P., Olbers, D. J., Richter, K., Sell, W., and Walden, H. (1973). "Measurements of wind-wave growth and swell decay during the joint North Sea wave project," *Deut. Hydrogr. Z.* Suppl. A 8(12), 1-95.

Hughes, S. A. (1993). *Physical models and laboratory techniques in coastal engineering.* World Scientific, Singapore.

Isaacson, M., and Qu, S. (1990). "Waves in a harbor with partially reflecting boundaries," *Coastal Engineering* 14, 193-214.

Jeffreys, E. R. (1987). "Directional seas should be ergodic," *Applied Ocean Reserach* 9(4), 186-191.

Kennedy, A. B., Chen, Q., Kirby, J. T., and Dalrymple, R. A. (2000). "Boussinesq modeling of wave transformation, breaking and runup, I: 1D," *Journal of Waterway, Port, Coastal and Ocean Engineering* 126(1), 37-39.

Kirby, J. T., and Ozkan, H. T. (1994). "Combined refraction/diffraction model for spectral wave conditions: REF/DIF-S," Center of Applied Coastal Research Report No. CACR-94-04. University of Delaware.

Kitaigorodskii, S. A., Krasitskii, V. P., and Zaslavskii, M. M. (1975). "On Phillips theory of equilibrium range in the spectra of wind-generated gravity waves," *Journal of Physical Oceanography* 5, 410-420.

Larsen, J. and Dancy, H. (1983). "Open wave boundaries in short wave simulations – A new approach," *Coastal Engineering* 7, 285-297.

Lin, P., and Liu, P. L. -F. (1998). "A numerical study of breaking waves in the surf zone," *Journal of Fluid Mechanics* 359, 239–264.

Mardia, K. V. (1972). *Statistics of directional data.* Academic Press, New York.

Miles, M. D. (1989). "A note on directional random wave synthesis by the single-summation method," *Proceedings*, XXIII IAHR Congress, Ottawa, Canada, C243-C250.

Nwogu, O., Mansard, E. P. D., Miles, M., and Isaacson, M. (1987). "Estimation of directional wave spectra by the maximum entropy method," *Proceedings, IAHR Seminar on Wave Analysis and Generation in Laboratory Basins,* XXII IAHR Congress, Lausanne, Switzerland, 363-376.

Nwogu, O. (1989). "Maximum entropy estimation of directional wave spectra from an array of wave probes," *Applied Ocean Research* 11(4), 176-182.

_____. (1993) "Alternative form of Boussinesq equations for nearshore wave propagation," *Journal of Waterway, Port, Coastal and Ocean Engineering*, ASCE, 119(6), 618-638.

Nwogu, O. (1994). "Nonlinear evolution of directional wave spectra in shallow water," *Proceedings,* 24th International Conference on Coastal Engineering, Kobe, Japan, 467-481.

_____. (1996). "Numerical prediction of breaking waves and currents with a Boussinesq model," Paper presented at the 25th International Conference on Coastal Engineering, ICCE '96, Orlando, FL.

Ochi, M. K., and Hubble, E. N. (1976). "Six-parameter wave spectra," *Proceedings,* 15th Int. Conference on Coastal Engineering, Honolulu, 301-328.

Okihiro, M., Guza, R. T., and Seymour, R. J. (1993). "Excitation of seiche observed in a small harbor," *Journal of Geophysical Research* 98(C10), 18201-18211.

Osborne, A. R. (1997). "Approximate asymptotic integration of a higher order water-wave equation using the inverse scattering transform," *Nonlinear Processes in Geophysics* 4, 29-53.

Peregrine, D. H. (1967). "Long waves on a beach," *Journal of Fluid Mechanics* 27, 815-827.

Pierson, W. J., and Moskowitz, L. (1964). "A proposed spectral form for fully developed wind seas based on the similarity theory of S. A. Kitaigorodskii," *Journal of Geophysical Research* 69, 5181-5190.

Rienecker, M. M., and Fenton, J. D. (1981). "A Fourier approximation method for steady water waves," *Journal of Fluid Mechanics* 104, 119-137.

Sand. S. E., and Mynett, A. E. (1987). "Directional wave generation and analysis," *Proceedings*, IAHR Seminar on Wave Generation and Analysis in Laboratory Basins, XXII IAHR Congress, Lausanne, Switzerland, 209-235.

Smagorinsky, J. (1963). "General circulation experiments with the primitive equations," *Monthly Weather Review* 91, 91-164.

Smith, J. A., and Largier, J. L. (1995). "Observations of nearshore circulation: Rip currents," *Journal of Geophysical Research* 100, 10967-10975.

Smith, J. M., Seabergh, W. C., Harkins, G. S., and Briggs, M. J. (1998). "Wave breaking at an idealized inlet," Technical Report CHL-98-31, U.S. Army Engineer Waterways Experiment Station, Vicksburg, MS.

Smith, J. M., Sherlock, A. R., and Resio, D. T. (2001). "STWAVE: Steady-state spectral wave model user's manual, Version 3.0." Special Report SR-01-1, U.S. Army Engineer Research and Development Center, Vicksburg, MS.

Smith, J. M., and Vincent, C. L. (1992). "Shoaling and decay of two wave trains on beach," *Journal of Waterway, Port, Coastal and Ocean Engineering* 118(5), 517-533.

St. Denis, M., and Pierson, W. J. (1953). "On the motions of ships in confused seas," *Trans. SNAME* 61, 280-357.

Stansberg, C. T. (1987). "Statistical properties of directional sea measurements," *Journal of Offshore Mechanics and Arctic Engineering* 109, 142-147.

Thompson, E. F. (1980). "Energy spectra in shallow U.S. coastal waters," Technical Paper No. 80-2, Coastal Engineering Research Center, U.S. Army Corps of Engineers, Fort Belvoir, VA.

Van Dongeren, A. R., and Svendsen, I. A. (1997). "Absorbing–generating boundary condition for shallow water models," *Journal of Waterway, Port, Coastal and Ocean Engineering*, ASCE, 123(6), 303–313.

Vincent, C. L,. and Briggs, M. J. (1989). "Refraction-diffraction of irregular waves over a mound," *Journal of Waterway, Port, Coastal and Ocean Engineering* 115(2), 269-284.

Wei, G., Kirby, J. T., Grilli, S. T., and Subramanya, R. (1995). "A fully nonlinear Boussinesq model for surface waves, Part 1, highly nonlinear unsteady waves," *Journal of Fluid Mechanics* 294, 71-92.

Witting, J. M. (1984). "A unified model for the evolution of nonlinear water waves," *Journal of Computational Physics* 56, 203-236.

Appendix A
Fourier Series Solutions of Boussinesq Equations

As the height of surface waves in intermediate and shallow-water depths increases, the wave profile changes from a sinusoidal shape to an asymmetric one with peaked crests and broad shallow troughs. The Boussinesq equations are nonlinear and are able to describe the change in wave shape, provided the wave height and period are within nonlinear and dispersive limits of the equations. However, it is important that the velocity and flux time-histories imposed along the wave generation boundaries of the numerical model be consistent with the equations that are solved within the computational domain. In BOUSS-2D, the Fourier approximation method of Rienecker and Fenton (1981)[1] has been used to derive nonlinear boundary conditions for periodic waves in water of constant depth. The one-dimensional form of the weakly nonlinear form of the Boussinesq equations (Equations 4 to 6) for water of constant depth can be written as:

$$\eta_t + [(h+\eta)u_\alpha]_x + \left(\alpha + \frac{1}{3}\right)h^3 u_{\alpha,xxx} = 0 \tag{A1}$$

$$u_{\alpha,t} + g\eta_x + \frac{1}{2}\left(u_\alpha^2\right)_x + \alpha h^2 u_{\alpha,xxt} = 0 \tag{A2}$$

For periodic waves, the partial differential equations can be transformed into a set of coupled nonlinear ordinary differential equations in terms of coordinate system, $\xi = x - Ct$, moving at the phase speed of the waves, C, and integrated once to yield:

$$(h+\eta)u_\alpha + \left(\alpha + \frac{1}{3}\right)h^3 u_{\alpha,\xi\xi} + Q = 0 \tag{A3}$$

$$g\eta + \frac{1}{2}\left(u_\alpha^2\right) + \alpha h^2 u_{\alpha,\xi\xi} - R = 0 \tag{A4}$$

---

[1] References cited in Appendices A-E are listed in the References at the end of the main text.

where Q is the volume flux and R is the Bernoulli constant. The velocity u_α can be expanded as a Fourier series:

$$u_\alpha = B_0 + \sum_{j=1}^{N} jkB_j \cos(jk\xi) \tag{A5}$$

where N is the number of Fourier components, B_j are the Fourier coefficients, and k is the wave number. To solve the problem numerically, the free surface elevation is discretized into N+1 equally spaced points over half a wavelength, i.e.,

$$\eta_m = \eta(\xi_m), m=0,1,\ldots,N \tag{A6}$$

where $\xi_m = mL/2N$ and L is the wavelength. Equations A3 to A4 are then evaluated at points over half a wavelength to yield a system of nonlinear algebraic equations:

$$(h+\eta_m)u_m + \left(\alpha + \frac{1}{3}\right)h^3 u_{\xi\xi,m} + Q = 0 \tag{A7}$$

$$g\eta_m + \frac{1}{2}u_m^2 + \alpha h^2 u_{\xi\xi,m} - R = 0 \tag{A8}$$

The above 2N+2 equations involve $2N + 5$ unknowns η_j ($j = 0, \ldots, N$), B_j ($j = 0, \ldots, N$), k, Q, R, so three additional equations are needed. These can be obtained from the wave height, H, wave period, T, the mean water level as:

$$\eta_0 - \eta_N - H = 0 \tag{A9}$$

$$kCT - 2\pi = 0 \tag{A10}$$

$$\eta_0 + \eta_N + 2\sum_{j=1}^{N-1}\eta_j = 0 \tag{A11}$$

noting that $C = -B_0$ for a zero-mean Eulerian velocity. A Newton-Raphson procedure (see Rienecker and Fenton 1981) is used to solve the system of equations (A7 to A11) for the unknown values of the free surface displacement at the collocation points, the Fourier coefficients, the wave number, the phase speed, and the constants Q and R.

Appendix B
Description of Ocean Wave Spectra

A number of parametric shapes have been proposed to describe the frequency distribution of wave energy. The spectral shapes were derived from long-term field wave measurements and depend on factors such as wind duration, the distance or fetch over which the wind blows, and water depth.

Pierson-Moskowitz Spectrum

For fully-developed sea states in deep water where there is a local balance between momentum transfer from the wind and wave breaking/nonlinear cross-spectral energy transfer processes, Pierson-Moskowitz (1964)[1] proposed the following wave spectrum:

$$S(f) = \frac{\alpha g^2}{(2\pi)^4 f^5} \exp\left[-\beta\left(\frac{f}{f_p}\right)^{-4}\right] \tag{B1}$$

where $\alpha = 0.0081$ is Phillips' constant, g is the gravitational acceleration, $\beta = 0.74$, $f_p = g/2\pi U_{19.5}$, and $U_{19.5}$ is the wind speed at 19.5 m above the mean sea level.

Bretschneider Spectrum

The Bretschneider spectrum (Bretschneider 1959) has the same shape as the Pierson-Moskowitz spectrum but is defined in terms of the significant wave height, H_s, and spectral peak frequency, f_p, instead of the wind speed. It can be written as:

---

[1] References cited in this appendix are listed in the References at the end of the main text.

$$S(f) = \frac{5H_s^2}{16} \frac{1}{(f/f_p)^5} \exp\left[-\frac{5}{4}\left(\frac{f}{f_p}\right)^{-4}\right] \tag{B2}$$

JONSWAP Spectrum

Based on an extensive analysis of data from the Joint North Sea Wave Observation Project (JONSWAP), Hasselmann et al. (1973) proposed the following modified form of the Pierson-Moskowitz spectrum to account for fetch-limited conditions:

$$S(f) = \frac{\alpha g^2}{(2\pi)^4 f^5} \exp\left[-\frac{5}{4}\left(\frac{f}{f_p}\right)^{-4}\right] \gamma^a \tag{B3}$$

where

$$\alpha = 0.076 \left(\frac{U_{10}^2}{gF}\right)^{0.22} \tag{B4}$$

$$f_p = 3.5 \left(\frac{U_{10}^2}{gF}\right)^{1/3} \tag{B5}$$

$$a = \exp\left[-(f - f_p)^2 / 2\sigma^2 f_p^2\right] \tag{B6}$$

$$\begin{cases} \sigma_a = 0.07 \quad \text{for} \quad f < f_p \\ \sigma_b = 0.09 \quad \text{for} \quad f < f_p \end{cases} \tag{B7}$$

F is the fetch distance, γ is a spectral peak enhancement factor, and U_{10} is the wind speed at 10 m above the mean sea level. Figure B1 shows a comparison of a JONSWAP spectrum with $\gamma = 3.3$ with a Bretschneider spectrum for a sea state. The JONSWAP spectrum reduces to the Bretschneider spectrum when γ is equal to 1.0.

TMA Spectrum

The TMA spectrum is a modified version of the JONSWAP spectrum for water of finite depth. It was proposed by Bouws, Gunther, and Vincent (1985) based on Kitaigorodskii, Krasitskii, and Zaslavskii (1975) frequency-dependent factor for the equilibrium range of the wave spectrum in shallow-water and validated with data from three field studies (Texel, MARSEN, and ARSLOE). It can be written as:
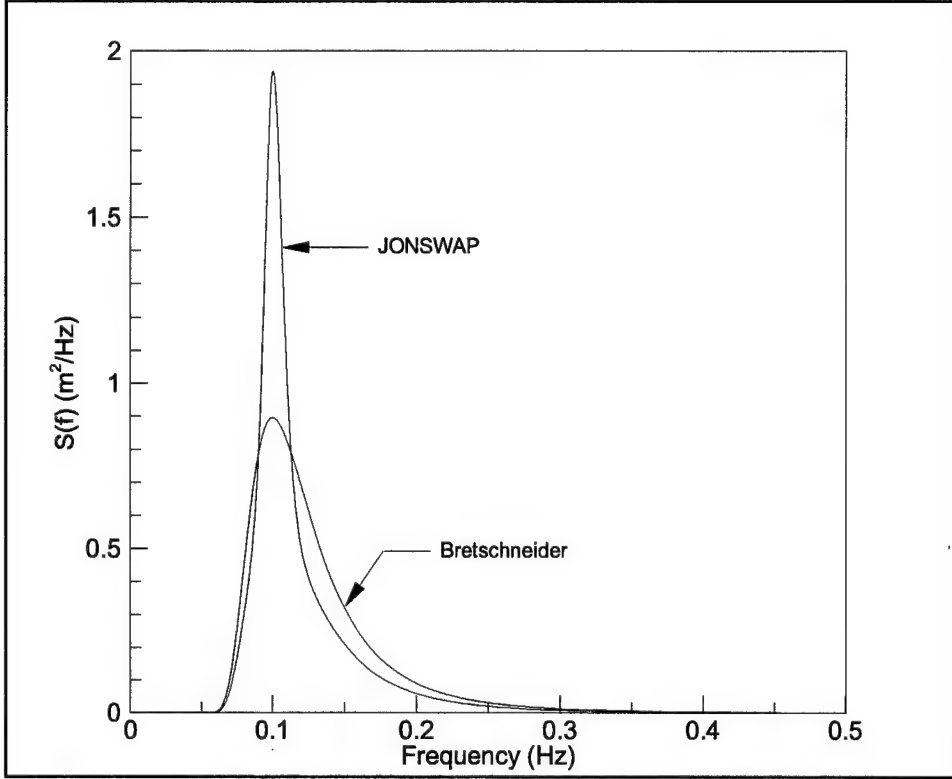
Figure B1. Comparison of Bretschneider and JONSWAP ($\gamma = 3.3$) spectra for a sea state with $H_{mo} = 1$ m, $T_p = 10$ s

$$S(f) = \frac{\alpha g^2}{(2\pi)^4 f^5} \, \exp\left[-\frac{5}{4}\left(\frac{f}{f_p}\right)^{-4}\right] \gamma^a \cdot \lambda(f,h) \tag{B8}$$

where $\lambda(f,h)$ is a function that expresses the effect of finite water depth and is given by:

$$\lambda(f,h) = \left[R(\omega_h)\right]^{-2} \left\{1 + \frac{2\omega_h^2 R(\omega_h)}{\sinh[2\omega_h^2 R(\omega_h)]\left[2\omega_h^2 R(\omega_h)\right]}\right\}^{-1} \tag{B9}$$

The frequency factor $\omega_h = 2\pi f \sqrt{(h/g)}$ and $R(\omega_h)$ is obtained from the iterative solution of the linear dispersion relation:

$$R(\omega_h)\tanh\left[\omega_h^2 R(\omega_h)\right] = 1 \tag{B10}$$

Ochi-Hubble Spectrum

The Ochi-Hubble spectrum (Ochi and Hubble 1976) is a six-parameter spectrum proposed for bimodal sea states consisting of swell and local wind-generated components. It can be written as:

$$S(f) = \frac{\pi}{2} \frac{\left[(4\gamma_1 + 1)(2\pi f_{p1})^4 / 4\right]^{\gamma_1}}{\Gamma(\gamma_1) \ (2\pi f)^{4\gamma_1 + 1}} H_{s1}^2 \exp\left[-\frac{4\gamma_1 + 1}{4}\left(\frac{f}{f_{p1}}\right)^{-4}\right]$$
$$+ \frac{\pi}{2} \frac{\left[(4\gamma_2 + 1)(2\pi f_{p2})^4 / 4\right]^{\gamma_2}}{\Gamma(\gamma_2) \ (2\pi f)^{4\gamma_2 + 1}} H_{s2}^2 \exp\left[-\frac{4\gamma_2 + 1}{4}\left(\frac{f}{f_{p2}}\right)^{-4}\right] \tag{B11}$$

where Γ is the gamma function. H_s, f_p, and γ denote the significant wave height, spectral peak frequency, and spectral shape factor respectively for the two sea state components. When γ is equal to 1, the Ochi-Hubble spectrum reduces to the Bretschneider spectrum.

Appendix C
Directional Wave Spreading Functions

The directional spreading function, $D(\theta)$, describes the directional distribution of wave energy in irregular multidirectional sea states. It can be quantified in terms of the principal direction of wave propagation θ_p, and the directional spread or standard deviation of the spreading function, σ_θ, which is defined as:

$$\sigma_\theta^2 = \int_{\theta_p - \pi/2}^{\theta_p + \pi/2} D(\theta) \, (\theta - \theta_p)^2 \, d\theta \tag{C1}$$

A number of parametric shapes have been proposed to describe the directional spreading function including the cosine-power, the circular normal, and wrapped-normal distributions. These are described in the following paragraphs.

Cosine-Power Spreading Function

The cosine-power function is an extended version of the cosine-squared directional distribution initially proposed by St. Denis and Pierson (1953)[1] and can be written as:

$$D(\theta) = \frac{\Gamma(s+1)}{\sqrt{\pi} \, \Gamma(s+1/2)} \cos^{2s}(\theta - \theta_p) \qquad \text{for } |\theta - \theta_p| < \pi/2 \tag{C2}$$

where Γ is the gamma function. The parameter s is an index describing the degree of directional spreading with $s \to \infty$ representing a unidirectional wave field.

Circular-Normal Spreading Function

The circular normal distribution was proposed by Borgman (1969) and can be written as:

---

[1] References cited in this appendix are listed in the References at the end of the main text.

$$D(\theta) = \frac{1}{2\pi I_0(a)} \exp\left[a\cos(\theta - \theta_p)\right] \tag{C3}$$

where I_0 is the modified Bessel function of the first kind and a is a parameter describing the degree of directional spreading with $a \to \infty$ representing a unidirectional wave field.

Wrapped-Normal Spreading Function

The wrapped-normal distribution was suggested by Mardia (1972) and is given by:

$$D(\theta) = \frac{1}{2\pi} + \frac{1}{\pi}\sum_{j=1}^{N}\exp\left[-\frac{1}{2}(j\sigma_\theta)^2\right]\cos\left[j(\theta - \theta_p)\right] \tag{C4}$$

Figure C1 shows a plot of the distributions for the three different spreading function formulations corresponding to a standard deviation σ_θ of 25.5 deg. The associated spreading indices are $s = 2$ for the cosine-power function and $a = 5.55$ for the circular-normal distribution. Thirty components ($N = 30$) were used for the wrapped-normal distribution. The cosine-normal and wrapped-normal distributions are slightly narrower than the cosine-power function although the differences can be considered to be minimal.
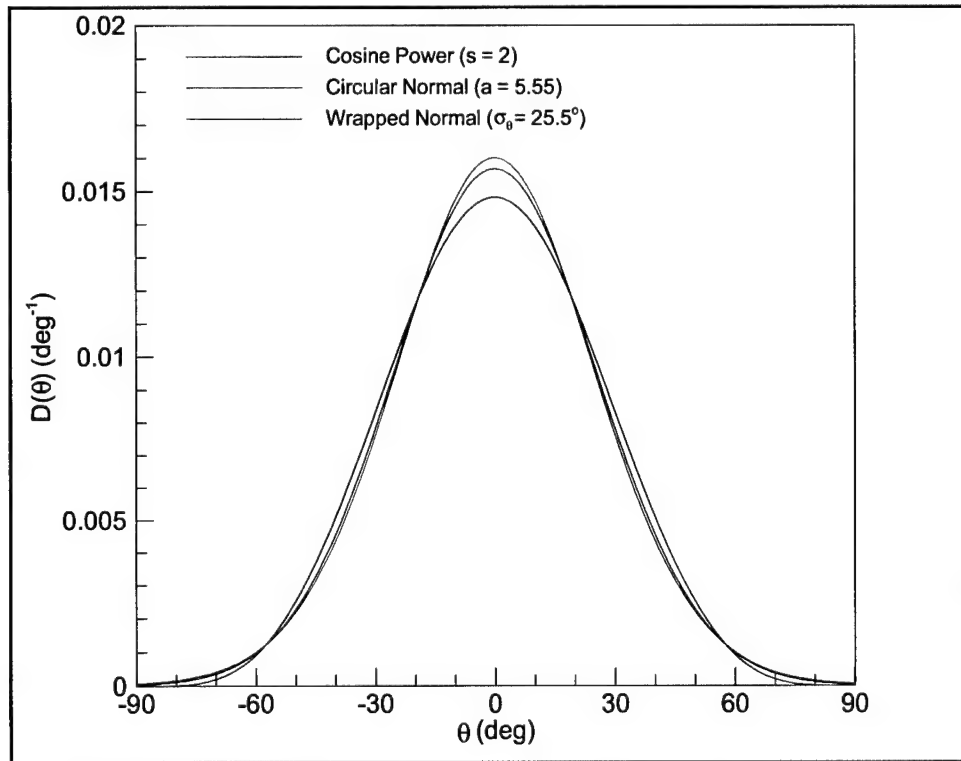

Figure C1. Comparison of the cosine-power, circular-normal and wrapped-normal distributions with a standard deviation of 25.5 deg

Appendix D
BOUSS-2D File Formats

BOUSS-2D currently supports two file formats. The grid format (.grd) is used to define the spatial variation of scalar or vector quantities over a rectangular grid. The time series format (.ts1) is used for one-dimensional time-histories of scalar quantities. The files consist of a header section and a data section. The header section includes both mandatory parameters required to define the data structure and optional parameters that provide additional information on the data. Comment lines in the header section begin with the pound (#) sign, and lines with parameter names and values begin with the colon (:) sign.

Grid File Format (.grd)

The grid file format is used to store multiple 2-D arrays $h_1(x,y)$, $h_2(x,y)$, etc. The variables are defined over a rectangular grid with the origin located at (x_{origin}, y_{origin}) and uniform grid spacings Δx and Δy in the x and y directions respectively. The number of grid points are N_x and N_y in the x and y directions respectively. The 2-D array $h(i,j)$ represents the value of $h(x,y)$ at $x = x_{origin} + (i-1)\Delta x$ and $y = y_{origin} + (j-1)\Delta y$. The mandatory header parameters are:

- NGrid_X = number of grid points in the x direction (N_x)
- NGrid_Y = number of grid points in the y direction (N_y)
- Delta_X = grid spacing in the x direction (Δx)
- Delta_Y = grid spacing in the y direction (Δy)
- X_Origin = x-coordinate of grid origin
- Y_Origin = y-coordinate of grid origin
- N_Arrays = number of data arrays (1 for scalar quantities, 2 for vector quantities)

The header section must terminate with the *EndHeader* keyword. Two-dimensional data are then written out after the header section as continuous data streams in row first order, i.e., $((h(i,j), i = 1, N_x), j = 1, N_y)$ for scalar quantities or $((u(i,j), i = 1, N_x), j = 1, N_y)$ and $((v(i,j), i = 1, N_x), j = 1, N_y)$ for vector quantities. A sample grid file is provided as follows:

```
# BOUSS2D Grid File
:FileName        bathy.grd
:WrittenBy       Bouss2D Version 1.0
:CreationDate    Mon Sep 18 12:40:25 2000
#
:N_Arrays        1
:DataDescription(1) Seabed Elevation
:DataUnits(1)      meters
#
:NGrid_X         4
:NGrid_Y         4
:Delta_X         10.0
:Delta_Y         10.0
:X_Origin        0.0
:Y_Origin        0.0
#
:EndHeader
15.8 15.8 15.8 15.8 15.8 15.8 15.8  15.8 15.8 15.8 15.8 15.8 15.8 15.8 15.8 15.8
```

Time Series File Format (.ts1)

The time series file format is used to store time-histories of scalar quantities $u(t)$ at discrete time intervals $t_i = t_1 + (i-1)\Delta t$, where t_1 is the start time and Δt is the time-step. The number of data points in the time record is N_t. Multiple time-histories (e.g., data output at different grid locations) can be stored in the same file. The mandatory header parameters are:

- NTimeSteps = number of time-steps (N_t)
- TimeStep = time-step (Δt)
- StartTime = start time of record (s)
- NDatasets = number of time series records

The header section terminates with the *EndHeader* keyword. Data are then written out after the header section as a single column vector for one time record or multiple columns for multiple time records. A sample time series file is provided as follows:

```
# BOUSS2D Time Series File
:FileName        test.ts1
:WrittenBy       Bouss2D Version 1.0
:CreationDate    Mon Sep 18 12:40:25 2000
#
:NDataSets              4
:DataDescription(1)     Surface Elevation
:DataUnits(1)           meters
:DataDescription(2)     Surface Elevation
:DataUnits(2)           meters
:DataDescription(3)     Surface Elevation
:DataUnits(3)           meters
:DataDescription(4)     Surface Elevation
:DataUnits(4)           meters
#
:StartTime              0.0000
:TimeStep               0.1500
:NTimeSteps             5334
#
```

```
:x_grid(1)          270.0000
:y_grid(1)          1030.0000
:x_grid(2)          500.0000
:y_grid(2)          1030.0000
:x_grid(3)          820.0000
:y_grid(3)          1030.0000
:x_grid(4)          1000.0000
:y_grid(4)          1030.0000
#
:EndHeader
    0.000000E+00   -1.772061E-15   -1.234493E-14   -4.485098E-14
   -1.195287E-13   -2.679531E-13   -5.388106E-13   -1.005685E-12
   -1.777521E-12   -3.012488E-12   -4.936255E-12   -7.866251E-12
   -1.224317E-11   -1.867146E-11   -2.797059E-11   -4.124122E-11
   -5.994772E-11   -8.602132E-11   -1.219879E-10   -1.711262E-10
   -2.376610E-10   -3.269985E-10   -4.460105E-10   -6.033756E-10
   -8.099900E-10   -1.079451E-09   -1.428627E-09   -1.878338E-09
   -2.454132E-09   -3.187200E-09   -4.115422E-09   -5.284574E-09
   -6.749691E-09   -8.576622E-09   -1.084376E-08   -1.364400E-08
         .               .               .               .
         .               .               .               .
         .               .               .               .
```

Appendix E
Utility Programs

GEN_DAMP

GEN_DAMP generates a damping file given the location of the damping layers (north, south, east, or west boundaries of the grid), the width of the damping layer, and the nondimensional damping strength at the end of the damping layer, μ_w. The damping values are initially set to zero over the entire grid. The program then calculates the spatial variation of the damping values over the width of the damping layers using a quadratic function, e.g.,

$$\mu_{nd}(x,y) = \left[\frac{x - x_0}{x_w - x_0} \right]^2 \mu_w$$

where x_0 and x_w are the coordinates of the beginning and end of the damping layer. The program is run interactively from an MS-DOS command prompt window. An example is as follows:

```
C:\bouss2d\bin\gen_damp
bathy   # name of input bathymetry file (.grd)
damp    # name of output damping file (.grd)
0       # width of damping layer - North (m) [0.0]
0       # non-dimensional damping strength (0-1) [0.0]
100     # width of damping layer - East (m) [0.0]
1       # non-dimensional damping strength (0-1) [0.0]
0       # width of damping layer - South (m) [0.0]
0       # non-dimensional damping strength (0-1) [0.0]
0       # width of damping layer - West (m) [0.0]
0       # non-dimensional damping strength (0-1) [0.0]
```

To effectively damp out waves at open boundaries, a damping layer half a wave-length wide with a damping strength of 1.0 should be used. The damping file is written out as an ASCII file in the grid file format described in Appendix D.

MAP_POROSITY

MAP_POROSITY creates a porosity grid file given the boundaries of porous regions within the computational domain as a set of discrete (x,y) points. The

porosity values are initially set to 1.0 over the entire grid. The program then uses the "Winding-Number" algorithm of Gordkin and Pulli (1984)[1] to set the porosity values within the porous region boundaries to values specified by the user. The (x,y) coordinates of the porous region boundaries are stored as two columns of data in an ASCII file. The program is run interactively from an MS-DOS command prompt window. An example is as follows:

```
C:\bouss2d\bin\map_porosity
bathy          # name of input bathymetry file (.grd)
porosity       # name of output porosity file (.grd)
2              # number of porous regions [1]
bw1.xy         # name of boundary file for porous region #1 [.xy]
0.4            # porosity (0-1) [0.4]
bw2.xy         # name of boundary file for porous region #2 [.xy]
0.4            # porosity (0-1) [0.4]
```

The porosity file is written out as an ASCII file in the grid file format described in Appendix D.

---

[1] References cited in this appendix are listed in the References at the end of the main text.

REPORT DOCUMENTATION PAGE

1. REPORT DATE (DD-MM-YYYY) September 2001	2. REPORT TYPE Report 1 of a series	3. DATES COVERED (From - To)

4. TITLE AND SUBTITLE

BOUSS-2D: A Boussinesq Wave Model for Coastal Regions and Harbors; Theoretical Background and User's Manual

5a. CONTRACT NUMBER

5b. GRANT NUMBER

5c. PROGRAM ELEMENT NUMBER

6. AUTHOR(S)

Okey George Nwogu, Zeki Demirbilek

5d. PROJECT NUMBER

5e. TASK NUMBER

5f. WORK UNIT NUMBER

7. PERFORMING ORGANIZATION NAME(S) AND ADDRESS(ES)

U.S. Army Engineer Research and Development Center
Coastal and Hydraulics Laboratory
3909 Halls Ferry Road
Vicksburg, MS 39180-6199

8. PERFORMING ORGANIZATION REPORT NUMBER

ERDC/CHL TR-01-25

9. SPONSORING / MONITORING AGENCY NAME(S) AND ADDRESS(ES)

U.S. Army Corps of Engineers
Washington, DC 20314-1000

10. SPONSOR/MONITOR'S ACRONYM(S)

11. SPONSOR/MONITOR'S REPORT NUMBER(S)

12. DISTRIBUTION / AVAILABILITY STATEMENT

Available for public release; distribution in unlimited.

13. SUPPLEMENTARY NOTES

14. ABSTRACT

BOUSS-2D is a comprehensive numerical model for simulating the propagation and transformation of ocean waves in coastal regions and harbors. The model is based on depth-integrated Boussinesq-type mass and momentum equations for nonlinear-dispersive waves. The equations describe most of the wave transformation phenomena of interest in coastal regions and harbors including shoaling, refraction, diffraction, reflection, nonlinear wave-wave interactions, and wave breaking. This manual describes the theoretical background behind the model and the steps involved in setting up and running the model.

15. SUBJECT TERMS

Boussinesq equation	Harbor entrances	Wave breaking	Wave-wave interactions
Diffraction	Numerical wave modeling	Wave transformation	
	Refraction	Wave-current interactions	

16. SECURITY CLASSIFICATION OF:

a. REPORT	b. ABSTRACT	c. THIS PAGE	17. LIMITATION OF ABSTRACT	18. NUMBER OF PAGES	19a. NAME OF RESPONSIBLE PERSON
UNCLASSIFIED	UNCLASSIFIED	UNCLASSIFIED		90	19b. TELEPHONE NUMBER (include area code)